EXPERIMENTAL AND NUMERICAL INVESTIGATION OF RADIAL-RADIAL SWIRLERS UNDER DIFFERENT CONFINEMENT CONDITIONS

A THESIS SUBMITTED TO
THE GRADUATE SCHOOL OF NATURAL AND APPLIED SCIENCES
OF
MIDDLE EAST TECHNICAL UNIVERSITY

BY

FIRAT KIYICI

IN PARTIAL FULFILLMENT OF THE REQUIREMENTS
FOR
THE DEGREE OF MASTER OF SCIENCE
IN
AEROSPACE ENGINEERING

JULY 2022

Approval of the thesis:

EXPERIMENTAL AND NUMERICAL INVESTIGATION OF RADIAL-RADIAL SWIRLERS UNDER DIFFERENT CONFINEMENT CONDITIONS

submitted by **FIRAT KIYICI** in partial fulfillment of the requirements for the degree of **Master of Science in Aerospace Engineering Department, Middle East Technical University** by,

Prof. Dr. Halil Kalıpçılar
Dean, Graduate School of **Natural and Applied Sciences** _____

Prof. Dr. Serkan Özgen
Head of Department, **Aerospace Engineering** _____

Assist. Prof. Dr. Mustafa Perçin
Supervisor, **Aerospace Engineering, METU** _____

Examining Committee Members:

Prof. Dr. Yusuf Özyörük
Aerospace Engineering, METU _____

Assist. Prof. Dr. Mustafa Perçin
Aerospace Engineering, METU _____

Assist. Prof. Dr. Sıtkı Uslu
Mechanical Engineering, TOBB ETU _____

Assist. Prof. Dr. Halil Ersin Söken
Aerospace Engineering, METU _____

Assist. Prof. Dr. Onur Baş
Mechanical Engineering, TED University _____

Date: 27.07.2022

I hereby declare that all information in this document has been obtained and presented in accordance with academic rules and ethical conduct. I also declare that, as required by these rules and conduct, I have fully cited and referenced all material and results that are not original to this work.

Name, Surname: Fırat Kıyıcı

Signature :

ABSTRACT

EXPERIMENTAL AND NUMERICAL INVESTIGATION OF RADIAL-RADIAL SWIRLERS UNDER DIFFERENT CONFINEMENT CONDITIONS

Kıyıcı, Fırat
M.S., Department of Aerospace Engineering
Supervisor: Assist. Prof. Dr. Mustafa Perçin

July 2022, 115 pages

In modern gas turbine combustors, flame stabilization is achieved by use of swirlers which introduce swirl component to the flow field. Swirlers are inherently sensitive to flow and environmental conditions, and even a minor geometrical modification can change the flow field remarkably. One of the critical parameters that affect the performance of the swirler is the channel orientation of the swirler channels. In the literature, the channel orientation has been mostly investigated at constant confinement ratio levels, and results showed that the performance of the co-rotating (CO) and counter-rotating (CR) swirlers are different in a number of aspects. In this study, the sense of the swirler channel rotation is investigated under different confinement ratio levels at a fixed total swirl number of 1.2 by using a 2D2C PIV system in isothermal conditions. The experimental results show that the confinement affects the CO and CR swirlers oppositely. As the confinement ratio increases, the radial expansion of the swirling jet decreases in the CR swirler while it increases in the CO swirler for the confined cases. For all levels of confinement, a higher degree of radial expansion is observed in the CO swirler. In addition, steady-state RANS simulations are performed to support the experimental findings, which are in good agreement with ex-

perimental data except for the unconfined condition. On the other hand, Large Eddy Simulations (LES) provide results that are in a better agreement with the experimental data in the unconfined configuration. Furthermore, a spectral proper orthogonal (S-POD) analysis is conducted to understand the effect of the confinement ratio on the dynamics of coherent flow structures. The S-POD results exhibit a single helical structure with a frequency of 1.2 kHz observed for both CO and CR swirlers under all confinement ratio levels. The S-POD mode shapes reveal that the confinement can suppress low-frequency global instability modes or higher frequency mode structures. Finally, changing the number of channels does not change the frequency of the PVC when the swirl number is kept identical.

Keywords: Swirler, Coherent Structures, Computational Fluid Dynamics, Particle Image Velocimetry, Confinement Ratio

ÖZ

RADYAL-RADYAL TİPİNDEKİ DÖNDÜRÜCÜLERİN FARKLI HAPSETME ORANLARI ALTINDA DENEYSEL VE NÜMERİK İNCELENMESİ

Kıyıcı, Fırat
Yüksek Lisans, Havacılık ve Uzay Mühendisliği Bölümü
Tez Yöneticisi: Dr. Öğr. Üyesi. Mustafa Perçin

Temmuz 2022 , 115 sayfa

Modern gaz türbin motorlarında, alev kararlılığı sıklıkla akış alanına döndürücü vasıtasıyla dönen bir hava momentumu verilerek sağlanmaktadır. Döndürücüler doğası gereği akış ve çevresel koşullara duyarlıdır ve geometride yapılacak en ufak bir değişiklik akış alanında ciddi değişiklikler meydana getirmektedir. Döndürücü kanallarının dönüş yönü dönürücü performansını etkileyen parametrelerin başında gelmektedir. Literatürde döndürücü kanallarının dönüş yönü genellikle sabit hapsetme oranlarında incelenmiştir ve sonuçlar eş- ve ters- dönüşlü döndürücülerin performanslarının birçok açıdan farklı olduğu görülmüştür. Bu çalışmada, döndürücü kanallarının dönüş yönü farklı hapsetme oranlarında ve 1.2 sabit toplam dönüş sayısında 2 boyutlu-2 hız komponentli Parçacık Görüntülemeli Hız Ölçme Tekniği ile izotermal koşulda incelenmiştir. Deneysel sonuçlara göre eş- ve ters- dönüşlü döndürücülerin performansı hapsetme oranından ters şekilde etkilenmektedir. Hapsetme oranı arttıkça dönen jetin radyal açılması ters- dönüşlü döndürücüde azalırken eş-dönüşlü döndürücüde ise artmıştır. Bütün hapsetme oranı seviyelerinde eş-dçnüşlü döndürücüde daha fazla radyal

açılma gözlemlenmiştir. Buna ek olarak, Reynolds-Ortalamalı Navier Stokes analizleri de deneysel sonuçları desteklemek için gerçekleştirilmiştir ve hapsetme duvarı olan durumdaki deneylerle tutarlı sonuçlar elde edilmiştir. Hapsetme duvarı olmayan koşullarda ise Büyük Burgaç Simülasyonu gerçekleştirilmiştir ve deneyle uyumlu sonuçlar elde edilmiştir. Ayrıca, Spektral-POD analizleri gerçekleştirilerek hapsetme oranının koherent akış yapılarının dinamik karakteristiği üzerindeki etkisi incelenmiştir. Spektral-POD sonuçları 1.2 kHz'deki tekli bir helisel yapının eş- ve ters-dönüşlü döndürücü için bütün hapsetme oranlarında görüldüğünü ortaya çıkartmıştır. Ayrıca, Spektral-POD mod şekilleri hapsetme oranının düşük frekanstaki evrensel kararsızlık modlarını ya da yüksek frekanstaki mod yapılarını bastırabildiğini göstermiştir. Son olarak, dönüş sayısı aynı tutulacak şekilde kanal sayısını değiştirmenin devinen girdap çekirdeği frekansına bir etkisi olmadığı gözlemlenmiştir.

Anahtar Kelimeler: Döndürücü, Koherent Yapılar, Hesaplamalı Akışkanlar Dinamiği, Parçacık Görüntülemeli Hız Ölçme Tekniği, Hapsetme Oranı

Dedicated to loving memory of my grandfather

ACKNOWLEDGMENTS

Words cannot express my gratitude to my advisor Mustafa Percin for his endless support and feedback during this journey. Without his knowledge and experience, I could not be able to complete this thesis as I wanted.

I'm also extremely grateful to jury members Prof. Dr. Oğuz Uzol, Prof. Dr. Yusuf Özyörük, Assist. Prof. Dr. Sıtkı Uslu, Assist. Prof. Dr. Onur Bas and Assist. Prof. Dr. Ersin Söken for their valuable comments and discussions. Especially, I am deeply indebted to Assist. Prof. Dr. Sıtkı Uslu who has supported me since my undergraduate years to work in the field of propulsion.

I am also grateful to my colleagues Battal Gencer and Ayse Bay for their support. Performing experiments would not be more straightforward without them. Also, I am so thankful to RUZGEM and RUZGEM personnel for their help whenever needed.

I would like to thank my "big brothers" Hasret Türkeri and Ender Hepkaya for their support in performing scale-resolving simulations. Especially, I am so indebted to Ahmet Topal for initiating fundamental research studies at universities. Also, I am so grateful to my colleagues Ahmet Kaan Zayim and Kubilay Arar for the mechanical design of the test article.

I wish to extend my special thanks to my past managers Emin Nadir Kaçar, İlkay Solak, Ercan Arıcan, Ali Tuna Kırgız, and TUSAS Engine Industries Inc for financially supporting this study.

Lastly, I would be remiss in not mentioning my family. Their belief in me has kept my spirits and motivation high during this process. I would also like to thank my wife Cansu for all the entertainment and emotional support. Without her, I could not complete this study.

TABLE OF CONTENTS

ABSTRACT v

ÖZ vii

ACKNOWLEDGMENTS x

TABLE OF CONTENTS xi

LIST OF TABLES xiv

LIST OF FIGURES xvi

LIST OF ABBREVIATIONS xxiii

CHAPTERS

1 INTRODUCTION 1

1.1 Effect of the channel orientation 10

1.2 Effect of the confinement ratio 12

1.3 The coherent structures 13

1.4 Motivation and objectives 17

1.5 Structure of the thesis 18

2 METHODOLOGY 19

2.1 Experimental Setup 19

2.1.1 Experimental Facility 19

2.1.2 Radial-Radial Swirlers 22

2.2 Particle Image Velocimetry 26
2.3 Uncertainty Analysis 31
2.4 Numerical Method 36
2.4.1 Mathematical Formulation 36
2.4.2 Solution Algorithms 37
2.4.3 Turbulence Modeling 39
2.4.3.1 Reynolds-Averaged Navier Stokes Simulations 44
2.4.3.2 Large Eddy Simulations 47
2.4.3.3 Numerical Validation 50
2.4.4 Numerical Setups 58
2.5 Modal Analysis 63
2.5.1 Proper Orthogonal Decomposition 63
2.5.2 Spectral Proper Orthogonal Decomposition 64
3 RESULTS AND DISCUSSIONS 65
3.1 Effect of the channel orientation 65
3.1.1 Time-averaged flow fields 65
3.1.2 Coherent flow structures 74
3.2 Effect of the confinement ratio 77
3.2.1 Time-averaged flow fields 78
3.2.2 Coherent flow structures 96
3.3 Effect of channel number 100
4 CONCLUSION 103
5 FUTURE WORKS 105

REFERENCES 107

LIST OF TABLES

TABLES

Table 1.1 Swirler-Injector Configurations [9] 5

Table 2.1 Control unit configurations 20

Table 2.2 Slow PIV recording parameters for the mid- and cross-plane measurements 32

Table 2.3 Domain size, vector resolution and data acquisition frequency for the fast PIV measurements 33

Table 2.4 The statistical uncertainty estimates for the Reynolds stresses (mean values calculated in the measurement plane up to $y/D_h = 2$ and mean non-dimensional values normalized by the jet velocity and Reynolds stresses in brackets) 34

Table 2.5 The statistical uncertainty estimates for the mean flow (mean values calculated in the measurement plane up to $y/D_h = 2$ with mean of the normalized values in brackets) 34

Table 2.6 Experimental coefficients of the Standard k-ϵ model 45

Table 2.7 Experimental coefficients of the Realizable k-ϵ model 46

Table 2.8 Comparison of flow parameters for different meshes considered in the mesh independence study 59

Table 3.1 Swirl numbers at different streamwise positions calculated based on the results of the numerical simulations 70

Table 3.2 Normalized reversed mass flow rates (normalization is performed using the medium confinement cases of the CR swirler) and width of the CTRZ 81

Table 3.3 Absolute SN at $y/D_h = 0.5$, 1, 2 and 3 for the CR and CO swirlers under different confinement conditions 89

Table 3.4 CTRZ length results for different turbulence models 95

Table 3.5 Frequency and amplitude of the PVC for the CR and CO swirlers under different confinement conditions 97

Table 3.6 Energy contribution of the PVC in the total energy of the flow 99

Table 3.7 Frequency and amplitude of the PVC for different channel numbers and orientations 102

LIST OF FIGURES

FIGURES

Figure 1.1 Schematic of a simple gas turbine architecture [1] 1

Figure 1.2 Schematic of a gas turbine combustor[3] 2

Figure 1.3 Schematic of swirling flow field [9] 4

Figure 1.4 Axial and radial swirlers 5

Figure 1.5 Bubble (upper) and double-helix (lower) type vortex breakdown [10] 6

Figure 1.6 Regular (left) and wide-open (right) type conical vortex breakdown [11] 6

Figure 1.7 Schematic of the PVC motion [4] 7

Figure 1.8 Combustion instability loop [12] 8

Figure 1.9 Schematic of a radial-radial type swirler 8

Figure 1.10 Radial-radial type swirler parts [17] 9

Figure 1.11 Symmetric and anti-symmetric mode shape structures [44] . . . 16

Figure 2.1 Schematic of the experimental facility 21

Figure 2.2 1st pressure regulator 22

Figure 2.3 Control unit of the experimental facility 22

Figure 2.4 Mixing chamber 23

Figure 2.5 Settling chamber and turbulent screen 24

Figure 2.6 Measured normalized inlet velocity profile 24

Figure 2.7 Low, medium and high confinement ratio test sections 25

Figure 2.8 Schematic of the radial-radial swirler 26

Figure 2.9 Working principle of the PIV system [48] 27

Figure 2.10 Schematic of the slow and fast PIV measurement planes for different confinement ratio conditions 28

Figure 2.11 Experimental setup for the cross-stream PIV measurements at $y/D_{\mathrm{h}} = 1$ and 3: a sketch showing the adapted coordinate system (left); a schematic of the setup showing the the positions of the measurement planes(right) 29

Figure 2.12 A photo of the experimental setup during data acquisition 30

Figure 2.13 Comparison of the time-averaged radial velocity (the velocity component in the x direction, U/V_0) profiles obtained from the mid-plane streamwise PIV measurements and cross-stream PIV measurements at y/D_{h}= 1 & 3 35

Figure 2.14 PIMPLE algorithm 38

Figure 2.15 Coupled algorithm 38

Figure 2.16 Energy cascade from large eddies to small eddies [57] 40

Figure 2.17 Turbulent energy spectrum 41

Figure 2.18 Resolved and modeled scales of the turbulence for RANS, LES and DNS [58] 42

Figure 2.19 Schematic of the instantaneous, time-averaged and fluctuating velocity components [60] 43

Figure 2.20 Schematic of the Cambridge/Sandia stratified swirl burner [77], [78] 51

Figure 2.21 Computational domain for the Cambridge/Sandia validation case 51

Figure 2.22 The evaluation of the LESIQ for the Cambridge/Sandia validation case 52

Figure 2.23 Axial velocity contours of RANS (upper) vs LES (lower) in isothermal condition 54

Figure 2.24 Time-averaged velocity profile comparison at different locations in isothermal condition 56

Figure 2.25 The r.m.s. velocity profile comparison at different locations in isothermal condition 57

Figure 2.26 Comparison of the time-averaged axial velocity (the velocity component in the y-direction, V/V_0), obtained from numerical simulations for the coarse, medium and fine mesh configurations in the $y/D_h = 0.5$, 1 and 2 59

Figure 2.27 Computational domain with boundary conditions (top) and the computational mesh with a close-up view (bottom) for RANS 61

Figure 2.28 Computational domain (top) and the computational mesh with a close-up view (bottom) for LES 62

Figure 2.29 LESIQ evaluation for the unconfined configuration of the CR swirler 62

Figure 3.1 Contours of the time-averaged axial velocity component (the velocity component in the y direction, V/V_0) complemented with the flow streamlines for the CR (left) and CO (right) swirler configurations obtained from the PIV measurements 67

Figure 3.2 Contours of the time-averaged axial velocity component (the velocity component in the y direction, V/V_0) complemented with the flow streamlines for the CR (left) and CO (right) swirler configurations obtained from the numerical simulations 67

Figure 3.3 Contours of the normalized turbulent kinetic energy (TKE/V_0^2) distributions for the CR (left) and the CO (right) swirler configurations . 68

Figure 3.4 Contours of the normalized time averaged out-of-plane vorticity (i.e., z-vorticity, $\omega_z D_h/V_0$) for the CR (left) and the CO (right) swirler configurations 68

Figure 3.5 Time-averaged axial velocity (the velocity component in the y direction, V/V_0), radial velocity (the velocity component in the x direction, U/V_0) and turbulent kinetic energy (TKE) profiles at y/D_{h}= 0.25 69

Figure 3.6 Contours of the time-averaged tangential velocity component (V_t/V_0) complemented with streamlines in the cross-stream planes at the axial positions of y/D_{h}= 1 (top row) and 3 (bottom row) for the CR (left) and the CO (right) swirlers 71

Figure 3.7 Time averaged tangential velocity profiles obtained from the results of the PIV measurements in the cross-stream planes at y/D_{h}= 1 (dashed line) y/D_{h} =3 (full line) for the CR (left) and the CO (right) swirlers 71

Figure 3.8 Contours of turbulent kinetic energy (TKE/V_0^2) obtained from the PIV measurements in the cross-stream plane at y/D_{h}= 1 72

Figure 3.9 Time-averaged axial velocity (the velocity component in the y direction) profiles obtained from the streamwise PIV measurements at the center of the CTRZ for the CR (red circles) and CO (blue asterisks) swirlers. The vertical dashed lines represent the radial location where the axial velocity turns from negative to positive values. 73

Figure 3.10 Comparison of the time-averaged axial velocity (the velocity component in the y-direction, V/V_0), radial velocity (the velocity component in the x-direction, U/V_0) and the tangential velocity (the velocity component in the z-direction, $|W|/V_0$) profiles obtained from the PIV measurements (symbols) and numerical simulations (full lines) for the CO (blue) and the CR (red) configurations in the streamwise plane aligned with the center of the swirler 74

Figure 3.11 The first three most energetic modes and the power spectral densities of their time coefficients obtained from the snapshot POD analysis for the CR (left) and CO (right) swirlers 75

Figure 3.12 Results of the spectral-POD analysis (mode shapes and power spectral densities) for the CR (left) and CO (right) swirlers 77

Figure 3.13 Contours of the time-averaged axial velocity component (the velocity component in the y direction, V/V_0) complemented with the flow streamlines for the CR (left) and CO (right) swirler configurations obtained from the PIV measurements under different confinement ratio conditions 79

Figure 3.14 Time-averaged profiles of the velocity component in the y direction (V/V_0 corresponding to axial velocity component) along the center of the recirculation zones for the confined cases 81

Figure 3.15 Contours of the normalized turbulent kinetic energy (TKE/V_0^2) distributions for the CR (left) and the CO (right) swirler configurations under different confinement ratio conditions 83

Figure 3.16 Contours of the time-averaged axial velocity component (the velocity component in the y direction, V/V_0) complemented with the flow streamlines for the CR (left) and CO (right) swirler configurations obtained from the numerical simulations under different confinement ratio conditions 84

Figure 3.17 Comparison of the time-averaged axial velocity (the velocity component in the y-direction, V/V_0), radial velocity (the velocity component in the x-direction, U/V_0) profiles obtained from the PIV measurements (symbols) and numerical simulations (full lines) for the CO (blue) and the CR (red) configurations in the $y/D_h = 0.5$, 1 and 2 . . . 86

Figure 3.18 Contours of the time-averaged normalized vorticity distribution ($\omega D_h/V_0$) for the CR (left) and CO (right) swirler configurations obtained from the numerical simulations under different confinement ratio conditions 88

Figure 3.19 Time-averaged velocity contour of RANS for unconfined condition (white lines represent the recirculation zone borders) 91

Figure 3.20 Time-averaged velocity contour of LES for unconfined condition (white lines represent the recirculation zone borders) 92

Figure 3.21 Comparison of the time-averaged axial velocity (the velocity component in the y-direction, V/V_0), radial velocity (the velocity component in the x-direction, U/V_0) profiles obtained from the PIV measurements (symbols) and numerical simulations (full lines) for the RANS (red) and the LES (blue) configurations in the y/D_h= 0.5, 1 and 2 . . . 93

Figure 3.22 Comparison of the r.m.s axial velocity (the velocity component in the y-direction, v'/V_0), radial velocity (the velocity component in the x-direction, u'/V_0) profiles obtained from the PIV measurements (symbols) and numerical simulations (full lines) for the LES (blue) in the y/D_h= 0.5, 1 and 2 94

Figure 3.23 The first three most energetic modes obtained from the S-POD analysis for the CR swirler under different confinement conditions . . . 98

Figure 3.24 The snapshot-POD and S-POD mode shape of the global hydrodynamic instability 99

Figure 3.25 The first three most energetic modes obtained from the S-POD analysis for the CO swirler under different confinement condition 100

Figure 3.26 Effect of the channel number on the time-averaged axial velocity profiles [86] 101

Figure 3.27 PVC modes shapes for different channel numbers and orientations 102

Figure 5.1 Isometric (top) and cross-section (bottom) view of the CANTEC-SD 106

LIST OF ABBREVIATIONS

CR	Counter-Rotating
CO	Co-Rotating
SN	Swirl Number
D_h	Hydraulic Diameter
V_0	Swirler Inlet Velocity
V_{jet}	Swirler Exit Bulk Velocity
RANS	Reynolds-Averaged Navier Stokes
LES	Large Eddy Simulation
PIV	Particle Image Velocimetry
2D2C	Two-Dimensional, Two Component
PVC	Precessing Vortex Core
CTRZ	Central Toroidal Recirculation Zone
CRZ	Corner Recirculation Zone
TKE	Turbulent Kinetic Energy
POD	Proper Orthogonal Decomposition
S-POD	Spectral Proper Orthogonal Decomposition
LESIQ	Large Eddy Simulation Index Quality
Rpo	Primary Swirler Outer Radius
Rso	Secondary Swirler Outer Radius
Rsi	Secondary Swirler Inner Radius

CHAPTER 1

INTRODUCTION

One of the revolutionary inventions of humanity is gas turbines. They have been used in various ways, including power generation and civil and military flights. The working principle of the gas turbine engines depends on the Brayton cycle, and a simple gas turbine cycle includes compressors, combustion chambers, and turbines, as shown in Fig. 1.1. For power generation, a pressurized fluid is necessary to rotate the turbine blades, and pressurized air is obtained through compression by compressors. However, suppose the compressor directly connects with the turbine under the assumption of an isentropic process. In that case, the turbine's extracted power will equal the required power by compressors and eventually stop the whole system. If any energy is added to the system after the compressor, the extracted power by the turbine increases, and the system maintains itself until the energy source is removed.

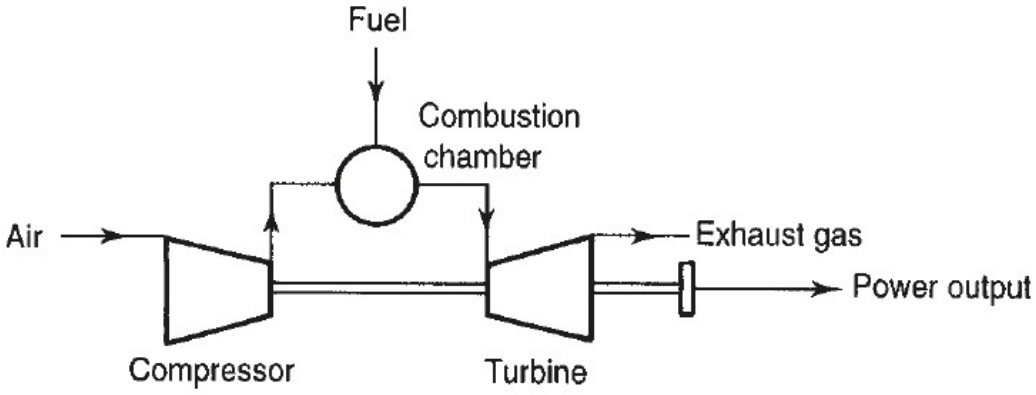


Figure 1.1: Schematic of a simple gas turbine architecture [1]

The required energy is added to the system due to the combustion process inside the combustors. The combustion is a chemical reaction chain between the fuel and

oxidizer which offers a high amount of energy to any system. Thus, high-temperature pressurized air is introduced to the turbine, and the turbine releases the energy by expanding the volume of the gaseous through the turbine stages. The released energy is converted to shaft work to drive the compressor and other systems.

Designing a combustor or combustion chamber is a highly compelling process due to the interaction of several phenomena such as fluid mechanics (turbulence, swirling flow, spray, and atomization), heat transfer, chemistry, and mechanical design. A schematic of the combustor is shown in Fig. 1.2. First, the diffuser reduces the velocity of the incoming air. Then the flow is divided into snout, inner and outer annulus sections. Inside the snout, a swirler and injector are located. The role of the injector is to introduce the fuel particles with smaller diameters for easier ignition and continuous combustion. Swirlers are used to generate a recirculation zone to anchor the flame and prevent the blow-off. Primary jets confines the recirculation zone to create stagnation points. Also, primary jets are used to create a perfectly stirred reaction zone in the primary zone [2]. The secondary jets introduce the fresh air to complete the combustion, and dilution jets provide desirable exit profiles for long-life turbines.

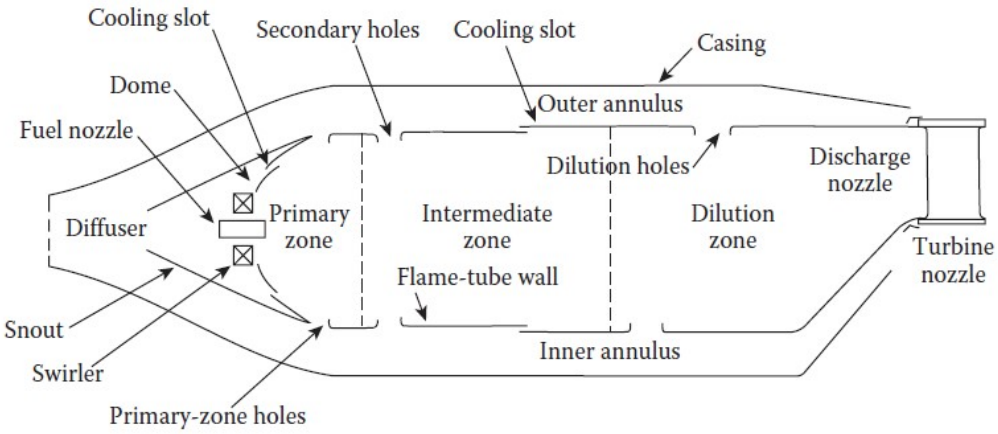


Figure 1.2: Schematic of a gas turbine combustor[3]

The major problem of the combustion systems is the flame being prone to blow-off, meaning the physical departure of the flame from the combustor [4]. The propagation

speed of the flame is lower than the flow speed, and flames can not sustain themselves under this condition. For example, for fixed fuel/air ratio levels, the flame will blow-off when the flow's velocity magnitude increases. Similarly, if the fuel-air ratio decreases at a constant velocity magnitude, the flame will be blow-off again. The blow-off can be described in terms of combustor loading which is a function of chemical kinetic time scale (τ_{che}) and fuel-particles residence time (τ_{res}). The chemical time scale defines the required time for complete combustion of a fuel particle, while the residence time refers to the lifetime of a fuel particle in the reaction zone. If the fuel particle residence time is far lower than the chemical time-scale, the flame will blow off [4]. To prevent the blow-off, we need faster combustion or a longer residence time of fuel particles. This is called flame-anchoring or flame stabilization, which is part of the static stability of the combustors.

$$Loading = \tau_{\text{che}}/\tau_{\text{res}} \tag{1.1}$$

There are several ways to anchor the flames, such as using a bluff-body, introducing swirling flow, or using piloted flames. The most common way of stabilizing the flame in modern gas turbine combustors is to introduce a swirling flow. Swirlers are used in gas turbine combustion chambers for flame stabilization by introducing the swirl velocity component to the flame tube of combustors. When the introduced swirl momentum is sufficiently high, a reversed flow region starts to develop, forming a central toroidal recirculation zone (CTRZ) [5] as a result of the vortex-breakdown. The CTRZ is a crucial element for flame stabilization and more efficient combustion. A schematic of the CTRZ is shown in Fig 1.3. In this flow reversal zone, fresh air mixes well with fuel while unburned fuel particles return to the reaction zone, which increases the number of burned fuel particles compared to combustors operating without a CTRZ. The swirling flow expands radially when it is introduced to the flow field. Thus, a corner recirculation zone (CRZ) may also be formed between the combustor walls and CTRZ. A strong shear layer occurs between the CRZ and the CTRZ, which increases the level of turbulent mixing and reduces the diameter of the fuel spray particles.

The strength of the swirling momentum is generally quantified by the swirl number

(SN), which is the ratio of the axial flux of the tangential momentum to the axial flux of the axial momentum. High swirl flows are generally defined to have an SN of 0.6 or more due to the formation of a CTRZ at these swirl numbers [6]. However, these characteristic flow patterns such as vortex breakdown and CTRZ may also occur at lower swirl number values [7], [8]. Even though the swirling flow stabilizes the flame, increasing the degree of the swirling momentum would not be the best option, leading to severe combustion instability and damaging the hardware of the combustors. This is associated with the dynamic stability of the combustors [4].

Swirlers are named as how they introduce the swirling flow to the combustors, and the two most commonly used swirler types are radial and axial swirlers. The radial swirlers introduce air radially inside the swirlers, and the radial momentum is converted into tangential momentum. Whereas the axial swirler uses swirl blades (similar to those used in turbomachinery applications) to obtain a swirling flow. The swirler types are shown in Fig. 1.4. Different types of swirler configurations are used in gas turbine engines as listed in Table 1.1 [9].

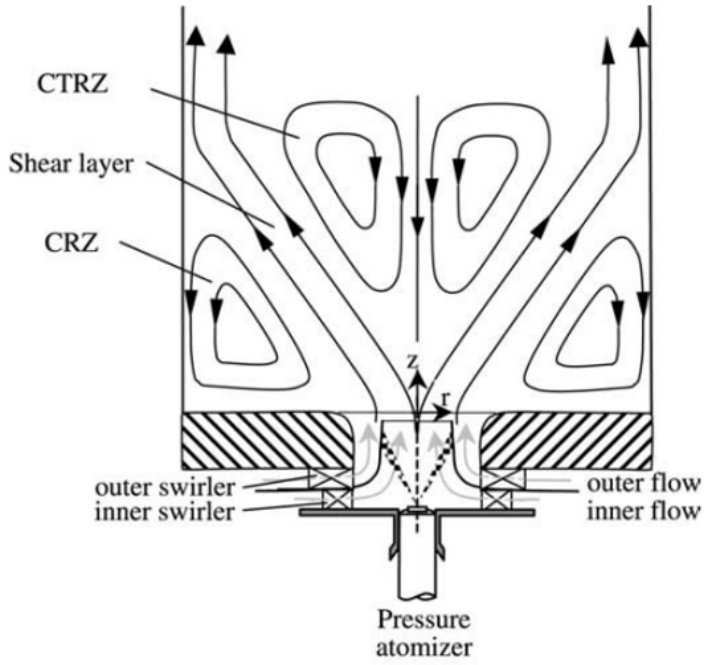


Figure 1.3: Schematic of swirling flow field [9]

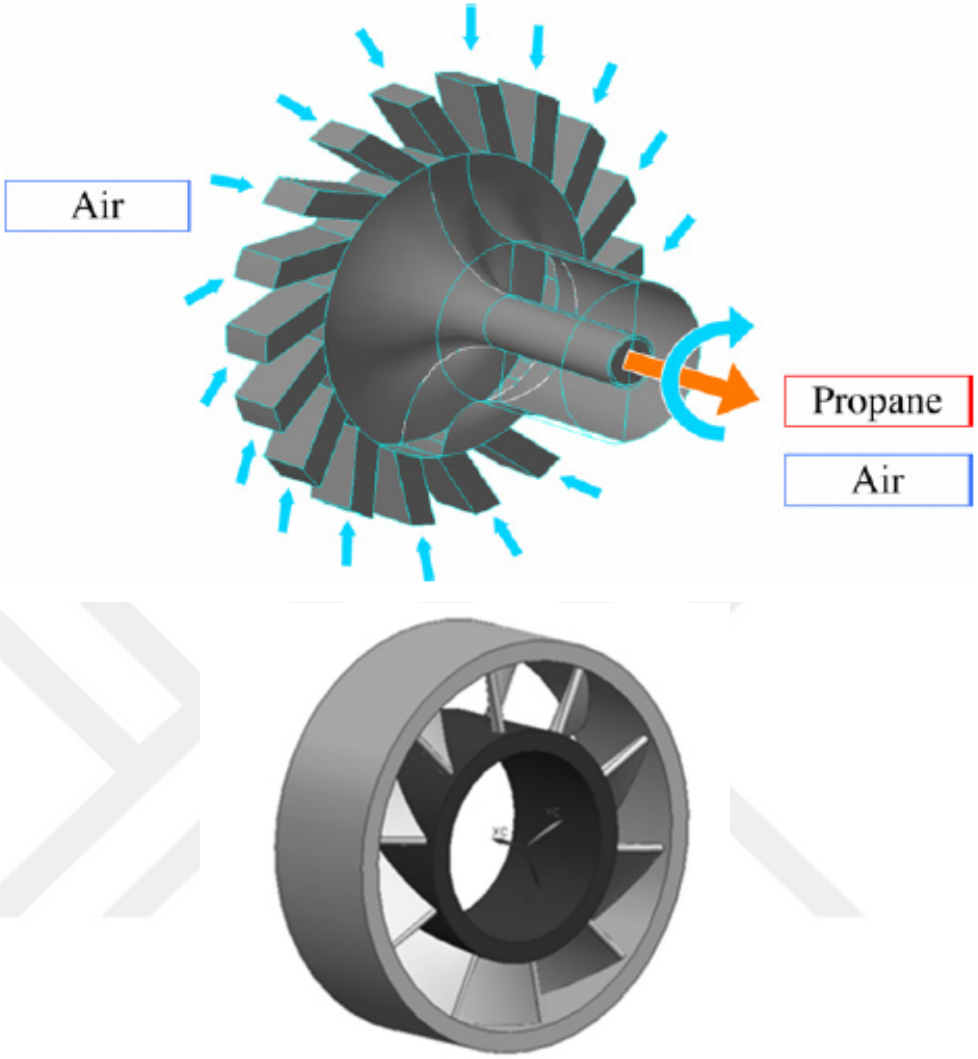


Figure 1.4: Axial and radial swirlers

Table 1.1: Swirler-Injector Configurations [9]

Combustor	Injector Type	Swirler Type
GE-DACRS	Dual annular	Counterswirl
LDI	Single/Multi	Helical
GE-TAPS	Twin annular	Cyclone
GE-CFM56	Single	Dual-swirl radial
VESTA	Multi	Dual stage

In combustion chambers, different types of vortex breakdown bubbles are observed depending on the flow rate, swirl number (SN), and the confinement ratio (ratio of the cross-section area of the combustion chamber to the swirler exit area). For example, bubble-type vortex breakdown is observed at higher Reynolds numbers, whereas double-helical vortex breakdown is observed at lower Reynolds numbers which are shown in Fig. 1.5 [10]. The other common type of vortex breakdown observed in the combustors is the conical type vortex breakdown. Moise et al. [11] showed the effect of the confinement ratio on the conical type vortex breakdown. As the confinement ratio increases, conical type vortex breakdown turns into a wide-open conical type vortex breakdown, and a larger recirculation zone occurs, as shown in Fig. 1.6.

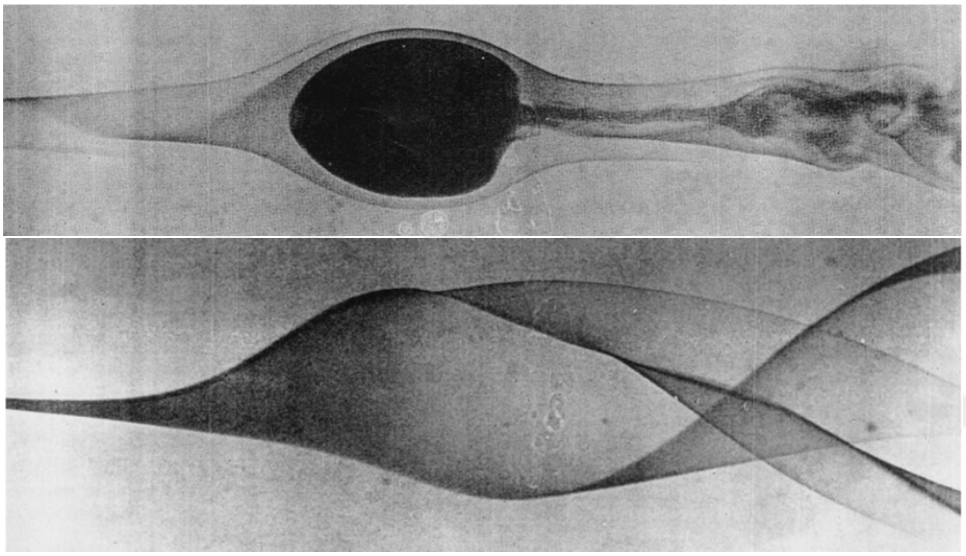


Figure 1.5: Bubble (upper) and double-helix (lower) type vortex breakdown [10]

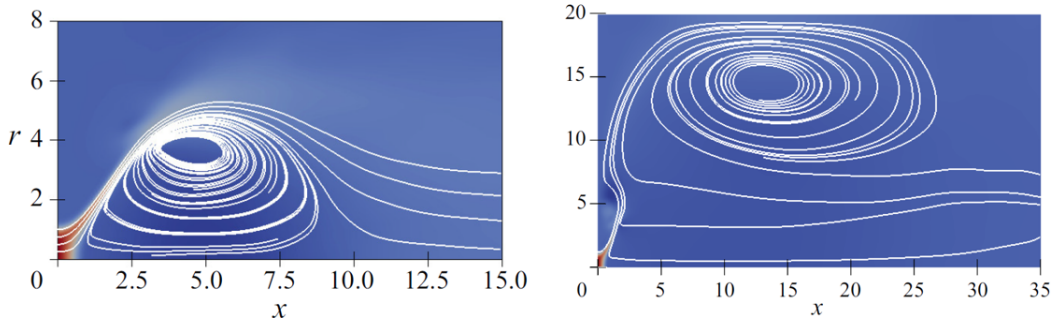


Figure 1.6: Regular (left) and wide-open (right) type conical vortex breakdown [11]

Another stability factor of the swirling flows (rather than vortex breakdown) is the

Precessing Vortex Core (PVC). The PVC is a helical structure that causes the vortex to precess around the swirler axis. The schematic of the PVC motion is shown in Fig. 1.7. The importance of the PVC comes out concerning combustion instability, which is also called dynamic stability. This phenomenon refers to the large scale of pressure and temperature oscillations inside the combustors. When large amplitude oscillations are coupled, higher heat transfer rates occur, leading to significant thermal stress levels. Eventually, the structure of the combustion chambers can be damaged, or the flame can blow-off. The combustion instability loop can be seen in Fig. 1.8. The PVC changes the CTRZ structure and flame shape. When the flame shape is corrugated, the flame surface area varies, and it causes heat release. The heat release rate changes the flow field, and the strength of the PVC can increase, or the PVC can disappear. This loop continues until a limit, then the combustion instability occurs. That is why understanding the PVC's nature is crucial for stable combustion systems.

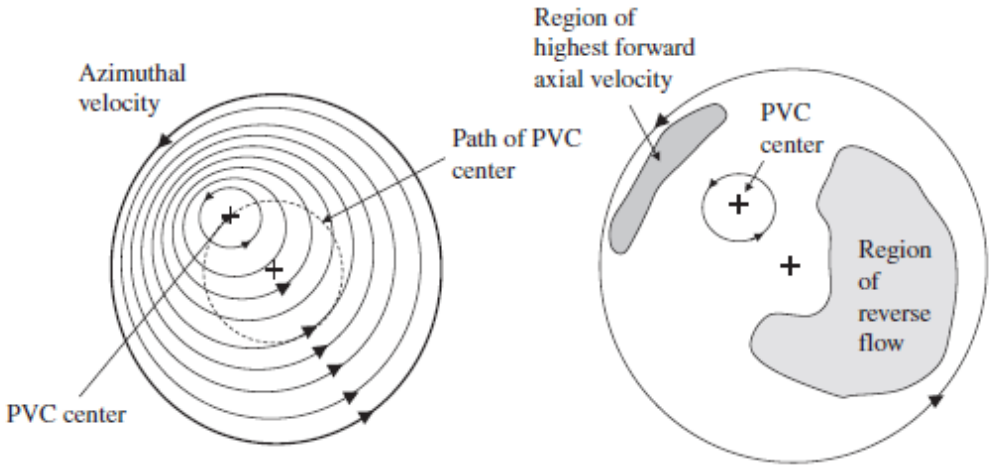


Figure 1.7: Schematic of the PVC motion [4]

Performance of the swirlers can be enhanced by using them in multiple configurations [13], and one of the most common types is the radial-radial swirler. In this configuration, the fuel injector (i.e., atomizer) is located at the center of the primary swirler (inner air flow). Generally, the SN of the primary swirling flow is lower than that of the secondary swirler (outer air flow), and the schematic of the configuration is shown in Fig 1.9 [14]. The air and fuel mixing starts in the primary swirler, and the fuel droplets are transported to the reaction zone of the combustor by the primary swirling flow. In addition, the primary swirling flow reduces the break-up length [15]

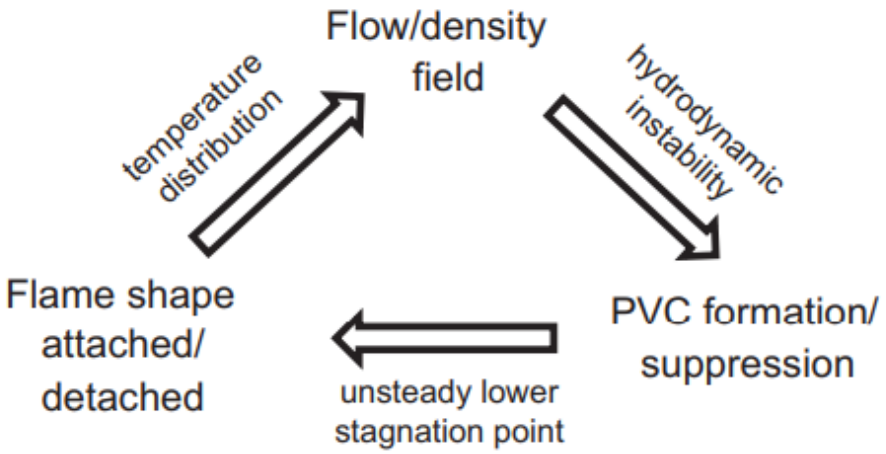


Figure 1.8: Combustion instability loop [12]

and helps to reduce the sheet thickness of the fuel droplets on the primary swirler wall, which directly affects the mean droplet size, combustion efficiency, and level of emission [16]. The secondary swirler, on the other hand, introduces higher momentum swirling flow which is responsible for creating CTRZ.

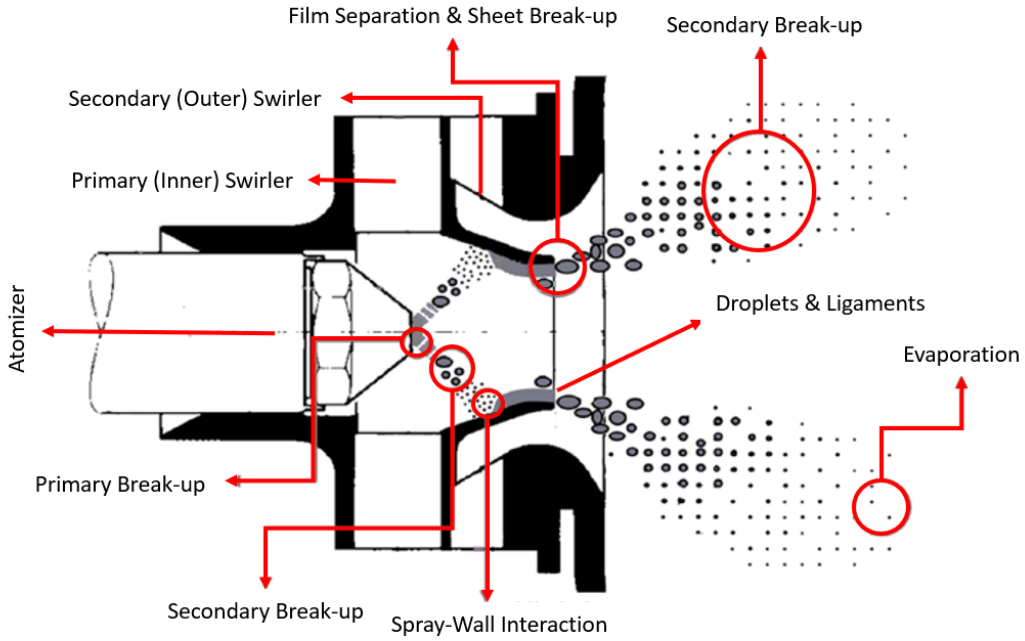


Figure 1.9: Schematic of a radial-radial type swirler

Radial-radial swirlers are affected by several parameters as listed below, and these components are shown in a schematic in Fig. 1.10 [17]. In this section, the design parameters relevant to this study are shown.

- Sense of rotation
- Confinement ratio
- Swirl number
- Mass-flow split between channels
- Venturi diameter
- Venturi shape
- Flare angle
- Secondary swirler diameter
- Swirler vane shape
- Swirler vane number
- Fuel nozzle position

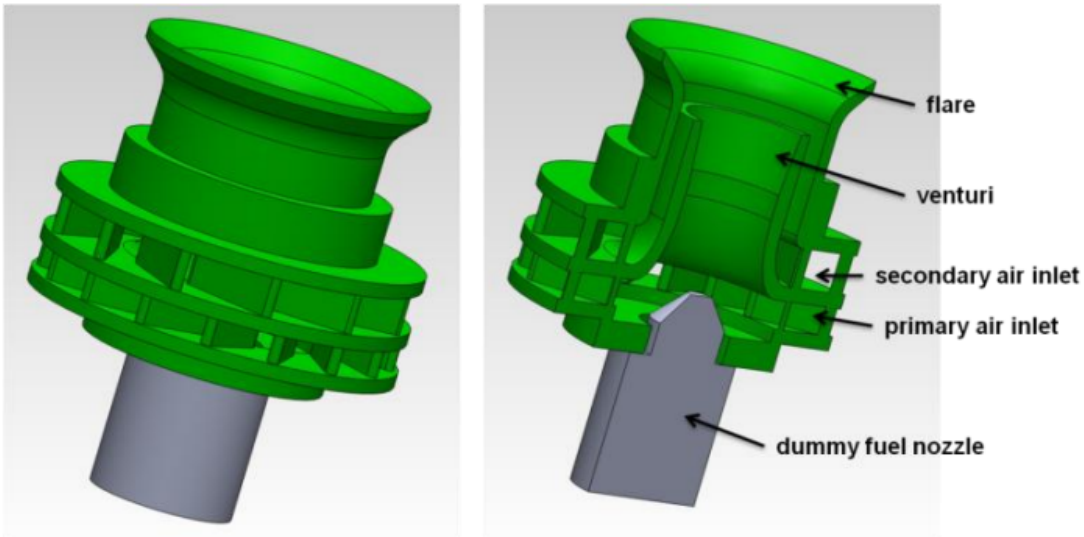


Figure 1.10: Radial-radial type swirler parts [17]

1.1 Effect of the channel orientation

Orientation of the swirler channels is reported to influence the combustion efficiency, fuel atomization, stability limits, and recirculating mass flow rate. Sung and Choi [18] investigated the sense of rotation in an axial-axial type swirler using PIV and OH/CH-chemiluminescence techniques in reactive conditions by changing the orientation of the primary swirler. They stated that flame shape changes from a heart-shaped structure to an elongated structure by changing the sense of rotation from CO to CR. Due to better mixing, the CR configuration provides a higher temperature distribution than the CO structure.

A similar study was performed by Degeneve et al. in both reactive and non-reactive conditions for axial-axial type swirler configurations [19] using PIV with OH-Planar Laser-Induced Fluorescence techniques. In the isothermal conditions, a higher amount of flow recirculates, and longer CTRZ is observed in the CO swirler. For the reacting conditions, an elongated flame structure is observed in the CR configuration, while a more compact flame is observed in the CO configuration.

The other study was conducted by Merkle et al. using radial-radial type swirler configurations to investigate stability limits using the Laser Doppler Anemometry technique [20]. The sense of rotation was adjusted by changing the orientation of the secondary swirler. In the isothermal conditions, an additional vortex appears right after the swirler exit, and more air recirculates in the CR configuration. Also, they investigated the effect of channel rotation on turbulent mixing. Their results showed that in the CO configuration, faster mixing was observed. In addition, they showed that the CR swirler provides a higher thermal load with a larger stability limit than the CO swirler.

Hadef and Lenze performed a study to compare the effect of the swirler orientation on the droplet characteristics of a spray flame by using the dual-phase Doppler anemometry technique [14]. The U-shaped flame was observed for both swirler types in their study, and it means that the flow attaches to the dome section of the burner. Even though the flame shape structure and droplet size distribution are similar, the CR configuration provides more turbulent droplet motion. In the CR configuration, more

droplets accumulated near the centerline of the burner axis, which is responsible for better flame stability. Also, finer atomization and a higher level of turbulence were observed in the CR swirler configuration, which provides higher efficiency combustion thanks to better mixing.

Gupta et al. [21] investigated premixed flames experimentally using the CO and the CR swirler configurations and observed remarkable differences. In the CO swirler case, a larger reaction zone with more minor temperature fluctuations was observed, while the magnitude of the fluctuation increases in the CR swirler due to the intense reaction zone. This resulted in a non-symmetrical reaction zone in the CR swirler while the CO swirler provided homogeneous temperature distribution.

Li and Gutmark conducted a similar study to investigate the Lean-Direct Injection burner at reacting and isothermal conditions [22] under atmospheric conditions. They stated that the sense of rotation of the swirler affected the axial and the tangential velocity profiles, which impacted turbulence level, flame structure, and emission levels regardless of the fuel type. The CO swirler provided minimum emission levels compared with the CR swirler. The main difference is that the CO swirler reduces mixing time and increases reaction time, resulting in better combustion than the CR swirler. Thus, it resulted in a lower emission and temperature distribution level for the CO swirler.

Bolat and Uslu conducted a numerical study to observe the effect of the channel orientation of radial-radial type swirlers on the performance of an annular combustor [23]. According to their results, centerline temperature was almost identical. Also, hot spot locations at the outlet were different, and a more desirable exit temperature distribution was obtained in the CO swirler. Both configurations provided the same combustion efficiency, but a higher emission level was observed in the CR swirler configuration.

Even though several studies exist regarding channel rotation, they do not provide any information about the relation under the different confinement ratio levels. Moreover, the effect of the channel orientation on the coherent structures has not been conducted deeply.

1.2 Effect of the confinement ratio

The confinement ratio is another critical design parameter affecting the swirler performance. The confinement ratio is defined as the ratio of the flame tube's cross-section area to the jet exit's cross-section area. Kiyici and Percin [24] investigated the effect of the confinement ratio on the performance of a CR radial-radial type swirler by using a 2D-2C PIV system in isothermal conditions. Their results showed that the confinement has essential effects on the swirling flow field, and as the CR increases, the expansion angle decreases. Interestingly, as the confinement ratio increases, two central recirculation zone was observed for the highest confinement ratio case among the confined cases.

A similar study for a CR radial-radial type swirler was performed by Fu et al. [25] using a pointwise measurement technique of laser Doppler anemometry. They concluded that the mean behavior of the CTRZ was remarkably affected by the confinement ratio, and the number of the recirculation zone increases as the confinement ratio increases. This affected the turbulence generation, and two peaks were observed at higher confinement ratio cases while it reduced a single peak at lower confinement ratio cases. They also stated that the secondary swirler dominates the flow field, which has a five-time higher flow area than the primary swirler.

Cai et al. [26] studied the effect of the confinement on the CR radial-radial swirler by using a phase-locked PIV measurement in isothermal conditions. In addition, they recorded noise data by a microphone to extract frequency information. They observed two coherent structures: PVC as an azimuthal mode and large-scale vortices shedding as a longitudinal mode. The confinement ratio is more effective in suppressing the PVC, whereas it is less effective on the dynamics of the vortices shedding. They found that a linear relationship exists between acoustics and the Reynolds number. The PVC affected the velocity components near the swirler exit, but it suddenly decays far from the jet exit. Also, they stated that the PVC leads to asymmetrical CTRZ structure in circumferential directions. However, large-scale vortices showed longitudinal mode structure, which changes the flow field symmetrically, and its effect can be observed at more downstream locations.

In another study, the effect of the confinement ratio on the flame characteristics of a CR axial-axial swirler was investigated by Zeng et al. [27]. They showed that the confinement ratio changes the flame structure and the combustion efficiency as well. They stated that soot formation was not observed in the medium confinement ratio case. However, it gradually develops as the confinement ratio changes. Also, the centerline velocity distribution was affected by the confinement ratio. Longer CTRZ was observed as the confinement ratio was increased.

Ji et al. investigated the effect of the confinement and the confinement ratio on the blow-off characteristics of a single-axial swirler [28]. They observed that the blow-off limits of a combustor increase as the confinement ratio increases. They revealed the stability mechanisms of confined and unconfined situations. They found that the shear layer and CTRZ have crucial importance in stabilizing the flame front where the flame is far away and close to blow-off under the unconfined condition. However, the shear layer and CRZ helps to stabilize the flame when it is far away from blow-off under confined condition. At lower fuel-air ratio levels, the effect of CRZ decreases for stabilization. They stated that, close to the blow-off conditions, the flame is stabilized by CTRZ at a lower confinement ratio while shear layer interaction is getting more critical in higher confinement ratio cases.

These studies have provided valuable findings to the literature but did not include any information about the changes in coherent structures under the different confinement ratio levels. Moreover, types of vortex breakdown for multiple swirler configurations have not been investigated thoroughly.

1.3 The coherent structures

Higher swirling momentum could trigger a helical mode instability that is called PVC. The PVC is defined as a periodical motion around the instantaneous center of the vortex core, which is different from the center of the swirler [29]. The PVC is caused by vortex breakdown and emerges as a global instability mode obtained from linear stability of the supercritical Hopf bifurcation [30]. The dynamics of the flow field determine its frequency instead of the combustion chamber [31]. The frequency of the

PVC is linearly affected by the flow rate, but it might not be coupled with the rotation rate of the flow [32]. The existence of the PVC is the function of different parameters such as equivalence ratio, confinement ratio, SN, and the flame shape [29]. The PVC can influence the combustor dynamics either positively or negatively. For example, the PVC can increase the mixing of fuel-air mixture [33], [34] it can be coupled with the thermoacoustic oscillations of the burner [35]. In literature, the effect of some parameters, such as high or low momentum axial injection [36], [37], SN [38], exit boundary condition [39], on the dynamics of the PVC has been investigated. However, the effect of channel orientation has not been investigated thoroughly.

Several examples can be found to identify the coherent structures in the literature that reveal the dynamics of the swirling flow field in both reacting and isothermal conditions. The coherent structures can be defined as the energy-containing large-scale periodic turbulent structures [40]. The turbulence structures in the combustor are harder to identify due to the interaction of multiple flow phenomena such as shear layer-recirculation zone interaction, wall-shear layer interaction, and multiple swirling jet interaction. In order to identify these structures, modal decomposition methods are used [41] and one of the most commonly used is the Proper Orthogonal Decomposition (POD). The purpose of the POD is to construct a basis of the modes that maximizes the turbulent kinetic energy with few modes.

Percin et al. [7] conducted snapshot POD to pressure fields of a 3D flow field that was obtained by tomographic-PIV. The swirl was generated by variable guide vanes of a single axial swirler. The SN of this study was around 0.4. They observed that the precessing helical mode structure is the most dominant flow structure, and it precesses at a Strouhal number of 0.27. They revealed that the first 60 POD modes capture 50 percent of the total energy of the flow field. They also observed a double-helical structure in addition to a single helical mode shape.

Terhaar et al. [42] decomposed the flow field using the vorticity fields for isothermal and three different flame shape conditions for a swirl burner using the POD. They showed that a helical instability mode of PVC appears in isothermal and reactive conditions (annular and trumpet-like flame) except in the V-flame structure, where the shear layer interaction is observed as the most dominant mode. They also stated that

the PVC frequency in reacting conditions is lower than in the isothermal condition.

Oberleithner et al. [12] applied POD on instantaneous velocity fields of a confined swirl burner with a single radial swirler. They compared the isothermal and two reactive conditions (low and high power cases at the same fuel/air ratio). POD results showed that PVC structure exists in isothermal and high-power reacting cases while it disappears in the low-power reacting case. Similar to the [42] study, PVC did not exist in the V-shaped flame case.

Especially for highly chaotic flows, the POD fails to extract modes due to maximization of the energy content, which results in the merging of several modes. A solution to the drawback is Spectral-Proper Orthogonal Decomposition (S-POD). S-POD employs a Gaussian low-pass filter (acts as a band-pass filter) to separate coherent structures [43]. The POD and S-POD results were compared in isothermal conditions of a swirl burner by Sieber et al. [43] using the radial velocity components for decomposition. According to their results, applying a bandwidth filter results in clear frequency peaks in S-POD modes, while the peaks can not be identified in POD modes. Even a global hydrodynamic instability mode (see [30]) was observed as the first POD mode clearly, the single and double helical modes were noisy. Thus, clear frequency peaks were not obtained from POD analysis which was more distinct in the S-POD modes and remarkable frequency peaks were also obtained.

A similar comparison was performed by Sieber et al. [44]. They applied POD and S-POD to the instantaneous radial velocity components of the flow field. First two modes of the POD and the S-POD were similar, but type II PVC mode was not observed in the POD modes. Additionally, they used OH* chemiluminescence to construct OH* modes, and this approach provides the heat release rate distribution and also relates all structures with the spatial fluctuations of it. As mentioned above, the PVC structure has an anti-symmetric helical mode shape. If the radial velocity component is used for coherent structure identification, symmetric and anti-symmetric flow structures can be defined as shown in Fig. 1.11 [44].

Oberleithner et al. [45] performed classical POD and S-POD on the flow field of the test article, which was presented by [7] Percin et al. before. They stated that the flow field is highly chaotic even though the test section has a simple configuration.

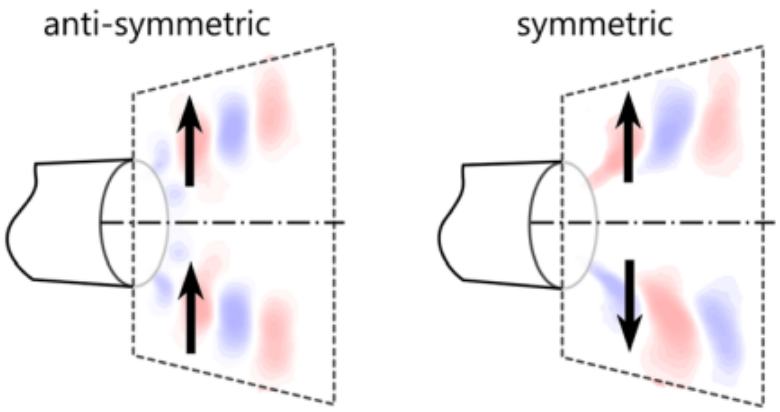


Figure 1.11: Symmetric and anti-symmetric mode shape structures [44]

They extracted two distinct mode shapes as single and double helical structures. They reported that their energy contents are very low; thus, the POD fails to extract these modes, and these mode structures affect the other mode structures. S-POD found the distinct frequency peaks of these two mode shapes as Strouhal number of 0.273 for single helical mode structure and 0.536 for double helical mode structure. In addition, snapshot-POD analysis of [7] also provided the Strouhal number of 0.27 for the single helical mode shape. Oberleithner et al. [45] also stated that the single helical structure extracts energy from the interaction of the vortex breakdown bubble and swirling jet.

Mason et al. [39] investigated the effect of the exit boundary conditions on the dynamics of PVC using radial velocity component with the S-POD technique. S-POD provided similar PVC frequency values with the pressure transducer data, which has a higher frequency resolution than the PIV. They showed that the frequency of the PVC is insensitive to exit boundary conditions while the amplitude of the PVC is remarkably sensitive to it. Also, the frequency of the PVC increases as the SN increases.

Karmarkar et al. [38] provided radial mode shape of the PVC for different SN values using S-POD. As the SN increases, the PVC structure becomes more coherent, moves upstream, and additional frequency peaks are observed at higher frequencies. They also showed that the frequency jitter is not insensitive to turbulence after a limit SN value.

Shen et al. [46] performed POD and S-POD analysis on instantaneous LES data

of confined and unconfined cases of a lean direct injection burner under isothermal conditions. Swirl was generated by using a CR swirler where the SN was equal to 0.7. They stated that POD fails to identify distinct features of the swirling flow field while S-POD extracts the single and double helical flow structures. They stated that the single helical mode shape frequency was almost insensitive to confinement walls. However, confinement changed the frequency of the double-helical mode shape remarkably. The coherent structure identification of their study showed that single and double helical structures occur in the inner shear layer of the flow.

1.4 Motivation and objectives

In the literature, a limited amount of studies have investigated the effect of confinement ratio and channel orientation on the performance of the radial-radial type swirlers. These studies were mostly performed using pointwise measurement techniques and did not provide any information on the coherent structures. In addition, the combined effect of channel orientation and coherent structures has not been performed yet. Moreover, numerical studies of the radial-radial type swirlers have not included the effect of the confinement ratio on the flow fields of the CO and CR swirlers.

In this study, the effect of the confinement ratio on CO and CR swirlers is investigated experimentally and numerically. The primary concern of this study is to understand how the confinement ratio changes the time-averaged flow fields of the CO and CR swirlers. The other objective is to detailly identify the global instability mechanism and coherent structures. Especially, PVC is highly crucial in terms of combustion performance and combustion instability. Thus, the confinement and channel orientation effects on the PVC dynamics are the other concern of this thesis. In addition to experimental findings, the other objective of this thesis is numerical simulations. LES and RANS simulations are performed to observe the performance of the numerical tools under different geometrical conditions for CO and CR swirlers to obtain the best-possible numerical schemes and mesh strategy options.

1.5 Structure of the thesis

The structure of the thesis is organized as follows. Chapter 1 identifies the architecture of the turbomachinery components and the combustion chamber. Significantly, the purpose of the swirlers in the combustion chamber is clarified. In addition, the effect of the geometrical parameters on the time-averaged and time-resolved swirling flow is summarized. The next chapter presents experimental facility, PIV and numerical setups, and modal analysis methods. In the following chapter effect of the confinement ration on the CO and CR swirlers is presented using time-averaged and time-resolved experimental data. Also, RANS and LES results are compared to experimental data to observe their performance under different conditions. Furthermore, modal analysis results show how the confinement ratio changes the dominant structures of the CO and CR swirlers flow field. In chapter 4, the findings of the present study are summarized. In the last chapter, the CANTEC-SD burner is presented as future work.

CHAPTER 2

METHODOLOGY

This section presents the experimental and numerical setup and modal analysis methods. The experimental setup section describes the experimental facility, the CO and CR swirler configurations, the confinement geometries, the measurement instruments, the PIV method, data recording strategies, and the error estimation methodology. Next, the numerical setup is presented. This section starts with the governing equations, and solution algorithms are also defined. Subsequently, the eddy viscosity-based turbulence modeling and LES methodology are represented. In the modal analysis section, POD and S-POD methods are shown.

2.1 Experimental Setup

2.1.1 Experimental Facility

The experiments are conducted at the Center for Wind Energy Research (RÜZGEM) of Middle East Technical University (METU). The schematic of the experimental facility is shown in Fig. 2.1. A compressor system supplies pressurized dry air split into two streams, i.e., the mainstream and the Laskin nozzle stream, after the first regulator, shown in Fig. 2.2. Subsequently, air enters the control unit, including a fine adjustment valve, plug socket, and second pressure regulator. The air stream goes through a Micro Motion Coriolis F050S type flow meter (see Fig. 2.3). The mass flow rate for the dry air is 12.9 g/s for all experiments. The mass flow rate is recorded at a rate of 100 Hz for a time interval of 120 seconds for three different connection types before the flow meter, which are listed in Table 2.1. A relatively smaller oscillation magnitude is obtained from Configuration 3 and causes bulk velocity uncertainty of

$\pm$ 0.1 m/s, which is considered negligible.

Table 2.1: Control unit configurations

Configuration Number	Configuration Type	Standard Deviation
1	Valve-Regulator	0.056
2	Valve-Regulator-Socket Plug	0.058
3	Valve-Socket Plug-Regulator	0.046

After the desired mass flow rate is obtained, the flow is then introduced into the mixing chamber radially through four inlets. The seeding particles enter the mixing chamber axially along the center to obtain a homogeneous air-seeding mixture (see Fig. 2.4). Subsequently, the air-seeding material mixture pass through a relatively long settling chamber (the length of the settling chamber is 1200 mm, which is ten times its hydraulic diameter) to obtain a uniform velocity profile at the inlet of the swirler to prevent uncertainties from the inlet. A turbulence screen is located at the mid-length position of the settling chamber to break up large-scale structures. The settling chamber and the screen are shown in Fig. 2.5. The distance between confinement walls and the black plate is higher than three times the hydraulic diameter of the settling chamber.

The measured inlet velocity profile close to the settling chamber exit is shown in Fig. 2.6. The mean inlet velocity V_0 is 0.89 m/s, which is used in the normalization of the experimental results. The air-seeding mixture opens to square test sections with cross-section dimensions of 80 mm x 80 mm (low confinement ratio with the confinement ratio of 9), 120 mm x 120 mm (medium confinement ratio with the confinement ratio of 20.4), and 160 mm x 160 mm (high confinement ratio with the confinement ratio of 36.2) with a height of 600 mm, shown in 2.7.

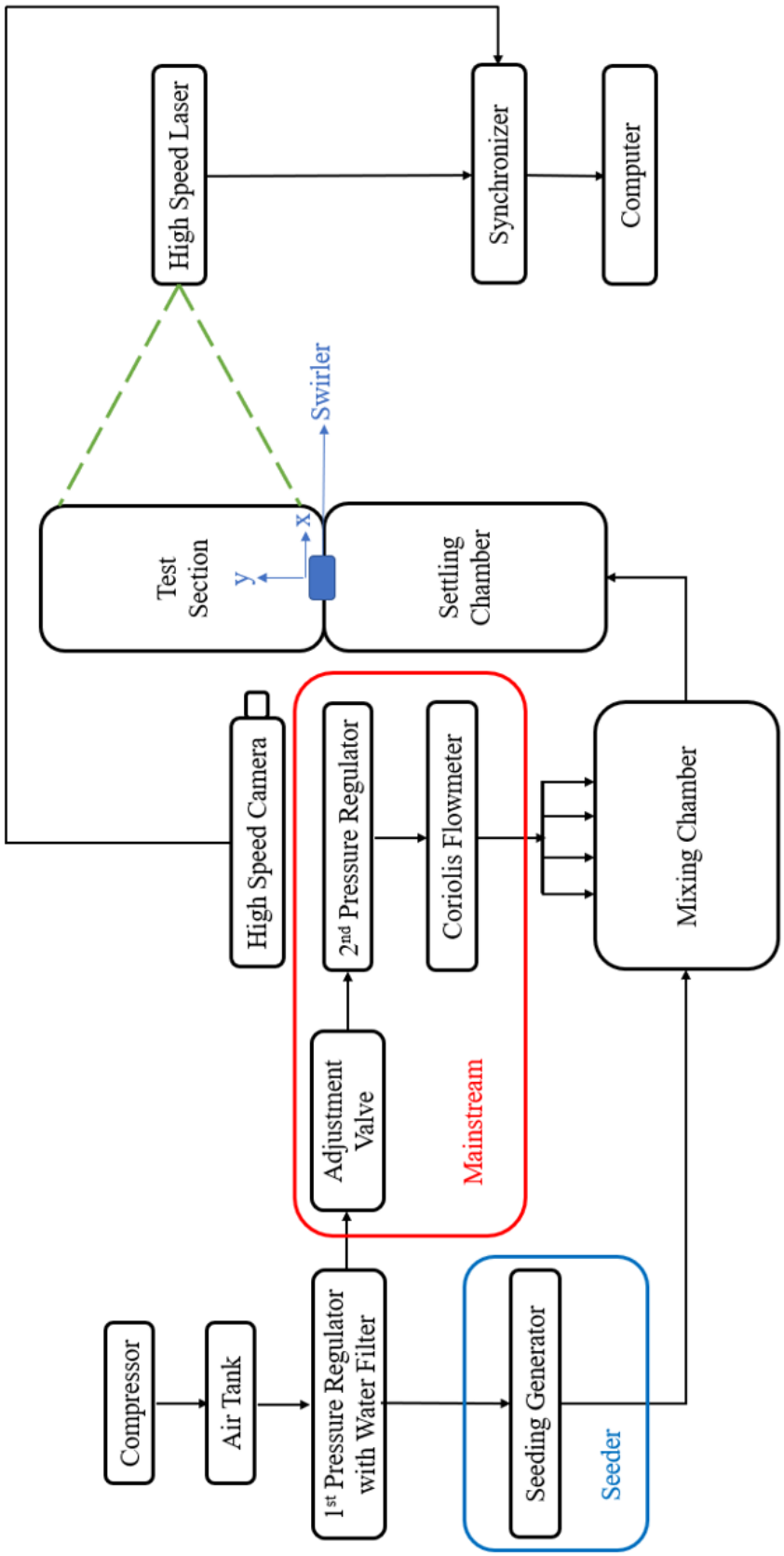


Figure 2.1: Schematic of the experimental facility



Figure 2.2: 1st pressure regulator

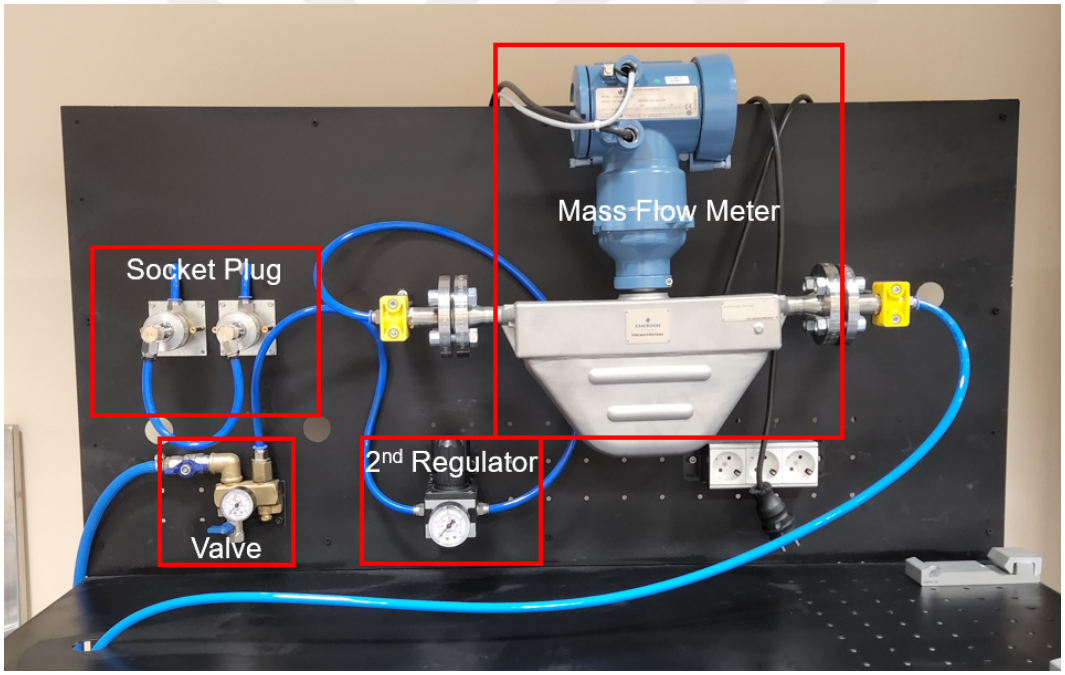


Figure 2.3: Control unit of the experimental facility

2.1.2 Radial-Radial Swirlers

Two different types of radial-radial swirler (i.e., co- and counter-rotating) configurations with the same exit diameter (D_h) of 30 mm and different channel numbers are tested in this study. The corresponding Reynolds number is calculated as 35000 using

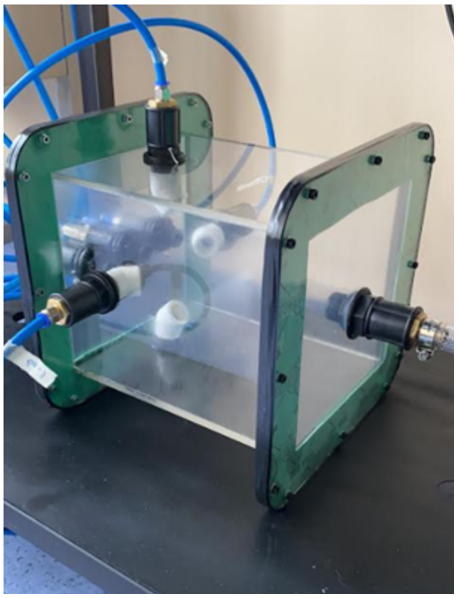


Figure 2.4: Mixing chamber

D_h and mean swirler exit velocity ($V_{jet} = 14.9m/s$). The co-rotating swirler configuration is referred to as CO and the counter-rotating one is as CR. A schematic of the swirler is shown in Fig. 2.8. Both swirlers feature a primary swirler (displayed in brown) with eight radial vanes and a secondary swirler (displayed in green) with ten, twelve, and sixteen radial vanes. In both configurations, the total mass flow rate is distributed by a ratio of 28% and 72% between the primary and the secondary swirler channels, respectively. The angular orientation of the secondary swirler is changed in the design of swirlers to obtain the CO and the CR configurations. The swirl number (SN) values are calculated by integrating the axial and tangential velocity profiles obtained from numerical simulations of the flow fields by using Eqn. (2.1) and (2.2), respectively[6].

$$SN_{pri} = \frac{\int_0^{R_{po}} U_{axial} \cdot U_{tangential} \cdot r^2 dr}{R_{po} \int_0^{R_{po}} U_{axial} \cdot U_{tangential} \cdot r dr} \tag{2.1}$$

$$SN_{sec} = \frac{\int_{R_{si}}^{R_{so}} U_{axial} \cdot U_{tangential} \cdot r^2 dr}{R_{so} \int_{R_{si}}^{R_{so}} U_{axial} \cdot U_{tangential} \cdot r dr} \tag{2.2}$$

In the CO configuration, both primary and secondary swirlers provide a counter-clockwise rotating flow at an SN of 0.65 and 1.4, respectively. In the CR config-

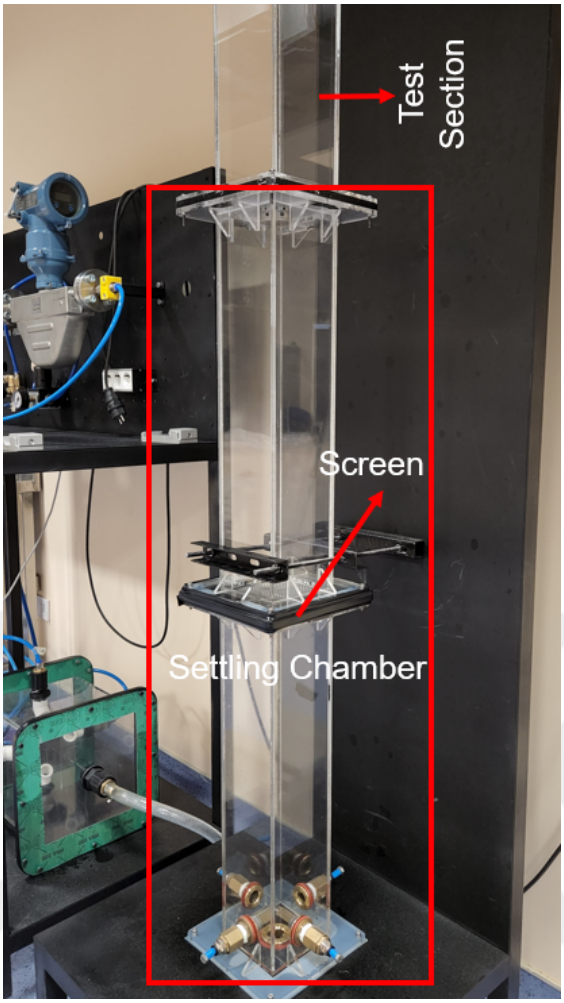


Figure 2.5: Settling chamber and turbulent screen

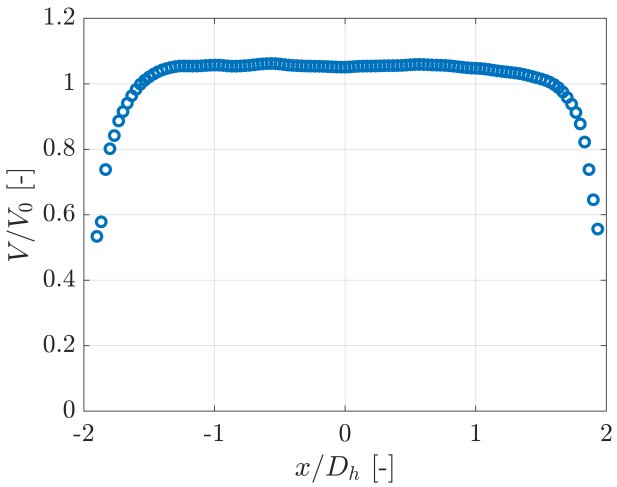


Figure 2.6: Measured normalized inlet velocity profile

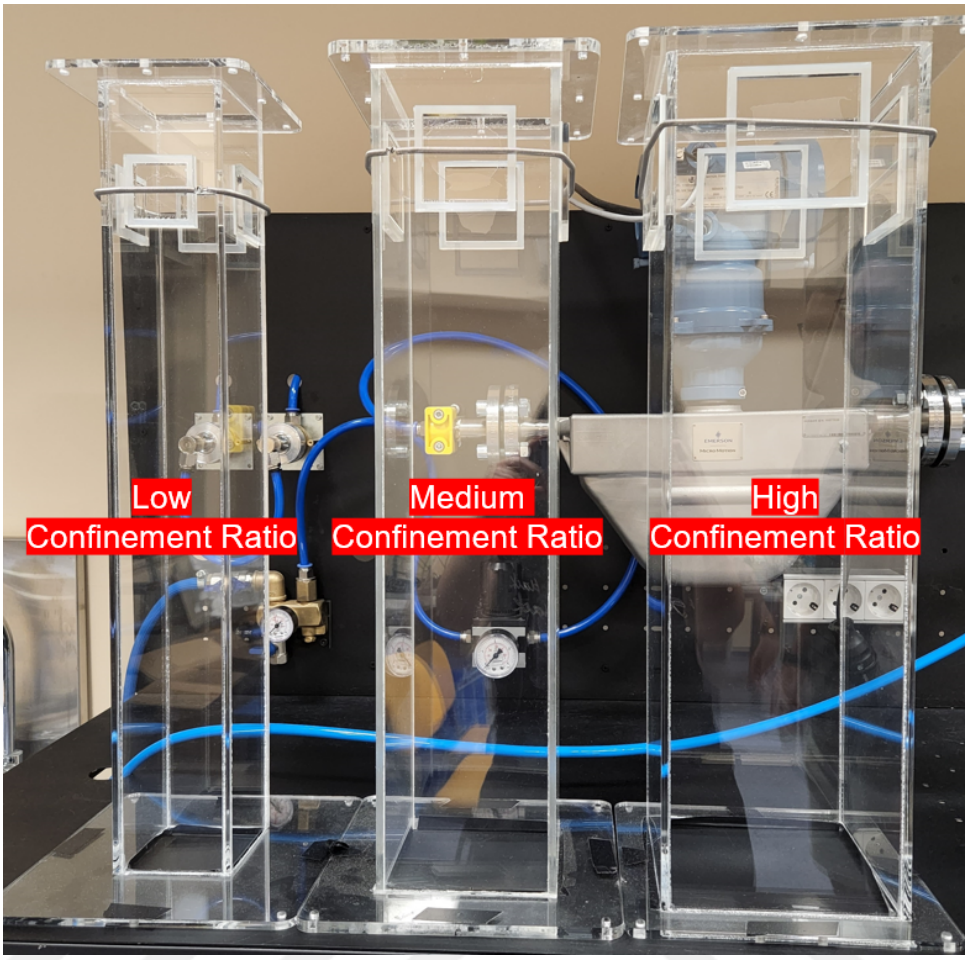


Figure 2.7: Low, medium and high confinement ratio test sections

uration, the primary swirler provides a counter-clockwise rotating flow at an SN of 0.65, while the secondary swirler provides a clockwise rotating flow at an SN of -1.4. The resultant SN is 1.2 for both swirler configurations, which is calculated using Eqn. (2.3) [47].

$$SN_{total} = |SN_{pri} \cdot \frac{\dot{m}_{pri}}{\dot{m}_{total}}| + |SN_{sec} \cdot \frac{\dot{m}_{sec}}{\dot{m}_{total}}| \tag{2.3}$$

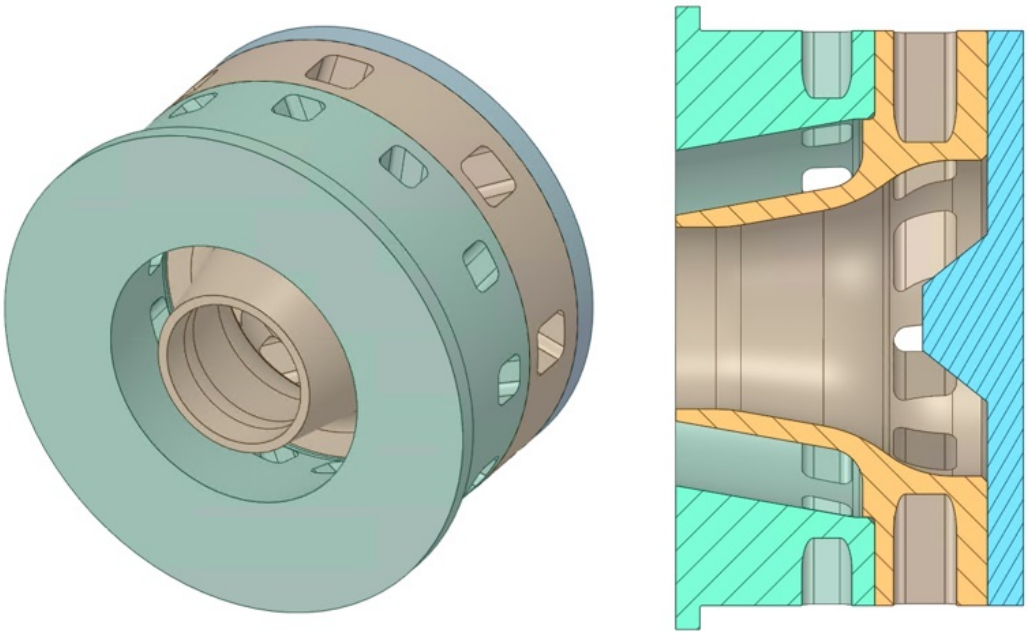


Figure 2.8: Schematic of the radial-radial swirler

2.2 Particle Image Velocimetry

The particle image velocimetry (PIV) is a non-intrusive optical flow visualization technique for obtaining velocity vectors of the illuminated flow field. It is one of the most widely used experimental methods in research and industry for different areas such as turbulence, combustion, micro-channels, flow, and sprays. The PIV system comprises cameras, a seeding particle generator, a laser to illuminate the seeding particles, a synchronizing device to synchronize the laser and camera, and data acquisition and analyzing software. The general structure of the PIV system is shown in Fig. 2.9 [48]. The working principle of the PIV technique is based on capturing the motion of relatively small seeding particles between two consecutive images (see Fig. 2.9, Image frame from pulse 1 and pulse 2) within a time interval (Δt) . The captured images are divided into several windows, which are called interrogation windows, and the total displacement of the seeding particles (Δx) is calculated via statistical algorithms (such as cross-correlation or adaptive-correlation) inside these windows. The magnitude of the flow vectors inside the interrogation windows is calculated by dividing the total displacement to the time interval between the consecutive images.

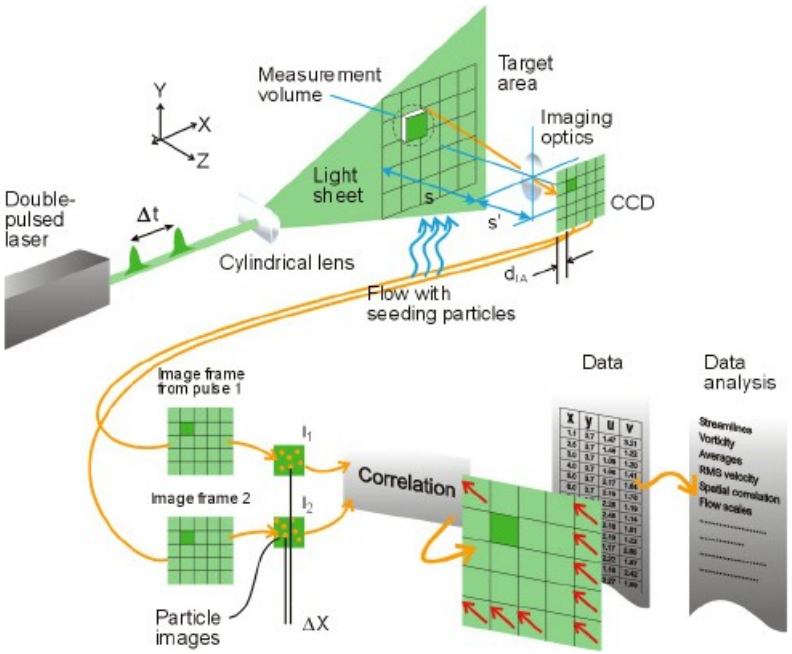


Figure 2.9: Working principle of the PIV system [48]

In this present study, two-dimensional two-component (2D2C) PIV measurements are performed at a streamwise plane aligned with the center of the jet (see Fig. 2.10) and two cross-stream planes corresponding to the axial positions of $y/D_{\mathrm{h}} = 1$ and 3 for three different confinement ratio and unconfined conditions. A Cartesian coordinate system is adapted in the analysis of streamwise plane measurements, whereas the cross-stream measurements are presented in a polar coordinate system which is shown in Fig. 2.11. Accordingly, the x-component of velocity in the streamwise plane corresponds to the radial velocity component in a cross-stream plane. A photo of the experimental setup during the data acquisition is shown in Fig. 2.12.

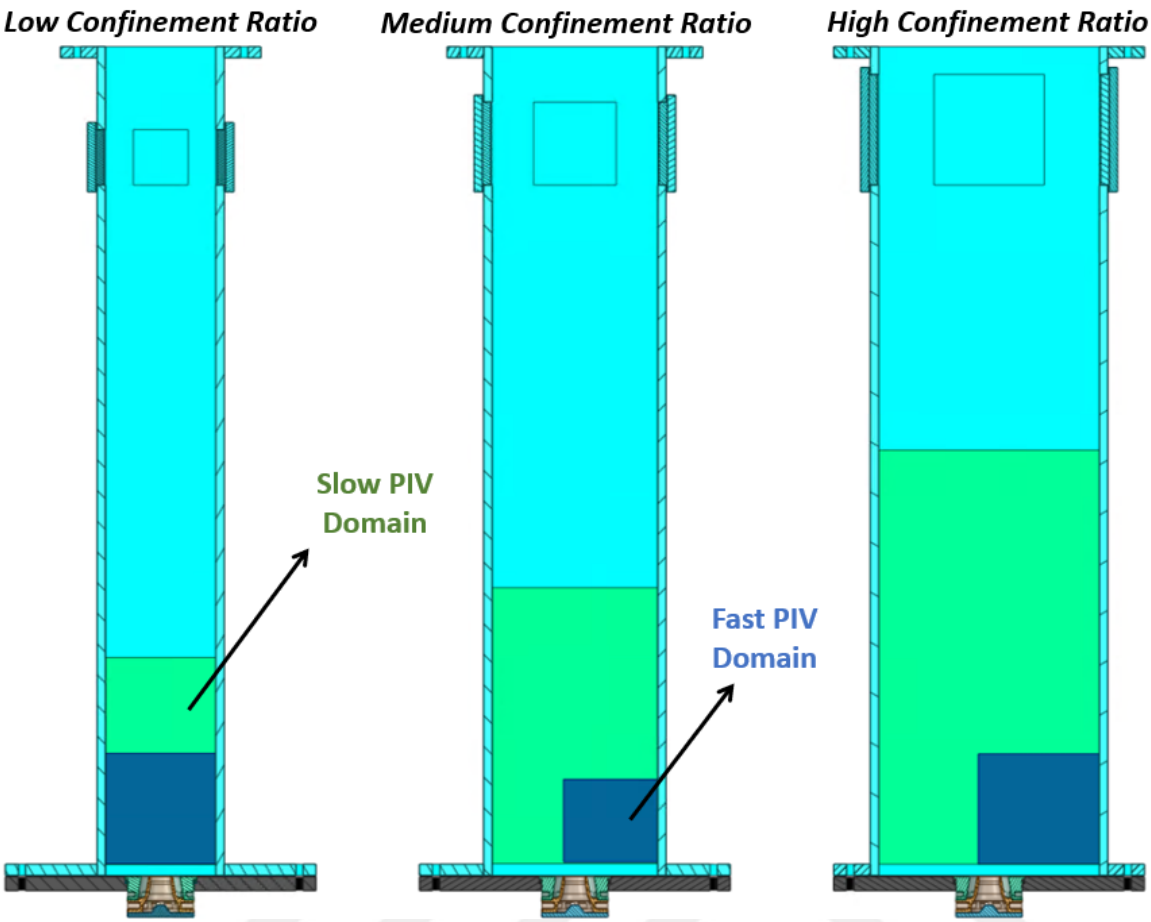


Figure 2.10: Schematic of the slow and fast PIV measurement planes for different confinement ratio conditions

A high-speed Nd:YLF laser (Litron LDY300) with a wavelength of 527 nm illuminates the measurement plane with an approximately 1 mm laser sheet thickness. A high-speed camera, Phantom V641, with a maximum resolution of 2560×1600 pixels at 1500 fps, captures the light scattered by the seeding particles in the image pairs. Image pairs are recorded at two different recording campaigns, slow and fast. In the slow image recording campaign, 2000 image pairs are recorded at a relatively low recording frequency of 200 Hz to allow for a converged statistical analysis by using independent statistical samples and capturing the flow for extended periods. In the fast recording campaign, 6000 image pairs at a rate of 3000 Hz for all confined cases and 8000 image pairs at a rate of 4000 Hz for the unconfined case to visualize time-series phenomena. The slow and fast PIV domains are shown in Fig. 2.10. The slow PIV campaigns' size and vector resolutions are listed in Table 3.4 and the fast PIV

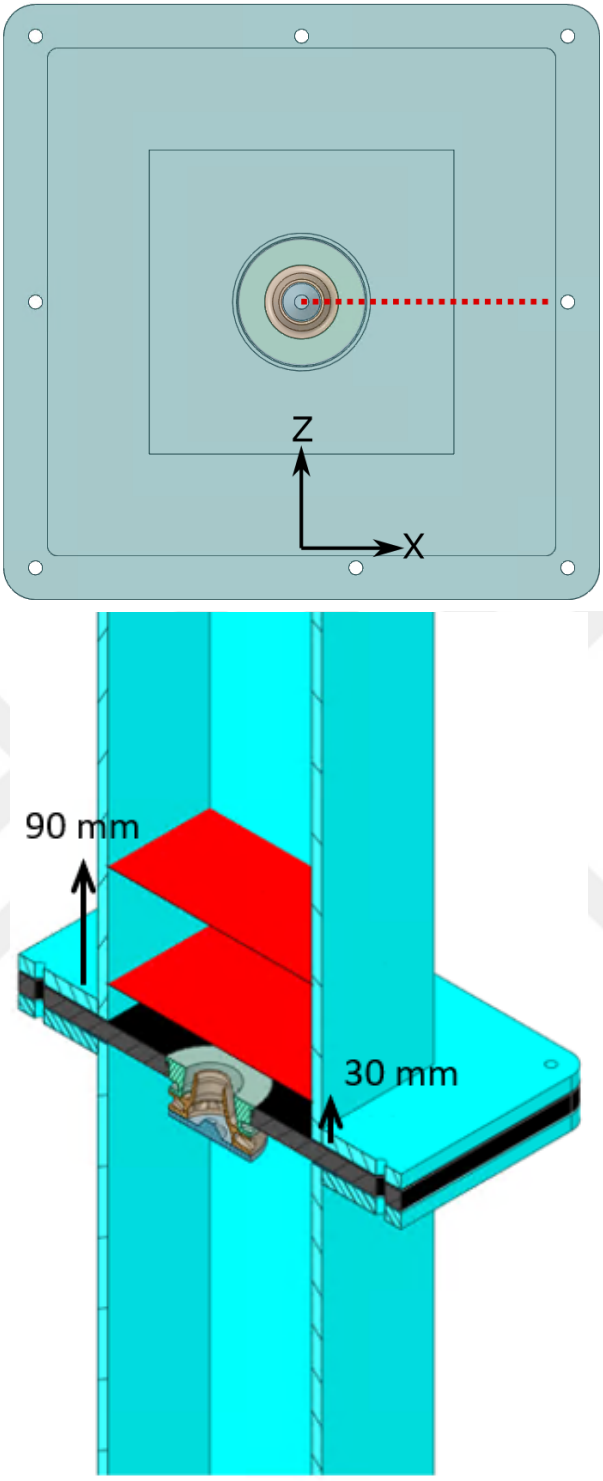


Figure 2.11: Experimental setup for the cross-stream PIV measurements at $y/D_{\mathrm{h}} = 1$ and 3: a sketch showing the adapted coordinate system (left); a schematic of the setup showing the the positions of the measurement planes(right)

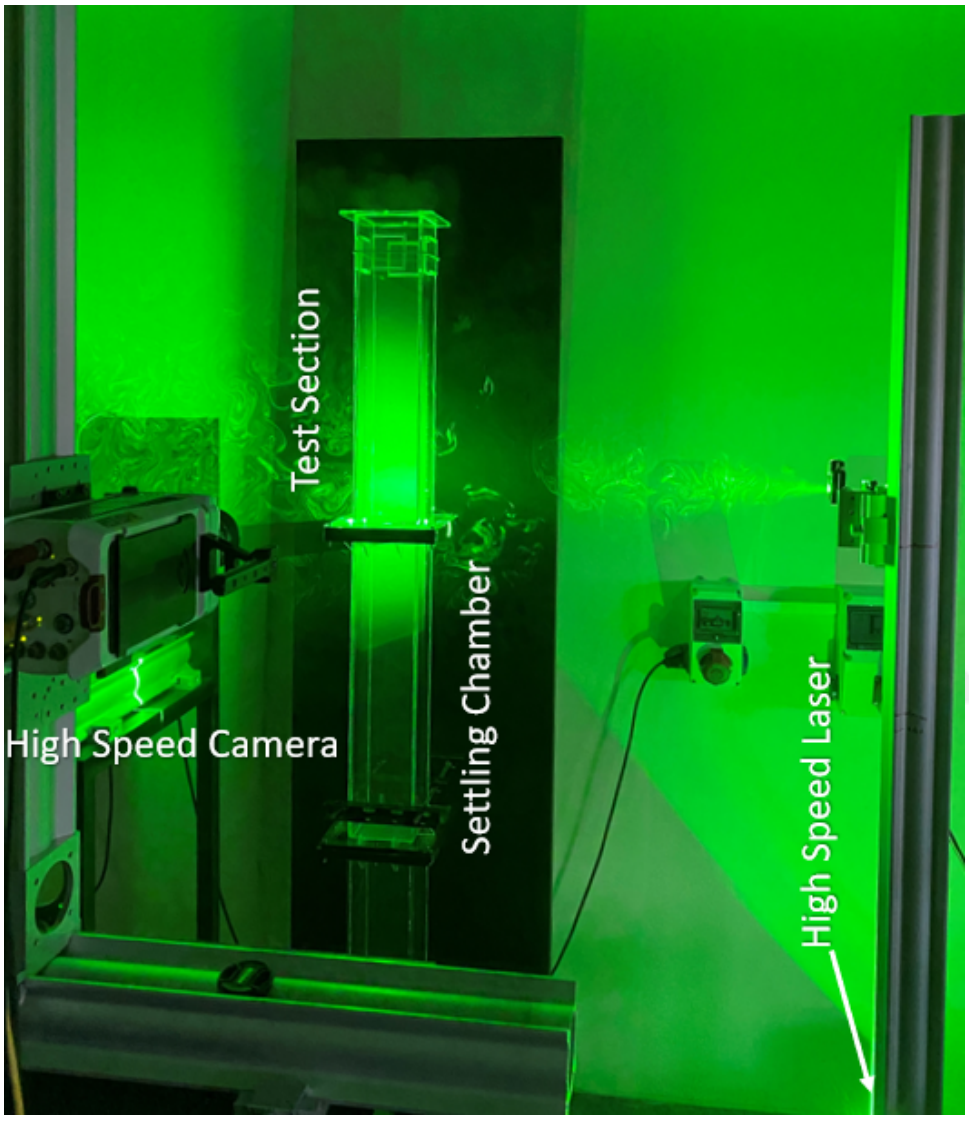


Figure 2.12: A photo of the experimental setup during data acquisition

domain size, vector resolution and the data acqusition frequency is shown in Table 2.3. Data acquisition is performed in TSI Insight 4G. An analysis series including background subtraction, two-step adaptive cross-correlation with a final interrogation window size of 32×32 pixels with a factor of 50% overlap, and the universal outlier detection [49] based on 3×3 cells is applied in Dynamic Studio v2015a.

2.3 Uncertainty Analysis

The error estimation of the PIV data is studied in terms of instantaneous velocity fields and statistical analysis of the time-averaged quantities as conducted by Percin et al. [7]. Random and bias errors in the instantaneous vector field can be caused by various sources regarding measurement devices, data acquisition, and data analysis. First, the divergence field is utilized to estimate the random error of the instantaneous field. In this study, the maximum instantaneous velocity magnitude is far lower than Mach 0.3; thus, the flow can be assumed incompressible. Incompressible flows are also classified as divergence-free flows; thus, the divergence of all the components of the velocity must be zero unless any measurement error [50]. To calculate the random velocity error, $\delta(u)$, Eqn. (2.4) is used with an assumption of uniform random error distribution in both velocity directions. The error in the velocity gradient is computed using a central differencing [50], [51] scheme where the d_v represents the vector spacing. The highest value of the r.m.s of the fluctuating divergence, as averaged over the measurement plane calculated as 0.055 pixels/pixel for the low confinement case of CO swirler. This also corresponds to 0.4 pixels velocity random error for the time interval of image pairs (i.e., 10 μs). In physical units, it returns as $\delta(u)/U_0$ = 1.91 %.

$$\delta(\frac{\partial u_i}{\partial x}) = \frac{1}{d_v}\delta(u) \tag{2.4}$$

2000 statistically independent vector fields are used to compute the first and second-order moments of the flow for statistical analysis of time-averaged quantities. The uncertainty of the measurements is assumed to be normally distributed. Then, the statistical uncertainty can be calculated as in Eqn. (2.5) Eqn. (2.6) and Eqn. (2.7) where $Z_{\alpha/2}$ = 1.96 for a 95% confidence interval and $R_{u_i u_j}$ is the correlation coeffi-

Table 2.2: Slow PIV recording parameters for the mid- and cross-plane measurements

Illumuniation	Nd:YLF, 527 nm wavelength		
Seeding Material	Oil Droplet, d_p =1 nm		
Recording Medium	Phantom V641 high speed camera, 2560x1600 pixels		
Recording Lens	f = 105 mm, f= 5.6		
Planes	Mid-Plane	y/D_h=1	y/D_h=3
Unconfined			
Pulse Delay	10 ms	15 ms	25 ms
Field of View	92 x 145 mm	110x110 mm	100x100 mm
Scale Factor	5.773 pixels/mm	6.912 pixels/mm	6.334 pixels/mm
Dynamic Velocity Range	130	∼120	80
Dynamic Spatial Range	80	∼50	∼50
Low Confinement Ratio			
Planes	Mid-Plane	y/Dh=1	y/Dh=3
Pulse Delay	10 ms	15 ms	25 ms
Field of View	84 x 145 mm	110x110 mm	100x100 mm
Scale Factor	5.773 pixels/mm	6.912 pixels/mm	6.334 pixels/mm
Dynamic Velocity Range	100	∼160	∼110
Dynamic Spatial Range	80	∼50	∼50
Medium Confinement Ratio			
Pulse Delay	10 ms	15 ms	25 ms
Field of View	116 x 200 mm	110 x 110 mm	100 x 100 mm
Scale Factor	7.916 pixels/mm	6.912 pixels/mm	6.334 pixels/mm
Dynamic Velocity Range	∼60	∼150	∼100
Dynamic Spatial Range	80	∼50	∼50
High Confinement Ratio			
Pulse Delay	10 ms	15 ms	25 ms
Field of View	155 x 275 mm	110x110 mm	100 x 100 mm
Scale Factor	11.190 pixels/mm	6.912 pixels/mm	6.334 pixels/mm
Dynamic Velocity Range	∼55	∼90	∼60
Dynamic Spatial Range	80	∼50	∼50

Table 2.3: Domain size, vector resolution and data acquisition frequency for the fast PIV measurements

Confinement Ratio	Domain Size [mm x mm]	Vector Spacing [mm]	Frequency [Hz]
Unconfined	50 x 50	2	4000
Low	72 x 72	2	3000
Medium	70 x 70	1.1	3000
High	86 x 86	2	3000

cient between two fluctuating velocity components. $R_{u_i u_j}$ can be computed as shown in Eqn. 2.8.

$$\delta_{\overline{U_i}} = Z_{\alpha/2}\sqrt{\frac{\overline{u_i^2}}{N}} \tag{2.5}$$

$$\delta_{\overline{u_i}^2} = Z_{\alpha/2}\sqrt{\frac{2\overline{(u_i^2)}^2}{N}} \tag{2.6}$$

$$\delta_{\overline{u_i u_j}} = Z_{\alpha/2}\sqrt{\overline{u_i}^2\,\overline{u_j}^2\left(\frac{1+R_{u_i u_j}^2}{N}\right)} \qquad (i \neq j) \tag{2.7}$$

$$R_{u_i u_j} = \frac{\overline{u_i u_j}}{\sqrt{\overline{u_i}^2\,\overline{u_j}^2}} \tag{2.8}$$

The statistical uncertainty of the first and second-order moments of the flow is averaged up to $y_{D_h} = 2$ and presented in normalized values similar to the study of Percin et al. [7] as shown in Table 2.4 and Table 2.5, respectively. The maximum uncertainty on the mean first and second-order moments is observed in CO swirler under the low confinement ratio condition. Additionally, the uncertainty of the provided mass flow rate is 0.66% and causes bulk velocity uncertainty of $\pm$ 0.1 m/s which is considered as negligible.

In addition to the measurement uncertainty, the mid-plane x-component velocity and the cross-stream radial velocity profiles (the velocity profiles are extracted at the red

Table 2.4: The statistical uncertainty estimates for the Reynolds stresses (mean values calculated in the measurement plane up to $y/D_h = 2$ and mean non-dimensional values normalized by the jet velocity and Reynolds stresses in brackets)

Mean Flow: m/s (x100/V_{jet})

Case=	Low Confinement Ratio		Medium Confinement Ratio	
	CO	CR	CO	CR
$\delta_{\overline{U}}$	0.175 (1.175)	0.128 (0.861)	0.128 (0.857)	0.127 (0.852)
$\delta_{\overline{V}}$	0.161 (1.083)	0.138 (0.923)	0.131 (0.879)	0.144 (0.964)
Case=	High Confinement Ratio		Unconfined	
	CO	CR	CO	CR
$\delta_{\overline{U}}$	0.096 (0.643)	0.143 (0.956)	0.081 (0.542)	0.159 (1.063)
$\delta_{\overline{V}}$	0.100 (0.670)	0.152 (1.022)	0.091 (0.610)	0.151 (1.014)

Table 2.5: The statistical uncertainty estimates for the mean flow (mean values calculated in the measurement plane up to $y/D_h = 2$ with mean of the normalized values in brackets)

Reynolds Stress Components: x100/V_{jet}^2 $(x100/\overline{u_i^2})_{mean}$

Case=	Low Confinement Ratio		Medium Confinement Ratio	
	CO	CR	CO	CR
$\delta_{\overline{u^2}}$	0.630 (15.764)	0.338 (13.275)	0.336 (11.505)	0.331 (11.657)
$\delta_{\overline{v^2}}$	0.535 (14.533)	0.389 (12.387)	0.352 (11.789)	0.425 (12.941)
$\delta_{\overline{uv}}$	0.290 (23.083)	0.181 (18.306)	0.172 (10.082)	0.187 (16.524)
Case=	High Confinement Ratio		Unconfined	
	CO	CR	CO	CR
$\delta_{\overline{u^2}}$	0.189 (8.628)	0.417 (14.672)	0.134 (7.273)	0.516 (12.988)
$\delta_{\overline{v^2}}$	0.205 (8.999)	0.477 (13.717)	0.076 (8.186)	0.336 (13.611)
$\delta_{\overline{uv}}$	0.098 (13.373)	0.223 (18.763)	0.170 (11.661)	0.246 (17.496)

dashed line in Fig. 2.11) are compared to assess the repeatability of the experiments. The results for the medium confinement ratio case of the CR swirler at y/D_{h}= 1 and 3 are shown in Fig. 2.13. The velocity profiles obtained from the streamwise and

cross-stream measurements are almost identical with an RMS error of 0.27 m/s and 0.038 m/s for the y/D_{h} =1 and 3 locations, respectively.

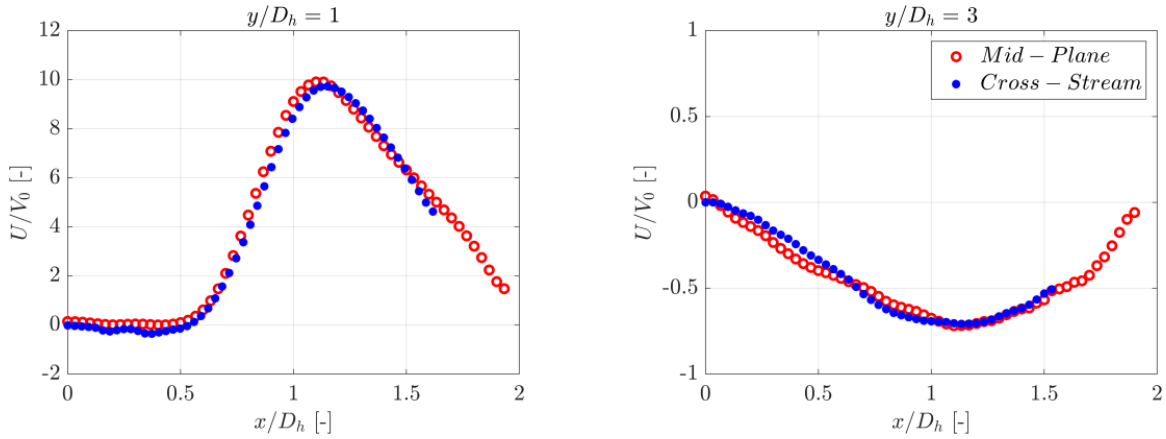


Figure 2.13: Comparison of the time-averaged radial velocity (the velocity component in the x direction, U/V_0) profiles obtained from the mid-plane streamwise PIV measurements and cross-stream PIV measurements at y/D_{h}= 1 & 3

2.4 Numerical Method

This section presents the RANS and LES methodologies. The RANS is used for the confined cases of the CO and CR swirlers. The performances of the RANS and the LES are then compared for the CR swirler in the unconfined condition. The RANS section provides numerical setup, mesh structure, and main differences between commercial and open-source software used in this study. The LES section also mentions numerical setup and LES quality index. In addition to the numerical setup of the LES, a benchmark study will also be provided to ensure proper use of the LES. The numerical validation section shows the RANS and LES performance in a low swirl unconfined benchmark case.

2.4.1 Mathematical Formulation

In this section, Navier-Stokes equations are defined to show the relation between a fluid element's density, pressure, velocity, and temperature. All equations are written in the Einstein notation in the Cartesian coordinates. The first equation is the continuity equation shown in Eqn. 2.9 where the ρ is the density, U is the velocity, t is the time and x is the position vector.

$$\frac{\partial \rho}{\partial t} + \frac{\partial (\rho U_i)}{\partial x_i} = 0 \tag{2.9}$$

The next equation is the conservation of the momentum, which is shown in Eqn. 2.10. In addition to continuity equation, p describes the pressure, f_i describes the body forces due to gravity. In the present simulation, body forces and compressibility are neglected due to the nature of the flow.

$$\frac{\partial (\rho U_i)}{\partial t} + \frac{\partial (\rho U_i U_j)}{\partial x_j} = -\frac{\partial p}{\partial x_i} + \frac{\partial \tau_{ij}}{\partial x_j} + \rho f_i \tag{2.10}$$

In the momentum equation, τ_{ij} is the viscous stress tensor which can be written for incompressible and Newtonian fluid as shown in 2.11. In this equation, μ defines the fluid's dynamic viscosity.

$$\tau_{ij} = \mu(\frac{\partial U_i}{\partial x_j} + \frac{\partial U_j}{\partial x_i}) \tag{2.11}$$

2.4.2 Solution Algorithms

In this study, RANS analysis is conducted in ANSYS Fluent, while LES is performed in OpenFOAM. The reason for using two different software is OpenFOAM is highly time efficient in conducting transient simulations. For example, two or three inner iterations are sufficient to obtain converged residuals in OpenFOAM, while it takes 20-25 iterations in ANSYS Fluent. Thus, OpenFOAM reduces the computational time remarkably.

In this study, RANS analysis is conducted using the pressure-based coupled solver, while LES is performed using the segregated PIMPLE algorithm. The main difference between the coupled and segregated algorithm is the continuity equation. The coupled algorithm solves the pressure-based continuity and momentum equations together. Instead, the segregated algorithm solves the pressure correction and momentum equations separately.

The PIMPLE is the combination of the two well-known pressure-based segregated algorithms of SIMPLE [52] and PISO [53], and it is mainly used for transient simulations. First, a specified number of inner correction loops are solved, and a steady-state solution is expected for each time-steps. Next, transport equations are solved. These two steps are part of the PISO solution. However, the PISO part is solved repeatedly until the specified outer loop number is completed with new initial guesses, which is the SIMPLE part of the PIMPLE algorithm. The diagram of the PIMPLE algorithm is shown in Fig. 2.14.

On the other hand, the coupled algorithm combines the first and second steps of the PIMPLE algorithm and reduces them to a single step. The coupled algorithm is more robust than the segregated algorithm in steady-state CFD analysis [54]. However, it requires more computational time for a single RANS iteration. A diagram of the coupled algorithm is shown in Fig. 2.15.

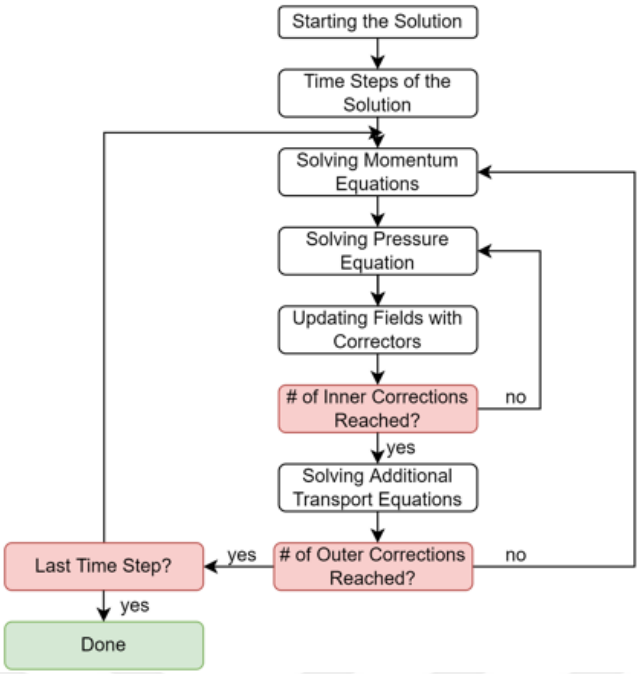


Figure 2.14: PIMPLE algorithm

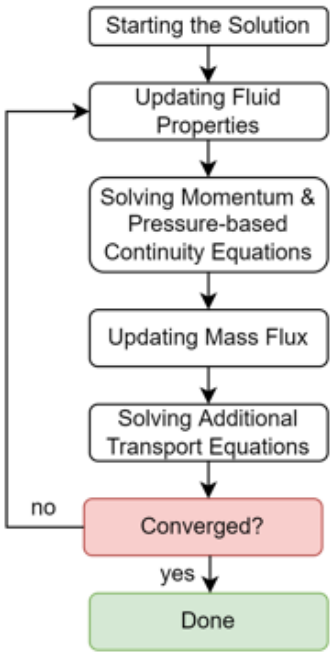


Figure 2.15: Coupled algorithm

2.4.3 Turbulence Modeling

Dealing with the turbulent flow is not as straightforward as dealing with laminar flows. Before discussing the mathematical modeling of the turbulent flow, the turbulence scales need to be discussed.

The general properties of the turbulent flows can be listed as [55]:

- Irregularity
- Diffusivity
- Occurs in large Reynolds numbers
- Three-dimensional
- Dissipation
- Continuum
- Property of fluid flows

The turbulent flows compose of different scales of eddies depending on the flow and geometry. Large-scale eddies show anisotropic nature and are affected by the geometry, initial, and boundary conditions. In contrast, small-scale eddies display isotropic characteristics and are insensitive to these conditions [55]. The energy is transported from large eddies to small eddies by the concept of energy cascade proposed by Richardson [56]. The formation of the large eddies produces the energy, and the energy passes onto smaller eddies. Finally, the energy dissipates in the smallest structures due to the viscosity. The energy cascade process is shown in Fig. 2.16 [57]. The largest scale of the eddies can not be bigger than the characteristic length of the flow field.

The size of the smallest scale can be computed using only mean energy dissipation rate (ϵ_d) and kinematic viscosity (ν) due to the turbulence becomes fully developed. These two variables can be represented in terms of dimension system as shown in Eqn 2.12 and 2.13. The length scale combines these two variables as shown in 2.14.

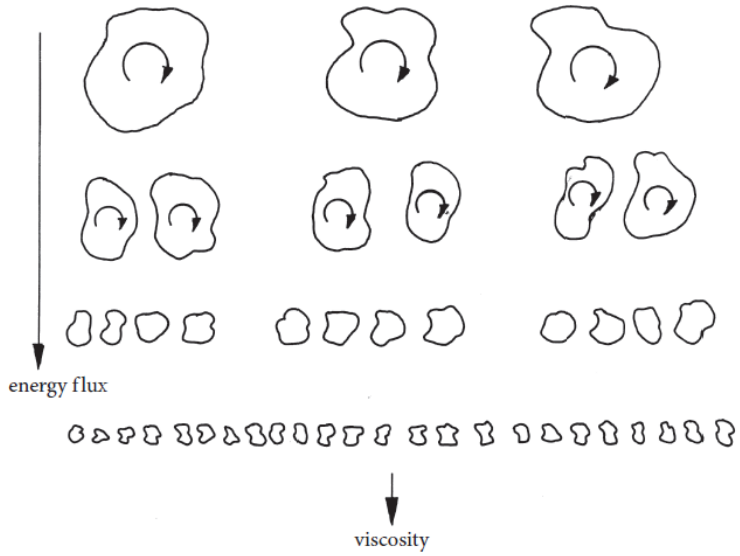


Figure 2.16: Energy cascade from large eddies to small eddies [57]

$$\epsilon_d = L^2 T^{-3} \tag{2.12}$$

$$\nu = L^2 T^{-1} \tag{2.13}$$

$$l_K = (\frac{\nu^3}{\epsilon_d})^{1/4} \tag{2.14}$$

This length scale is called as Kolmogorov length scale, which refers to the size of the smallest eddies. This length scale is also known as the dissipational length scale due to smaller scales being dissipated into heat due to viscosity, and they vanish. The smallest eddies rotate with a velocity of U_K and dissipate in a time of τ_K as shown below. Finally, the Kolmogorov energy spectrum is shown in Fig. 2.17. In this figure, k is the wave number and equals to $2\pi\lambda_e D_e$ where λ_e is the wavelength and D_e is the length of the eddies.

$$U_K = (\nu\epsilon_d)^{1/4} \tag{2.15}$$

$$\tau_K = (\frac{\nu}{\epsilon_d})^{1/2} \tag{2.16}$$

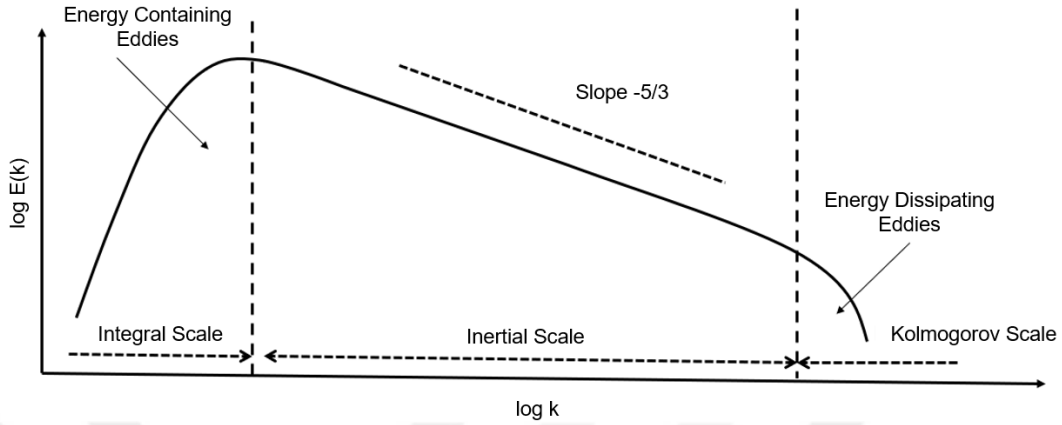


Figure 2.17: Turbulent energy spectrum

Different approaches have been developed to deal with the scales of turbulence. The first one is the Direct Numerical Simulation (DNS). In DNS, all turbulence scales are resolved; thus, DNS requires huge computational power. DNS does not require any modeling and solves the Navier-Stokes equations directly. In the inertial range of the energy spectrum, eddies show isotropic characteristics. In the LES method, relatively smaller eddies that show deterministic properties in the inertial range can be modeled in sub-grid scale models, and larger eddies than the sub-grid scale are directly solved. In LES, computational cell size must be reduced as the Reynolds number increases to obtain enough resolution. Finally, in Reynolds-Averaged Navier Stokes models, all scales of turbulence are modeled instead of solving them. The representation of all these models are shown in Fig. 2.18 [58]. In this figure, k_C is called a cut-off wave number, a function of the grid size. If the grid size is getting smaller, LES resolves more turbulent energy.

Turbulent flows show inherently time-varying properties, and these instantaneous components can be decomposed into mean and fluctuating parts, called Reynolds Decomposition [59]. As shown in Eqn. 2.17, the mean velocity can be obtained by averaging the instantaneous velocity in time. The fluctuating velocity components can also be obtained as shown in Eqn. 2.18. Schematics of the instantaneous, mean, and fluctuating velocity components are shown in Fig. 2.19 [60].

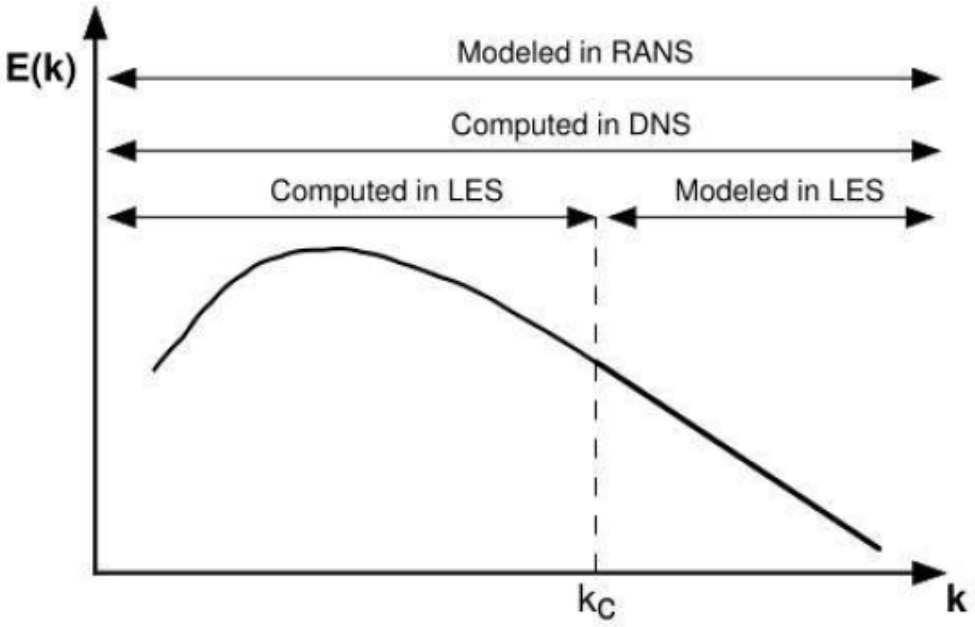


Figure 2.18: Resolved and modeled scales of the turbulence for RANS, LES and DNS [58]

$$\overline{U_i}(t_i) = \frac{1}{T_{period}} \int_{t_1 - T_{period}/2}^{t_1 + T_{period}/2} U_i(t) dt \tag{2.17}$$

$$U_i = \overline{U_i} + u_i \tag{2.18}$$

When the Reynolds decomposition is applied and the time-averaged and fluctuating terms are introduced to the standard Navier-Stokes equations, Reynolds-Averaged Navier Stokes (RANS) equations are obtained.

$$\frac{\partial \rho}{\partial t} + \frac{\partial (\rho U_i)}{\partial x_i} = 0 \tag{2.19}$$

$$\frac{\partial (\rho U_i)}{\partial t} + \frac{\partial (\rho U_i U_j)}{\partial x_j} = -\frac{\partial p}{\partial x_i} + \frac{\partial (\tau_{ij} - \rho \overline{u_i u_j})}{\partial x_j} \tag{2.20}$$

The major problem of the RANS equations is the closure problem. Additional terms, including the fluctuating terms, are required to solve the equations. The first term is

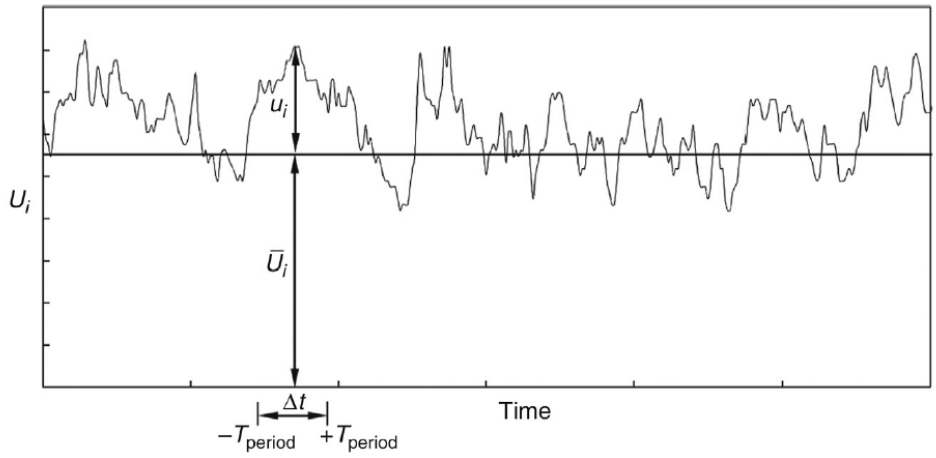


Figure 2.19: Schematic of the instantaneous, time-averaged and fluctuating velocity components [60]

the Reynolds stress tensor ($\overline{\rho u_i u_j}$). Reynolds stress tensor has nine components, but due to the symmetric nature of the tensor, the number of components can be reduced to six unknowns. Two approaches that are used for the calculation of this tensor are called eddy viscosity-based and Reynolds-stress models. In the first approach, all six variables of the Reynolds stress tensor are assumed to be equal under the assumption of the Boussinesq [61]. In the latter model, all of the components of the Reynolds stress tensor are calculated with separate equations. This approach often has convergence problems, but this problem can be overcome by using algebraic Reynolds-stress models neglecting diffusive and convective fluxes [62], [63]. In the present study, an eddy viscosity-based turbulence model is used; thus, only eddy viscosity modeling is presented.

Eqn. 2.25 describes the Reynolds stress tensor of eddy viscosity concept for incompressible Newtonian fluid flows where μ_t is the turbulent viscosity.

$$\overline{\rho u_i u_j} = \mu_t \left(\frac{\partial U_i}{\partial x_j} + \frac{\partial U_j}{\partial x_i}\right) \tag{2.21}$$

2.4.3.1 Reynolds-Averaged Navier Stokes Simulations

The problem of turbulence modeling comes out dealing with the turbulent viscosity. Several closure models have been developed for more than fifty years, and one of the most famous ones is the k-ϵ based turbulence models, which are proven their capabilities in dealing with the swirling flows [64], [65]. This study uses the Realizable k-ϵ turbulence model in RANS simulations.

Before discussing the Realizable k-ϵ model, standard k-ϵ of Jones and Launder [66] is needed to be discussed. In the standard k-ϵ model, the turbulent viscosity can be modeled as in Eqn. 2.22.

$$\mu_t = \rho C_\mu \frac{k^2}{\epsilon} \tag{2.22}$$

In this equation, C_μ is the experimental coefficient and can be changed depending on the problem. Also, k is the turbulent kinetic energy, and ϵ is the turbulence dissipation rate. These variables can be obtained by solving the transport equations shown below.

$$\frac{\partial(\rho k)}{\partial t} + \frac{\partial}{\partial x_j}\left(\rho \bar{U}_i k\right) = \frac{\partial}{\partial x_j}\left(\left(\mu + \frac{\mu_t}{\sigma_k}\right)\frac{\partial k}{\partial x_j}\right) + P - \rho\epsilon \tag{2.23}$$

$$\frac{\partial(\rho \varepsilon)}{\partial t} + \frac{\partial}{\partial x_j}\left(\rho \bar{U}_i \epsilon\right) = \frac{\partial}{\partial x_j}\left(\left(\mu + \frac{\mu_t}{\sigma_\varepsilon}\right)\frac{\partial \epsilon}{\partial x_j}\right) + C_{\epsilon 1}\frac{\epsilon}{k}P - C_{\varepsilon 2}\rho\frac{\epsilon^2}{k} \tag{2.24}$$

σ_k, σ_ϵ, $C_{\epsilon 1}$ and $C_{\epsilon 2}$ represent the experimental coefficients of the model in these equations. P is also the turbulence production rate, which can be obtained as shown below.

$$P = \mu_t\left(\frac{\partial \bar{U}_i}{\partial x_j} + \frac{\partial \bar{U}_j}{\partial x_i}\right)\frac{\partial \bar{U}_i}{\partial x_j} \tag{2.25}$$

Finally, the numerical values of the experimental coefficients are shown below.

Standard k-ϵ model has deficits when dealing with the swirling flows and separated flow regions, so the Realizable k-ϵ model was developed by Shih et al. [67]. The difference between the Realizable and Standard k-ϵ models is the definition of the

Table 2.6: Experimental coefficients of the Standard k-ϵ model

Parameter	σ_k	σ_ϵ	C_μ	$C_{\epsilon 1}$	$C_{\epsilon 2}$
Value	1.0	1.3	0.09	1.44	1.92

C_μ and $C_{\epsilon 1}$ terms which are calculated using strain rate and vorticity tensors. The calculation of these terms is shown below.

$$C_\mu = \left(A_0 + A_s V^* \frac{k}{\epsilon} \right)^{-1} \tag{2.26}$$

$$A_s = \sqrt{6} \cos \left(\frac{1}{3} \cos^{-1} \left(\sqrt{6} \frac{S_{ij} S_{jk} S_{ki}}{|S_{ij}|^3} \right) \right) \tag{2.27}$$

$$V^* = (S_{ij} S_{ij} + W_{ij} W_{ij})^{0.5} \tag{2.28}$$

$$S_{ij} = \frac{1}{2} \left(\frac{\partial \bar{U}_i}{\partial x_j} + \frac{\partial \bar{U}_j}{\partial x_i} \right) \tag{2.29}$$

$$W_{ij} = \frac{1}{2} \left(\frac{\partial \bar{U}_i}{\partial x_j} - \frac{\partial \bar{U}_j}{\partial x_i} \right) \tag{2.30}$$

$$C_{\epsilon 1} = max \left(0.43, \frac{\eta_\epsilon}{5 + \eta_\epsilon} \right) \tag{2.31}$$

$$\eta_\epsilon = \frac{|S_{ij}| \, k}{\epsilon} \tag{2.32}$$

In these set of equations, A_0 represents the experimental constants while A_s, V^* and η_ϵ model parameters; S_{ij} is the strain rate tensor and W_{ij} is the vorticity tensor. The numerical values of the Realizable k-ϵ coefficients are shown in below.

This study uses Realizable k-ϵ with the enhanced wall treatment option. The enhanced wall treatment is also called a two-layer approach due to dividing the flow

Table 2.7: Experimental coefficients of the Realizable k-ϵ model

Parameter	σ_k	σ_ϵ	A_0	$C_{\epsilon 2}$
Value	1.0	1.2	4.0	1.9

field into viscosity-affected and fully turbulent regions. In the viscosity affected region, turbulent dissipation rate and turbulent viscosity are modeled differently than the transport equations of the Realizable k-ϵ model. The turbulent Reynolds number is used for splitting these regions, as shown in Eqn. 2.33 where the y is the wall-normal distance from the wall boundaries.

$$Re_y = \frac{\rho y \sqrt{k}}{\mu} \tag{2.33}$$

The critical turbulent Reynolds number is 200 for splitting the regions, and if the turbulent Reynolds number is below 200, the region is called the viscosity-affected region. In this region, an additional one-equation turbulence model is solved [68]. The turbulent viscosity is calculated as shown below. In this equation, ℓ_μ defines the length scale, which is computed as shown in Eqn. 2.35 [69].

$$\mu_{t,\text{2layer}} = \rho C_\mu \ell_\mu \sqrt{k} \tag{2.34}$$

$$\ell_\mu = y C_\ell^* \left(1 - e^{-\text{Re}_y / A_\mu}\right) \tag{2.35}$$

The transition of the turbulent viscosity can be problematic between two layers. Thus, a blending function of turbulent viscosity is applied, as shown in Eqn. 2.36 [70]. In this equation, λ_ϵ is the blending coefficient and can be obtained as shown in Eqn. 2.37.

$$\mu_{t,\text{enh}} = \lambda_\epsilon \mu_t + (1 - \lambda_\epsilon) \mu_{t,\text{2layer}} \tag{2.36}$$

$$\lambda_\epsilon = \frac{1}{2}\left[1 + \tanh\left(\frac{\mathrm{Re}_y - \mathrm{Re}_y^*}{A}\right)\right] \tag{2.37}$$

In Eqn. 2.37, A is the coefficient that determines the width of the blending coefficient. This coefficient keeps the blending coefficient in a range of one percent of its free-stream value depending on the change in the turbulence Reynolds number, as shown below.

$$A = \frac{|\Delta \mathrm{Re}_y|}{\mathrm{atanh}(0.98)} \tag{2.38}$$

Finally, the turbulent dissipation rate is obtained in the viscosity-affected region, as shown in Eqn. 2.39 where the ℓ_ϵ is the length scale which is calculated as shown in Eqn. 2.40. In the length scale equation, $C_\ell{}^*$ is the length scale coefficient to provide a smooth transition between the layers and computed as shown in Eqn. 2.41 [69].

$$\epsilon = \frac{k^{3/2}}{\ell_\epsilon} \tag{2.39}$$

$$\ell_\epsilon = yC_\ell{}^*\left(1 - e^{-\mathrm{Re}_y/A_\epsilon}\right) \tag{2.40}$$

$$C_\ell{}^* = \kappa C_\mu^{-3/4}, \quad A_\mu = 70, \quad A_\epsilon = 2C_\ell{}^* \tag{2.41}$$

2.4.3.2 Large Eddy Simulations

Swirling flows are inherently highly chaotic and three-dimensional flows. Eddy viscosity-based RANS models could not be capable of predicting the flow field well due to its nature. Thus, LES has been widely used to predict chaotic flow fields for over thirty years.

Unlike the RANS modeling, a spatial filter is applied to splitting the resolved and modeled turbulence scales, called LES decomposition or filtering decomposition. As a result, filtered Navier-Stokes equations are obtained and solved in LES. Like RANS,

filtering decomposition is applied to instantaneous variables, as shown below. In this equation, $\overline{u}$ is called as resolved scales while $u^{'}$ represents the sub-grid scales.

$$u = \widetilde{u} + u^{'} \tag{2.42}$$

The main difference between the LES decomposition and Reynolds decomposition is spatial-averaging is conducted in LES instead of time-averaging. Thus, the filtering decomposition has different averaging rules. For example, the filtered sub-grid scales are not equal to zero due to filtering is not time-averaging. The resolved and modeled scales are splitted using the filter function $G(r, x)$ as shown in Eqn. 2.43 [71].

$$\widetilde{u} \equiv \int_{-\infty}^{\infty} G(r)u(x-r)dr \tag{2.43}$$

The filtered conservation of mass equation is shown below.

$$\frac{\partial \rho}{\partial t} + \frac{\partial}{\partial x_j}\left(\rho \widetilde{u}_i\right) = 0 \tag{2.44}$$

The filtered conservation of momentum equation is shown below. In this equation, sub-grid scale stress tensor $(\widetilde{u_j u_i} - \widetilde{u}_i \widetilde{u}_j)$ are needed to a sub-grid scale model to make the equation solvable. This sub-grid scale stress tensor can be obtained through an approach that is similar to Boussinesq approximation in RANS modeling[61] as shown in Eqn. 2.46. This approximation, also called as Smagorinsky model [72], is the simplest closure model for the sub-grid scales. In this equation, μ_{SGS} is the turbulent viscosity of the sub-grid scale that can be computed as shown in Eqn. 2.47. C_S is the model coefficient and equals to 0.2, Δ is the grid size and the $\overline{S}_{ij}$ represents the resolved shear stress components. The other term k_{SGS} is the sub-grid scale turbulent kinetic energy.

$$\frac{\partial \left(\rho \widetilde{u}_i\right)}{\partial t} + \frac{\partial}{\partial x_j}\left(\rho \widetilde{u}_i \widetilde{u}_j\right) = -\frac{\partial \widetilde{p}}{\partial x_i} + \frac{\partial}{\partial x_j}\left(\widetilde{\tau}_{ij} - \rho(\widetilde{u_j u_i} - \widetilde{u}_i \widetilde{u}_j)\right) \tag{2.45}$$

$$\rho(\widetilde{u_j u_i} - \widetilde{u}_i \widetilde{u}_j) = -2\mu_{SGS}\widetilde{S}_{ij} + \frac{2}{3}\rho k_{SGS}\delta_{ij} \tag{2.46}$$

$$\mu_{SGS} = \rho(C_S\Delta)^2(2\widetilde{S}_{ij}\widetilde{S}_{ij})^{0.5} \tag{2.47}$$

One crucial deficit of the Smagorinksy model is too dissipative around the walls [58]. Several models have been developed to overcome the deficit of the Smagorinsky model. One is the Wall-Adapting Local Eddy Viscosity (WALE) model by Nicoud and Ducos [73]. In this study, WALE is used as the sub-grid scale model. The model was developed based on the square of the velocity gradient tensor, which includes the local shear stress and rotation tensor. Thus, all turbulence structures related to turbulent kinetic energy dissipation could be determined. In addition, WALE makes turbulent viscosity zero around the walls without any damping functions. The turbulent viscosity is defined as shown in Eqn. 2.48. In this equation, Δ defines the length scale S_{ij}^d is the symmetric part of the velocity gradient tensor and $\widetilde{S_{ij}}$ is the resolved shear stress components. Δ computed as Eqn. 2.49) where κ is the von Karman constant, C_w is the experimental constant, V is the volume of the cell, d is the distance between the first cell and the wall. S_{ij}^d computed as shown in Eqn. 2.50 where $\widetilde{g_{ij}}$ is the sub-grid scale velocity gradient tensor. The value of the C_w constant was defined in the original model as 0.5 [73] but it is used as 0.325 in OpenFOAM [74].

$$\mu_t = \rho\Delta^2\frac{(S_{ij}^d S_{ij}^d)^{\frac{3}{2}}}{(\widetilde{S_{ij}}\widetilde{S_{ij}})^{\frac{5}{2}} + (S_{ij}^d S_{ij}^d)^{\frac{5}{4}}} \tag{2.48}$$

$$\Delta = min(\kappa d, C_w V^{1/3}) \tag{2.49}$$

$$S_{ij}^d = \frac{1}{2}(\widetilde{g_{ij}}^2 + \widetilde{g_{ji}}^2) - \frac{1}{3}\delta_{ij}\widetilde{g_{kk}}^2 \tag{2.50}$$

Typically, $\%80$ of the turbulent energy spectrum is expected to be resolved in LES [75]. Several methods have been offered to check the resolution of the LES, and one of them is the LES Index Quality (LESIQ) offered by Celik et al. [76]. A higher level of the LESIQ means better LES resolution, and this value must be higher than 0.8. The LESIQ is calculated as below, where the ν is the kinematic viscosity and ν_t is the turbulent viscosity.

$$LESIQ = \frac{1}{1 + 0.05\left[\frac{(\nu+\nu_t)}{\nu}\right]^{0.53}} \tag{2.51}$$

2.4.3.3 Numerical Validation

This chapter presents a numerical analysis of the Cambridge/Sandia Swirl Burner [77]. The first purpose of the study is to validate the RANS and LES models in a relatively more uncomplicated geometry before validating the radial-radial type swirlers. Especially, finding the proper numerical schemes is significant for correct LES analysis.

The schematic of the Cambridge-Sandia stratified swirl burner and flow directions are shown in Fig. 2.20 [77], [78]. The experiments were conducted in isothermal conditions. The burner includes two concentric fuel inlets and is embedded in a circular wind tunnel whose outer diameter equals 382 mm. The burner was also designed to investigate the effect of swirling flow so that the outer jet can provide swirling flow with different swirl numbers while the inner fuel jet only streams non-swirling flow. Here the swirl number is defined as the ratio of the tangential velocity to axial velocity. Two different swirling flows, the moderate and highest swirling flows having swirl numbers of 0.45 and 0.79, respectively, are studied experimentally. Only the highest swirling flow case with a swirl number of 0.79 is considered in this study. Mean velocity values of the U_i, U_o and U_e are 8.31 m/s, 18.7 m/s and 0.4 m/s, respectively. More details and measurement results can be found in Sweeney et al. [77], [78] and Zhou et al. [79].

The computational domain spans 300 mm and 200 mm in axial (U) and radial directions (V), respectively. Also, the domain prevents the non-physical numerical phenomena due to boundary conditions. The inlet sections are located 10 mm upstream of the jet exit. The domain is discretized by structured grids using Pointwise version 18.1 software, and the schematic of the domain is shown in Fig. 2.21. In this domain, the center of the swirling jet exit is defined as the origin location. A total number of 4.02 million multi-block structured grid points is used in the simulations, which satisfy the LES criteria as shown in Fig. 2.22 where the minimum value is higher than

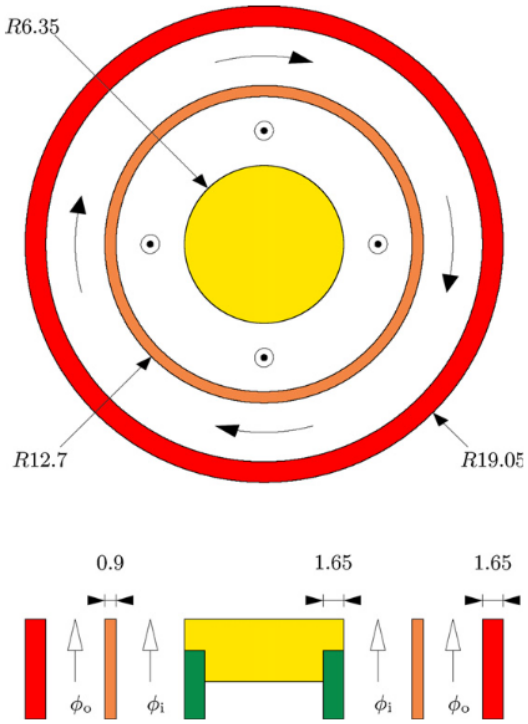


Figure 2.20: Schematic of the Cambridge/Sandia stratified swirl burner [77], [78]

0.8.

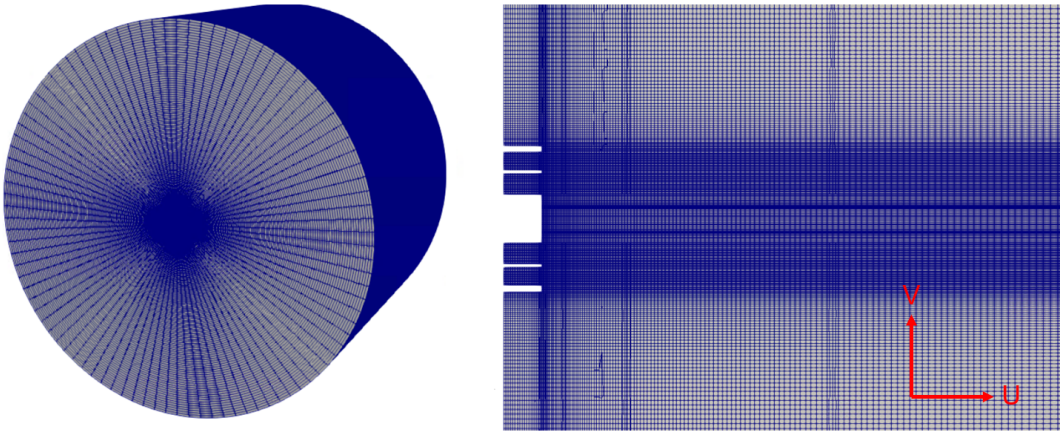


Figure 2.21: Computational domain for the Cambridge/Sandia validation case

A pressure based-coupled solver is used for the RANS simulations. The pressure term is discretized using the second-order central scheme and the other terms are discretized using the second-order upwind scheme. Realizable k-ϵ turbulence model

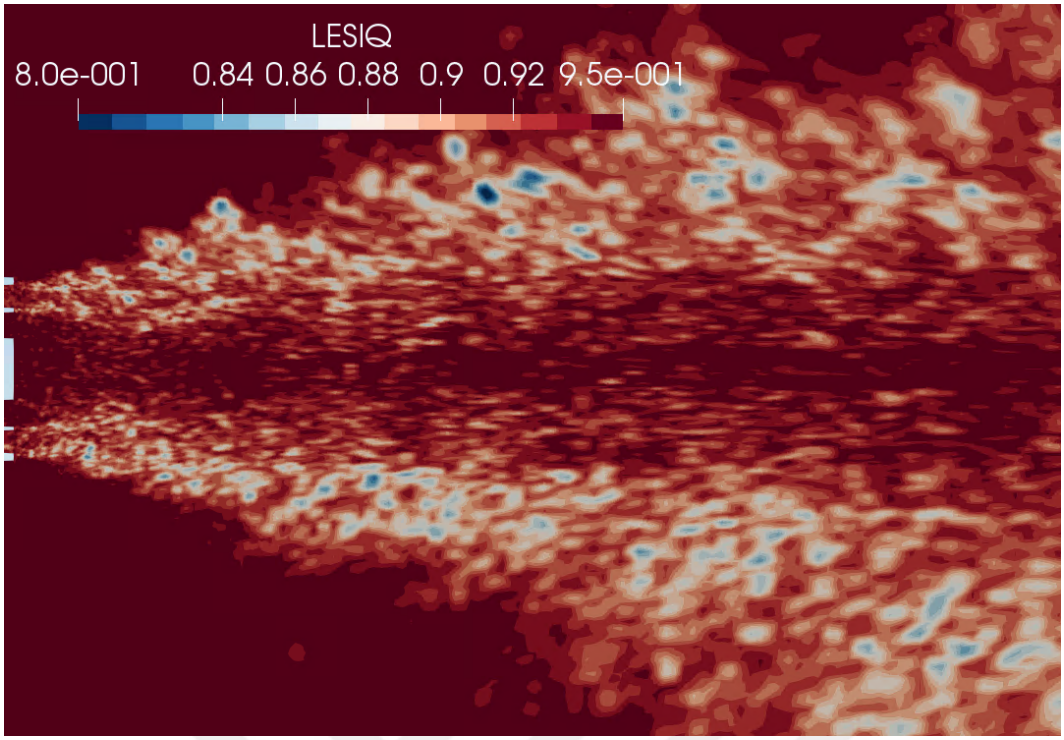


Figure 2.22: The evaluation of the LESIQ for the Cambridge/Sandia validation case

with enhanced wall treatment is used for numerical computation. Fully developed axial velocity profiles are applied inner and outer jets and tangential velocity of the outer jet adjusted to keep the exit velocity profile similar to the experiment.

In this study, pimpleFoam is used as an incompressible transient solver [80]. WALE [73] is used as the sub-grid scale in numerical simulations. The temporal discretization is carried out using a second-order backward differentiation scheme for the LES. The convective and gradient term discretizations are performed using a second-order central differencing scheme. The time step size is selected as 1e-5 s for the LES, which corresponds to a maximum CFL number of 1.5. Turbulent inlet boundary conditions have a crucial impact on the accuracy of the LES. The inlet boundary condition is obtained from different annular pipe flow simulations by following Turkeri et al. [81]. Separate LES are performed to generate turbulent inlet boundary conditions for both of the annular pipes. Periodic boundary conditions are applied at the inlet and outlet sections of the annular pipes and the no-slip boundary condition is used for walls. A mean velocity profile with random perturbations is applied as initial conditions then the simulation is conducted until the velocity profile converges to a

statistically stationary state. After that, the instantaneous velocity data is stored in a file to be used in the main simulation. Here, a scaling procedure on the interpolated velocities is conducted to satisfy a consistency between the numerical and experimental data at the closest measurement location. In the main simulation, the inner and the outer annulus pipe walls at the upstream part of the domain are defined as the slip-wall boundary to preserve obtained velocity profiles. The slip boundary condition is applied at far radial distance of the domain, and the non-reflective type boundary condition is used for the outlet of the domain to prevent any non-physical reversed flow. The first grid point is located to keep y^+ values below one around the bluff body and any wall functions or wall-treatments are not applied for all simulations. The simulation is initiated with a flow at rest and retained for four flow-through times to reach the statistically stationary state, which is defined as the time in which the swirling flow reaches three hydraulic diameters of the outer annulus after the jet exit. The simulations are conducted for four flow-through times to collect the statistical data and obtain the time-averaged data.

Isothermal axial velocity contours of the LES and RANS is shown in Fig. 2.23. Both simulations provide similar results to each other. First, two low-velocity regions are observed in both LES and RANS simulations. One of them is the recirculation zone around the bluff body. The recirculation zone length is calculated as 19 mm and 16 mm in LES and RANS, respectively.

The velocity components are compared in Fig. 2.24. The velocity profiles of U, V and W represent axial, radial and tangential velocity components, respectively. The locations where the data is compared means the axial distance after the bluff body. At 2 mm, the flow pattern of the LES is more consistent with the experimental data than the RANS results due to inlet velocity profiles which are generated for LES based on the experimental data. However, RANS results are still in reasonable agreement with experimental data. The maximum tangential and axial velocity magnitude are slightly under-predicted in the RANS simulations compared to the LES results.

LES is still in better agreement with experimental data at the following comparison location. Centerline axial velocity is predicted well by LES. RANS is also consistent with experimental data at the centerline; however, the axial velocity is slightly under-

predicted, resulting from the under-predicted axial and the tangential velocity profiles at 2 mm. Also, a better agreement is observed in LES for the peak axial velocity

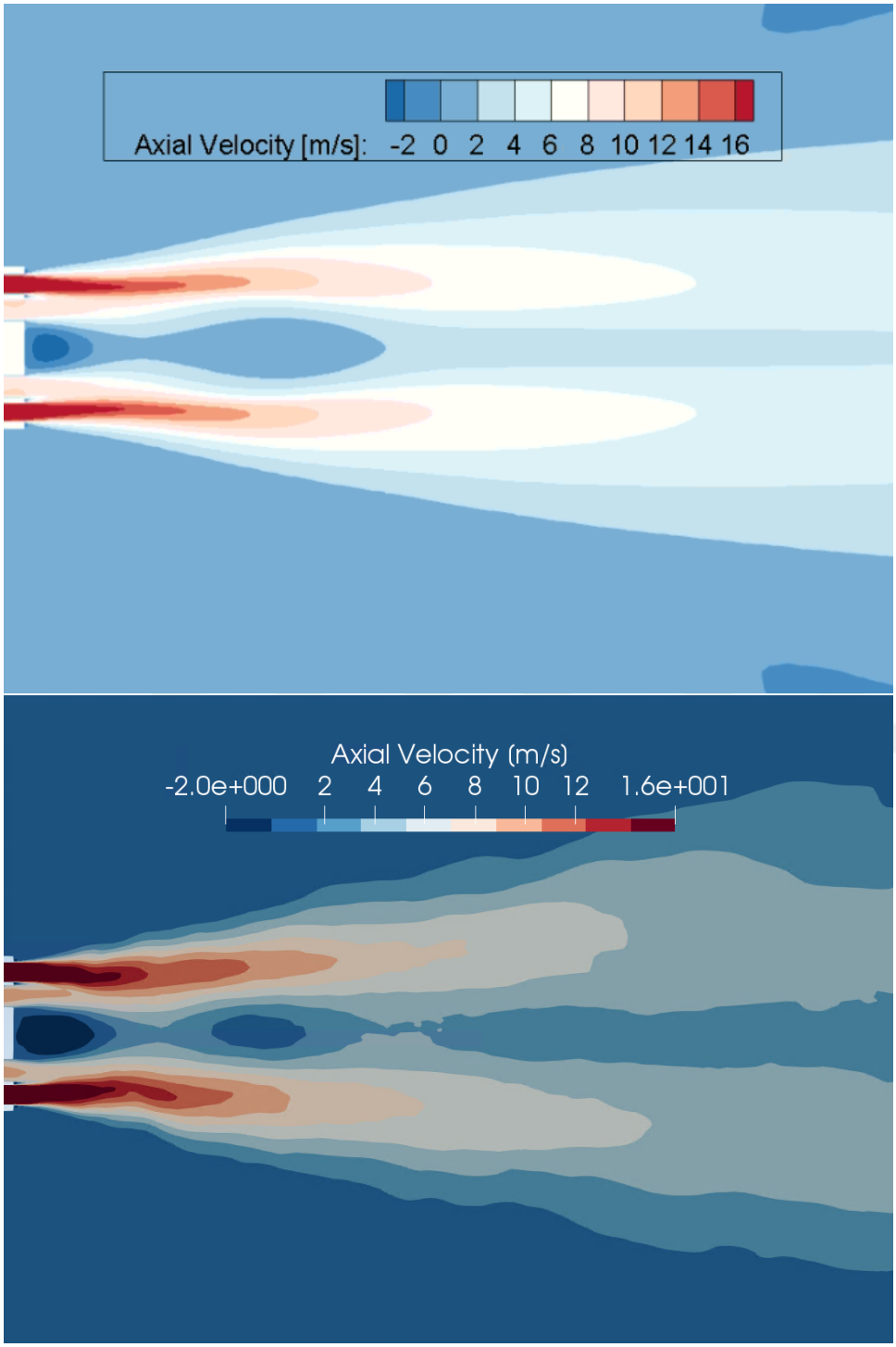


Figure 2.23: Axial velocity contours of RANS (upper) vs LES (lower) in isothermal condition

profile at this location. Again, RANS provides a lower tangential velocity than the experiment, while LES is closer to the experimental tangential profile. The radial velocity profiles are similar in both simulations.

At the streamwise position of 30 mm, the axial velocity is underpredicted at the centerline axis of the burner in both simulations. However, a more remarkable difference is observed in the RANS simulation due to the miscalculation of the axial pressure gradient. The difference in radial velocity profiles is getting larger for both simulations. The tangential velocity profiles of both simulations are in good agreement with the experimental tangential velocity profile.

Finally, the velocity profiles are compared at 50 mm. More consistent axial velocity profiles compared to experimental data are obtained by LES. Centerline velocity is under-predicted in RANS; however, LES is in good agreement with the experiment. Also, both simulations predict the tangential velocity profiles well. However, both simulations can not follow the radial profile trend and fail to provide similar results to experimental data.

The r.m.s. profiles of the velocity components of the LES are presented by comparing the experimental data in Fig. 2.25. The r.m.s. profiles align with the experiment, which is essential for the aspects of turbulent flow.

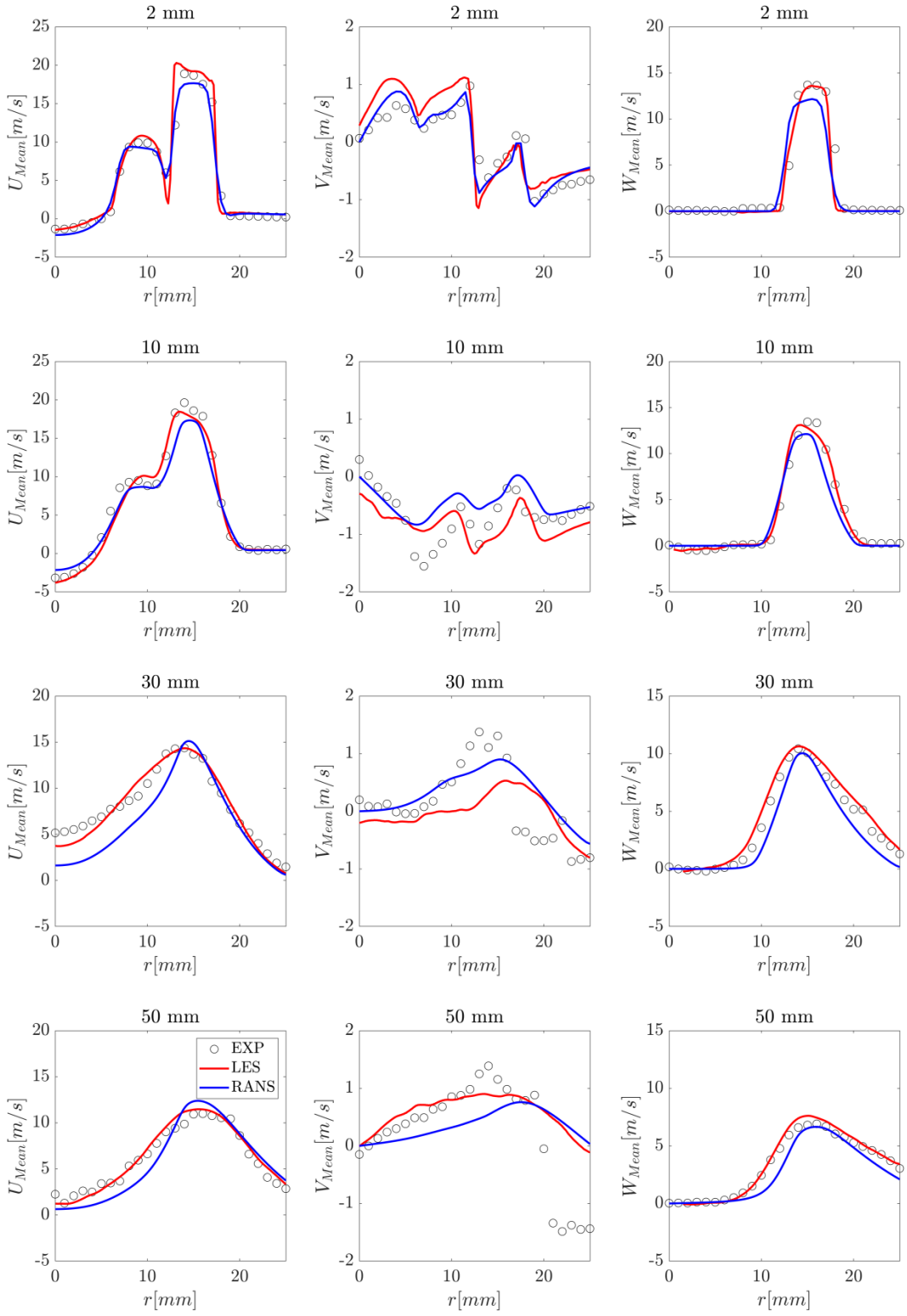


Figure 2.24: Time-averaged velocity profile comparison at different locations in isothermal condition

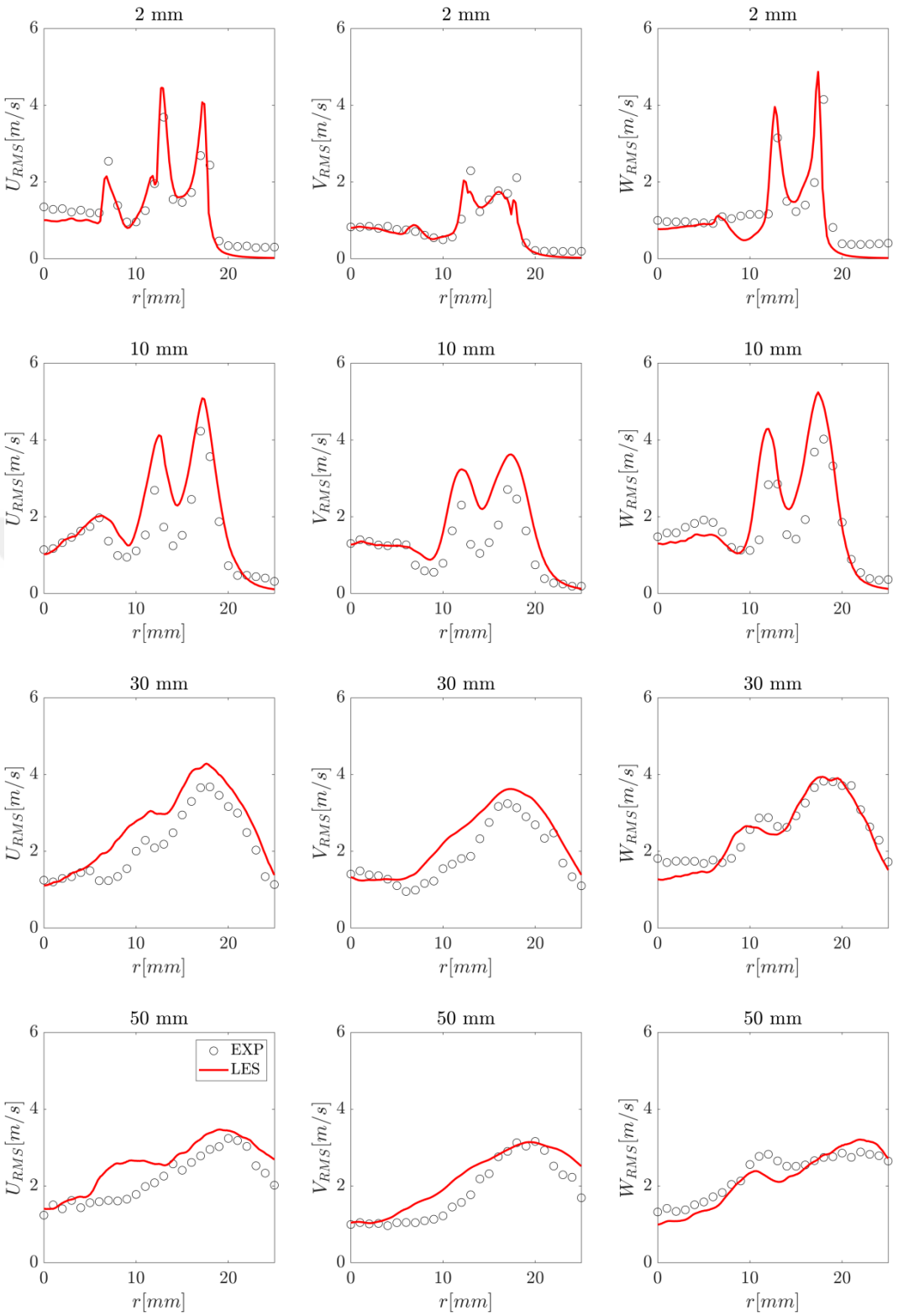


Figure 2.25: The r.m.s. velocity profile comparison at different locations in isothermal condition

2.4.4 Numerical Setups

To investigate the effect of the confinement and channel orientation on the parameters which cannot be obtained from the PIV measurements (such as the tangential velocity component and the SN), CFD simulations are performed. RANS simulations with an eddy viscosity-based turbulence model offered consistent results with experimental data of multi-stage swirlers under confined conditions, motivating the present study to use the same methodology [64], [65]. Thus, the realizable k-ϵ turbulence model with the enhanced wall treatment option is used with coupled solver in ANSYS Fluent framework V19.R1. The pressure is discretized using a central scheme and the rest is discretized using the second-order upwind numerical scheme. Simulations are performed by setting the velocity inlet (measured velocity and turbulence profiles), the pressure outlet (zero gradient pressure and turbulence) and no-slip wall boundary conditions for the inlet, outlet and wall surfaces, respectively. The CFD domain is extended with an atmospheric plenum to prevent non-physical reversed flows. The convergence of each analysis is monitored by collecting the velocity data at different probe locations. A mesh independence study is carried out with three different polyhedral meshes, which have 2.5×10^6 (coarse), 5.3×10^6 (medium), and 9.8×10^6 (fine) grid points to minimize the influence of the mesh resolution on the numerical results. For this purpose, the recirculating mass flow rate, the pressure drop, and the SN at several planes are recorded, and the results are shown in Table 2.8. Also, the normalized axial velocity profiles are compared for each meshes and results are shown in Fig. 2.26. The medium-mesh size is selected for further simulations since it provides similar results to the fine mesh at a reduced computational cost. These grid point numbers are given for medium confinement cases and the number of the mesh elements can increase or decrease depending on the confinement level. The first grid point height distribution satisfies to keep y+ values below five around the walls. The CFD domain and grid point distributions are shown in Fig. 2.29.

The results of the RANS and LES simulations are compared to experimental data for the unconfined configuration of the CR swirler. A computational domain that spans 300 mm and 200 mm in axial and radial directions is created. Due to the complicated structure of the radial-radial swirlers, a polyhex-core grid structure is preferred in this

Table 2.8: Comparison of flow parameters for different meshes considered in the mesh independence study

Mesh	Pressure Drop [%]	Normalized $\dot{m}_{reversed}$	SN at y/D$_h$ = 1
Coarse	1.823	0.982	-0.337
Medium	1.926	1.0	-0.350
Fine	1.923	0.997	-0.346

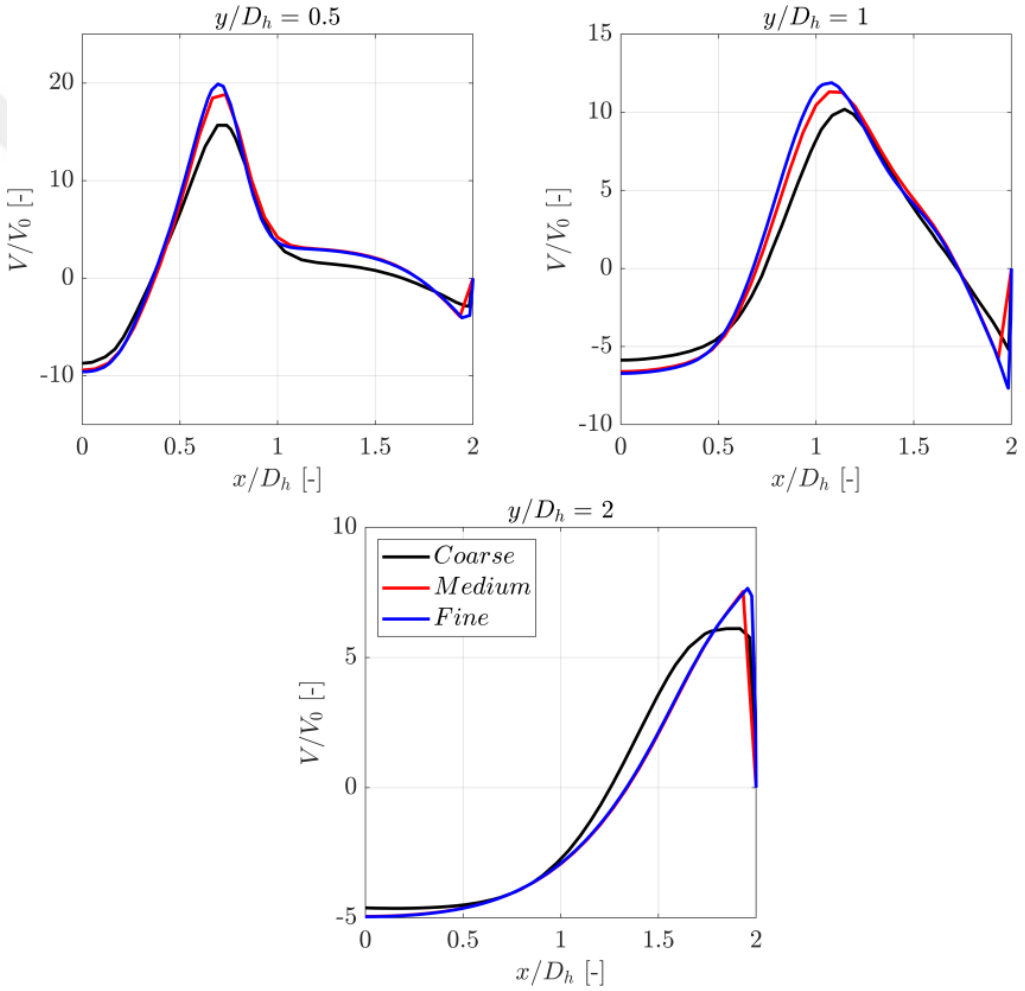


Figure 2.26: Comparison of the time-averaged axial velocity (the velocity component in the y-direction, V/V_0), obtained from numerical simulations for the coarse, medium and fine mesh configurations in the $y/D_h = 0.5$, 1 and 2

study. The logic behind the polyhex-core grid is generating polyhedral meshes around the wall and hexahedral meshes away from the wall. Hexahedral mesh is the closest mesh structure to the structural grid that is used in the Cambridge/Sandia validation case. Thus, using the same numerical schemes with the validation case, the polyhex-core grid structure is preferred. The polyhex-core grid is generated in the ANSYS Fluent v19R1. A total number of 9.2 million cell points are generated and grid point distribution and LESIQ results are shown in Fig. 2.29 and Fig. 2.29, respectively.

The pimpleFoam is employed as an incompressible transient solver for LES. WALE [73] is used as the sub-grid scale in numerical simulations. The temporal discretization is carried out using a second-order backward differentiation scheme for the LES. The convective and gradient term discretizations are performed using a second-order central differencing scheme. The time step size is selected as 1e-6 seconds for the LES, corresponding to a maximum CFL number of 1.4. The simulation is initiated with a flow at rest and retained for 600 milliseconds for the statistically stationary state. Then, the simulation is continued for additional 600 milliseconds to collect the statistical data. Any turbulence generation mechanism is not used for the inlet due to swirler generates a high level of turbulence [82].

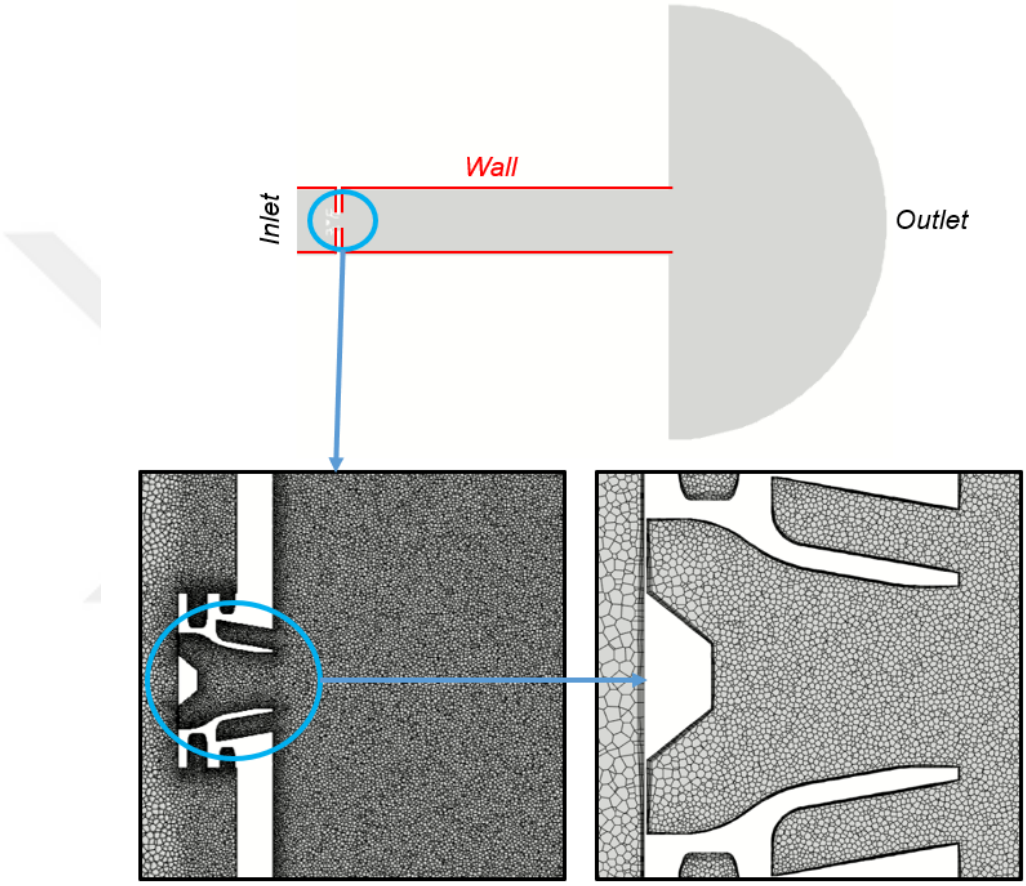


Figure 2.27: Computational domain with boundary conditions (top) and the computational mesh with a close-up view (bottom) for RANS

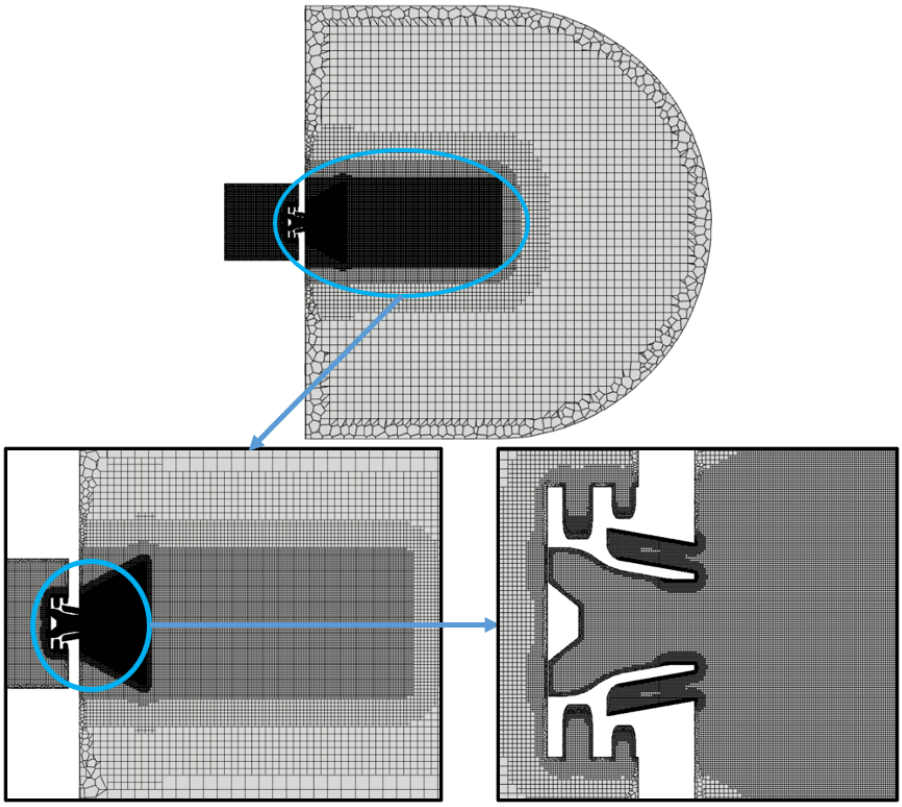


Figure 2.28: Computational domain (top) and the computational mesh with a close-up view (bottom) for LES

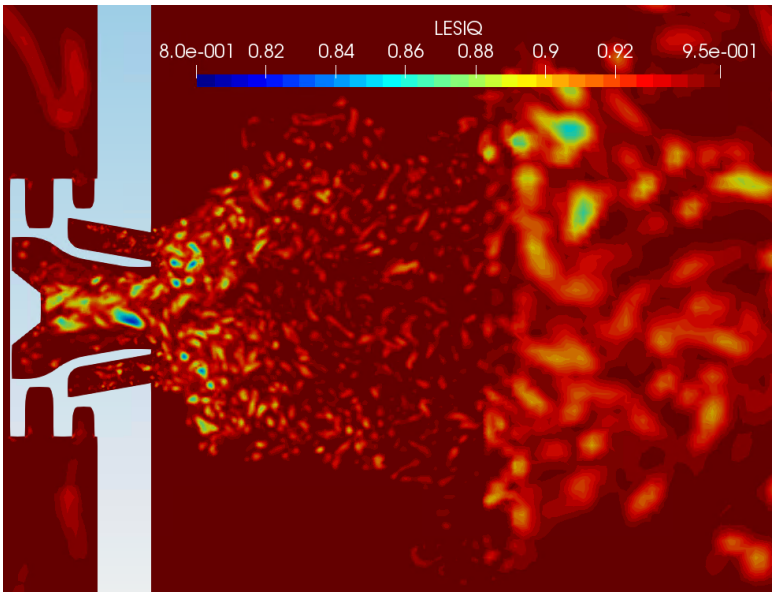


Figure 2.29: LESIQ evaluation for the unconfined configuration of the CR swirler

2.5 Modal Analysis

The proper orthogonal decomposition (POD) and the spectral proper orthogonal decomposition (S-POD) methods are used in this study to extract the coherent structures. The POD and the S-POD methods are applied to the fast PIV data of the medium confinement case for the CO and CR swirlers to observe the differences between the two methods in the sense of the orientation section. Also, the POD method is applied to the slow PIV data to obtain the overall structure of the modes in a relatively large area while the S-POD method is applied to the fast PIV data to extract frequency information.

2.5.1 Proper Orthogonal Decomposition

The POD is a model decomposition method to extract the coherent structures of the turbulent flow according to their energy contents. The POD naturally deals with the fluctuating part of the Reynolds decomposition, as shown in Eqn. (2.52).

$$V(x,t) = \overline{V}(x,t) + v'(x,t) \tag{2.52}$$

POD express the fluctuating velocity component as series of the number of snapshots, via

$$v'(x,t) = \sum_{i=1}^{N} \alpha_i(t) \cdot \Psi_i(x) \tag{2.53}$$

where *x* indicates the space vector and *t* the time. The decomposition of the fluctuating velocity component includes the temporal coefficients α and Ψ spatial modes. In this study, the snapshot-POD approach of Sirovich [83] is applied to low-speed PIV data to obtain modes in a larger area and fast-PIV data to compare the snapshot-POD mode shapes to S-POD mode shapes. The correlation matrix, $C_{\mathrm{i,j}}$, is constructed as shown in Eqn. (2.54) and the energies of the spatial modes, λ and temporal coefficients are obtained by solving the eigenvalue problem shown in Eqn. (2.55). Finally, the spatial modes are calculated by projecting the snapshots onto the temporal coefficients, as shown in Eqn. (2.56).

$$C_{i,j} = \frac{1}{N} v'(x,t_i)^T v'(x,t_i); C_{i,j}\ is\ of\ size\ NxN \tag{2.54}$$

$$C\alpha_i = \lambda_i \alpha_i \; where \; \lambda_1 > \lambda_2 > \lambda_3 > ... > \lambda_N \tag{2.55}$$

$$\Psi_i(x) = \frac{1}{N\lambda_i} \sum_{i=1}^{N} \alpha_i(t_j) v'(x, t_j) \tag{2.56}$$

2.5.2 Spectral Proper Orthogonal Decomposition

POD could be problematic, especially dealing with highly turbulent flows, to extracting mode shapes such as swirling flow in the combustors. The focus of the POD is to maximize the energy level of the related modes without any restrictions on the dynamics of these modes [44]. Thus, several physical modes may be combined in a single POD mode. To overcome this problem, the S-POD has been developed. In this paper, the S-POD of Sieber et al. [43] is followed. Even though the S-POD method resembles the snapshot POD method, a low pass filter, g_{k}, is applied to diagonals of the correlation matrix to modify it. Thus, new filtered correlation matrix $R_{\mathrm{i,j}}$ is obtained and represented as:

$$R_{i,j} = \sum_{k=-N_f}^{N_f} g_k R_{i+k,j+k} \tag{2.57}$$

The g_{k} represents the coefficients of the symmetric finite-impulse response filter with a length of $2N_{\mathrm{f}}$+1. This study uses a Gaussian-type low-pass filter with a standard deviation of the filter. S-POD shows the band-pass characteristics even if a low-pass filter is used [43]. The filter size is determined roughly by the ratio of the hydraulic diameter of the confinement test section to bulk velocity. Finally, temporal coefficients and mode energies are obtained from the eigenvalue problem, Eqn. 2.58, similarly to the POD method. Again, the eigenvectors are obtained from the snapshot projection onto temporal coefficients, as shown in Eqn. 2.59.

$$R\alpha_i = \lambda_i \alpha_i \; where \; \lambda_1 > \lambda_2 > \lambda_3 > ... > \lambda_N \tag{2.58}$$

$$\Phi_i(x) = \frac{1}{N\lambda_i} \sum_{i=1}^{N} \alpha_i(t_j) v'(x, t_j) \tag{2.59}$$

CHAPTER 3

RESULTS AND DISCUSSIONS

In this section, slow and fast experimental results are provided regarding the effect of the sense of the rotation and the confinement ratio. First CO and CR swirlers under the medium confinement ratio is compared. For this purpose, time-averaged velocity fields and vorticity contours are provided. Also, POD and S-POD contours are provided and their modes are compared.

3.1 Effect of the channel orientation

In this section, the flow fields of the CO and the CR radial-radial swirler configurations are compared in terms of time-averaged quantities and coherent flow structures. For the latter, the POD and the S-POD techniques introduced by Sieber et al. [43] are applied to obtain dominant mode structures and their frequencies. In all of the plots included in this section, the center of the jet exit corresponds to $x/D_h = 0$, whereas the confinement wall is at $x/D_h = 2$.

3.1.1 Time-averaged flow fields

Time-averaged normalized velocity fields for the CR and CO swirlers are compared in Fig. 3.1. The same plots are also produced from the results of the numerical simulations and presented in Fig. 3.2. Experimental and numerical results display a good agreement in terms of general flow topology. The sense of rotation influences the mean swirling flow fields several particular aspects. First, a strong radial expansion is observed in the CO swirler, which leads to the attachment of the jet to the dome

and then to the confinement walls. The CR swirler, on the other hand, generates a jet flow with a smaller expansion angle ($35.62°$), which reaches the confinement walls at $y/D_h \approx 1.5$ and becomes a wall jet. Accordingly, a secondary recirculation zone, i.e., corner recirculation zone (CRZ), forms between the expanding jet and the confinement walls, and the center of the CTRZ is located at a more downstream position ($y/D_{\text{h}} \approx$ 2.1) in the CR swirler configuration. In both cases, a CTRZ exists, and it seems to penetrate into the swirler. The topology of the CTRZ is strongly influenced by the channel orientation. The flow pattern observed for the CR swirler is indicative of a regular conical form of a vortex breakdown [44] while a wide-open conical form of a vortex breakdown [11] is observed in the CO swirler. The width of the CTRZ is larger in the CO swirler configuration ($x/D_{\text{h}} \approx$ 1.5) than the CR swirler ($x/D_{\text{h}} \approx$ 1.37). The length of the CTRZ extends beyond the field of view in both cases, yet the CTRZ is about to get closed in the CR swirler at $y/D_{\text{h}} =$ 6, which suggests the presence of a longer CTRZ in the case of the CO swirler.

Turbulent kinetic energy distributions (TKE) for the CR and the CO configurations are shown in Fig. 3.3. In general, high TKE values are correlated with the region of high shear, which can be inferred from the contours of out-of-plane vorticity shown in Fig. 3.4. It should be noted that the lowest extent of the field of view reaches $y/D_{\text{h}} \approx$ 0.2, where the primary and secondary jet flows are mixed and thus do appear as a single swirling jet flow. For the CR configuration, high turbulent kinetic energy values are observed along with the inner shear layer, which forms due to interaction between the swirling jet and the CTRZ, and along with the outer shear layer, which is associated with the interaction between the swirling jet and the CRZ. In the CO configuration, the inner shear layer is still due to the interaction between the swirling jet and the CTRZ. In accordance with the dramatic expansion of the swirling jet and then its interaction with the lateral confinement walls, the inner shear layer displays an L-shaped formation. On the other hand, the outer shear layer forms between the jet and the dome wall in the CO case. Accordingly, the maximum turbulent kinetic energies, magnitudes of which are more significant compared to the CR configuration, are observed close to the swirler exit in the vicinity of the dome walls.

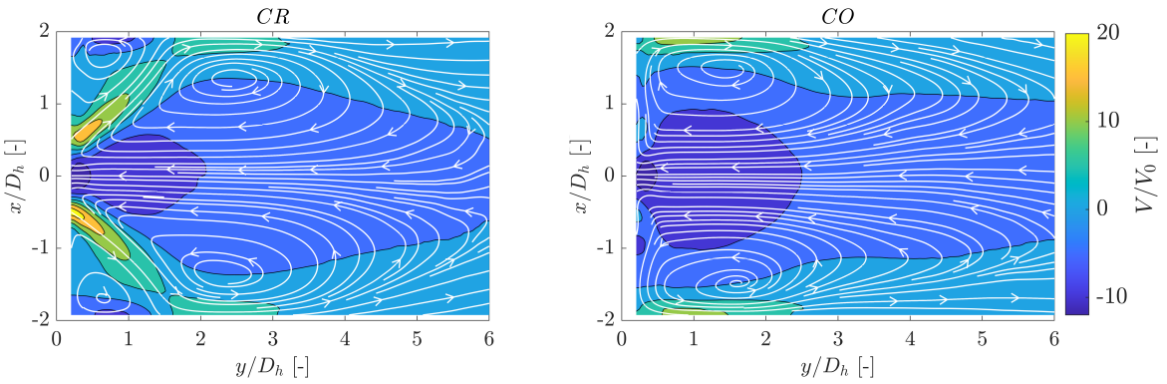


Figure 3.1: Contours of the time-averaged axial velocity component (the velocity component in the y direction, V/V_0) complemented with the flow streamlines for the CR (left) and CO (right) swirler configurations obtained from the PIV measurements

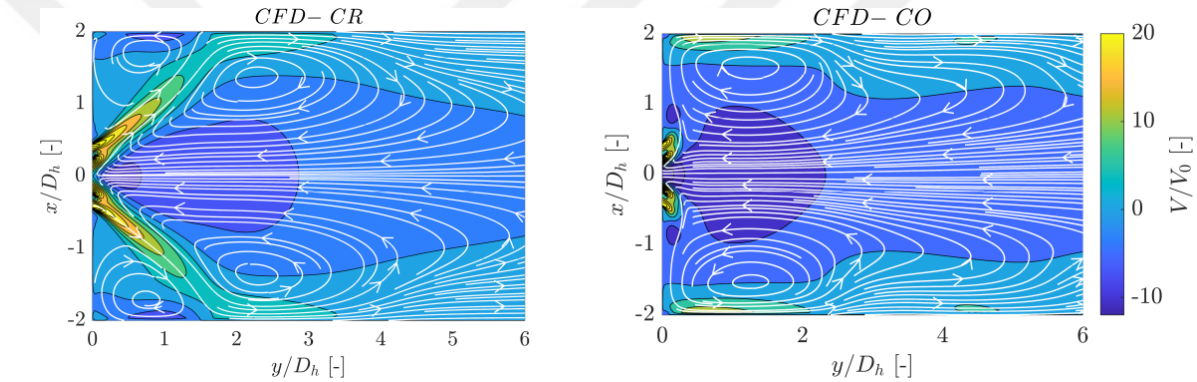


Figure 3.2: Contours of the time-averaged axial velocity component (the velocity component in the y direction, V/V_0) complemented with the flow streamlines for the CR (left) and CO (right) swirler configurations obtained from the numerical simulations

A similar comparison was also performed by Merkle et al. [20] between CO and CR swirler configurations in confined conditions yet at a relatively low swirl number (with swirl numbers of of 0.46 and 1.0 for the primary and secondary swirlers, respectively). They reported a regular conical form of vortex breakdown pattern in both co- and counter-rotating configurations, which means that there was no dome-attached jet flow in the CO configuration. This difference in the flow patterns, particularly for the CO configuration, can be attributed to the lower SN values considered in their study. They also reported that maximum TKE values are obtained in the CR configuration in the vicinity of the atomizer, which they explained by use of the Rayleigh's stability

criterion [84].

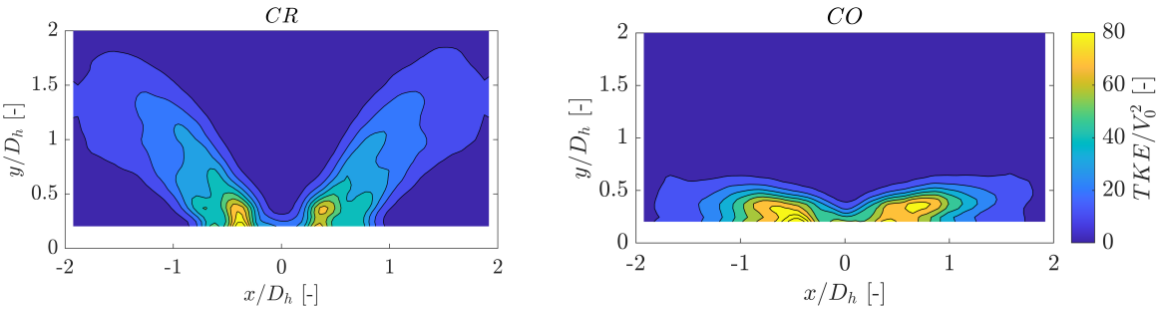


Figure 3.3: Contours of the normalized turbulent kinetic energy (TKE/V_0^2) distributions for the CR (left) and the CO (right) swirler configurations

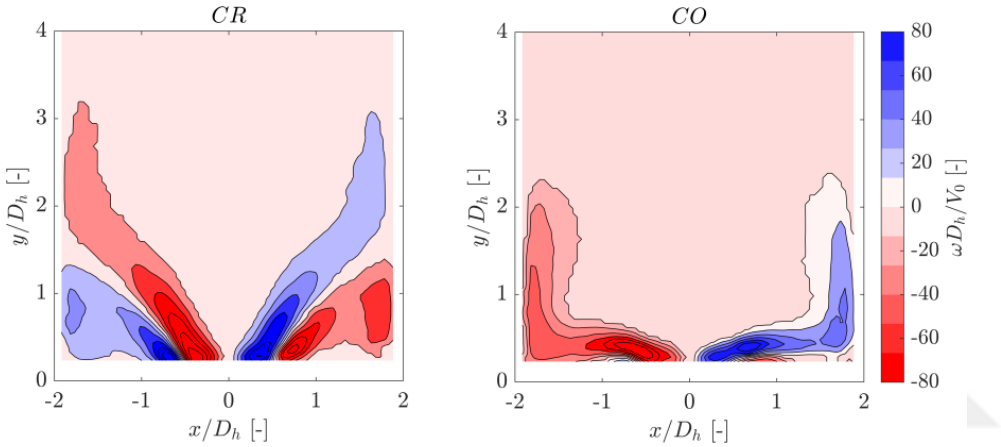


Figure 3.4: Contours of the normalized time averaged out-of-plane vorticity (i.e., z-vorticity, $\omega_z D_h/V_0$) for the CR (left) and the CO (right) swirler configurations

Normalized time-averaged axial, radial velocity and TKE profiles near the jet exit (y/D_{h}= 0.25) are shown in Fig. 3.5. In the CR swirler configuration, in accordance with the expansion angle of the jet ($35.62°$), high axial and radial velocity components are observed near x/D_{h}= 0.6 with similar magnitudes. A relatively high level of positive axial velocity values is observed in the CR swirler as the swirling jet flows through a narrow area between CRZ and CTRZ. Nevertheless, the peak negative axial velocities are similar for both swirlers at the center. The flow expands rapidly in the CO swirler, and relatively low axial velocity values are observed at this axial position. The rapid expansion of the flow is also evident from the elevated levels of radial velocity. As a result, a wide CTRZ forms in the CO configuration. The comparison of the TKE profiles reveals an increased level of turbulence for the CO configuration,

particularly at the radial locations of $x/D_{\mathrm{h}} > 0.5$. Multiple local maxima observed in the TKE profiles show a good agreement with the inner and outer shear layers of the swirling flow in both configurations (see Fig. 3.4).

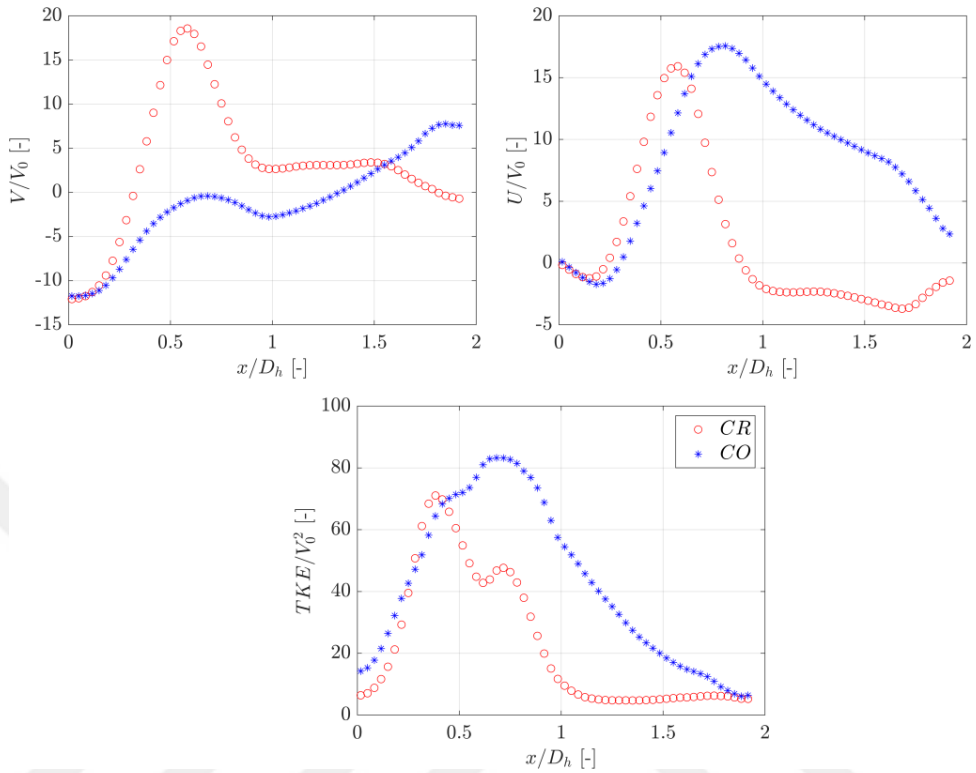


Figure 3.5: Time-averaged axial velocity (the velocity component in the y direction, V/V_0), radial velocity (the velocity component in the x direction, U/V_0) and turbulent kinetic energy (TKE) profiles at $y/D_{\mathrm{h}} = 0.25$

The flow fields obtained from the cross-stream measurements at the streamwise positions of $y/D_{\mathrm{h}} = 1$ and at $y/D_{\mathrm{h}} = 3$ are shown in Fig. 3.6. The resultant sense of rotations at these streamwise positions for the CO and CR configurations are counter-clockwise and clockwise, respectively. This observation justifies the dominance of the secondary swirler in the determination of the swirling flow behaviour. For the CR configuration, at the streamwise position of $y/D_{\mathrm{h}} = 1$, the swirling jet flows through a narrow region between the CTRZ and the CRZ, which appears as an annular contour pattern. Outside the vortex core, flow is directed radially outwards under the effect of swirling motion and the CRZ. The maximum tangential velocities are obtained in the annular jet region, as can be inferred from Fig. 3.7. The magnitude of the tangential velocity component decreases at the downstream position. A radially-inward

directed motion is present at y/D_{h}= 3, which is associated with the induced velocity of the toroidal vortex structure at this position (see Fig. 3.1). In the CO configuration, radially outwards and inwards velocity profiles are observed at the y/D_{h}= 1 and 3 positions, respectively, in accordance with the positions of the measurement planes with respect to the toroidal vortex. In both configurations, at the axial position of y/D_{h}= 3, a similar spiral flow topology is observed. Due to the square-shaped confinement, the swirling flow detaches from the wall surface around the corners, starts to move radially inwards, and its tangential velocity increases in view of the conservation of angular momentum. Due to the higher swirl momentum and thus higher swirl number at y/D_{h}= 3 (see Table 3.1) in the CO configuration, the high tangential velocity zones are located at outer radial positions with greater magnitudes compared to the CR configuration, as also shown in Fig. 3.7. The tangential velocity of the inwardly entrained flow then decreases, and the fluid is directed upstream towards the jet exit in the recirculation zone. The swirl numbers calculated at several streamwise positions are presented in Table 3.1. The SN values are obtained from the results of the numerical simulations, and only the regions with positive axial velocity values are included in the calculation. Therefore, at the axial positions close to the jet exit, relatively small SN values are obtained in the CO swirler due to the dominant radial velocity component rather than the axial velocity component associated with the rapid expansion of the jet.

Table 3.1: Swirl numbers at different streamwise positions calculated based on the results of the numerical simulations

Case	y/D$_h$ = 0.5	y/D$_h$ = 1	y/D$_h$ = 2	y/D$_h$ = 3
CR	-0.445	-0.350	-0.283	-0.272
CO	0.226	0.204	0.285	0.369

Turbulent kinetic energy distributions obtained from the cross-stream measurements at y/D_{h}= 1 are shown in Fig. 3.8. In the CR configuration, high TKE is mostly associated with the annular swirling jet at its interaction with the CTRZ. In the CO configuration, high TKE values are observed mostly around the confinement walls due to the rapid expansion of the swirling jet. When evaluated with the TKE distributions obtained from the streamwise planes, it can be concluded that strong turbulence

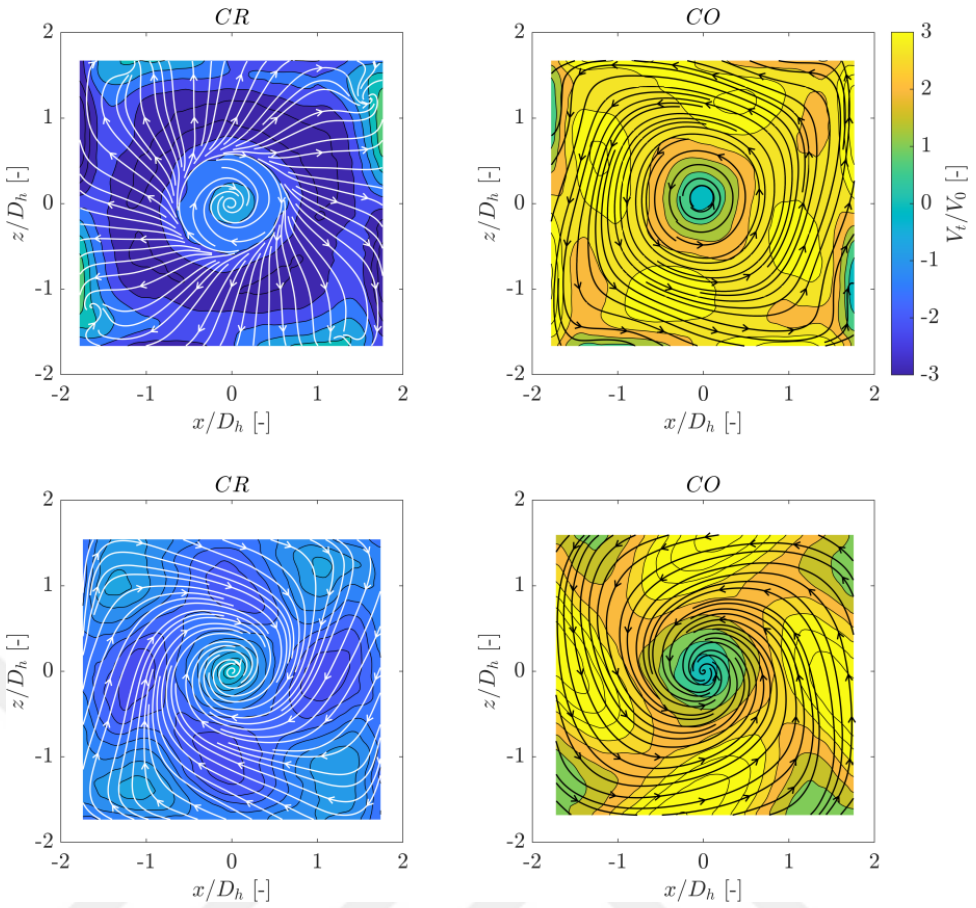


Figure 3.6: Contours of the time-averaged tangential velocity component (V_t/V_0) complemented with streamlines in the cross-stream planes at the axial positions of y/D_{h}= 1 (top row) and 3 (bottom row) for the CR (left) and the CO (right) swirlers

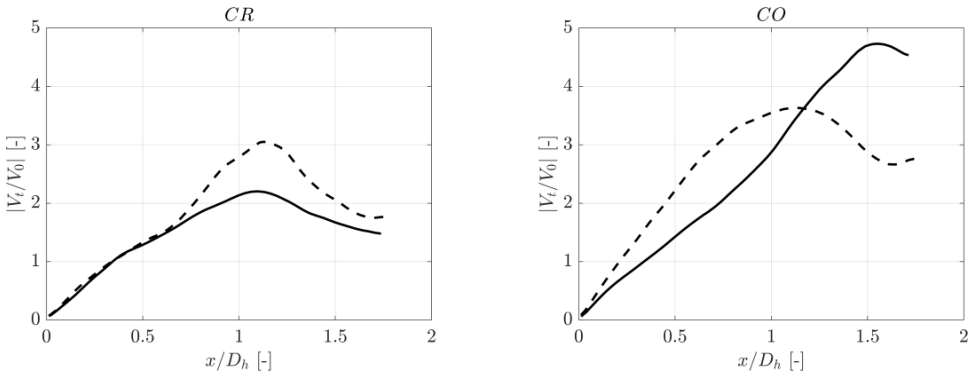


Figure 3.7: Time averaged tangential velocity profiles obtained from the results of the PIV measurements in the cross-stream planes at y/D_{h}= 1 (dashed line) y/D_{h} =3 (full line) for the CR (left) and the CO (right) swirlers

effects are present in the vicinity of the dome and confinement walls associated with the rapidly expanded jet in the CO configuration, which may be considered detrimental in terms of mixing and combustion efficiency in reactive flow conditions.

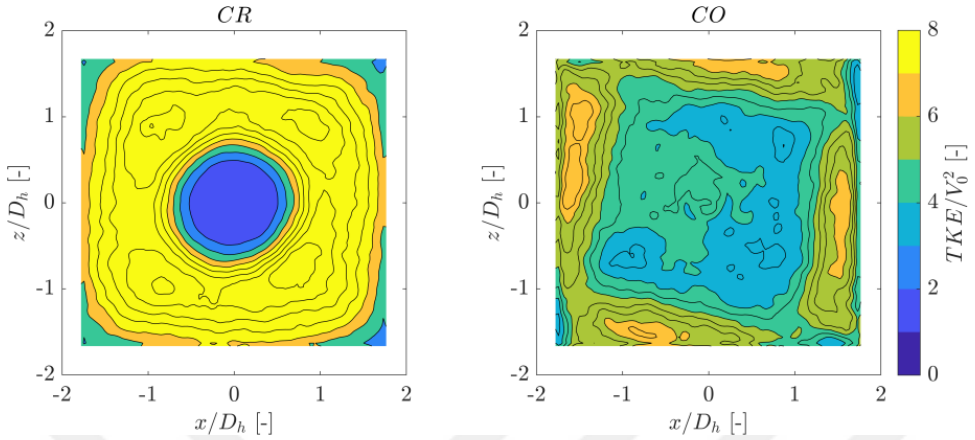


Figure 3.8: Contours of turbulent kinetic energy (TKE/V_0^2) obtained from the PIV measurements in the cross-stream plane at y/D_{h}= 1

The effect of the channel rotation on the mass flow rate inside the CTRZ is also investigated. The reversed mass flow rate is calculated by integrating the Eqn. (3.2) using the normalized axial velocity values, which are shown in Fig. 3.14. The borders of the integral are defined by the use of the negative axial velocity values from the center line axis to the center of the CTRZ. The center of the CTRZ is estimated by using the eyes of the recirculation regions as roughly observed in the streamline plots (see Fig. 3.1; y/D_{h}= 2 for CR and y/D_{h}= 1.75 for CO swirlers.) as described by Kilik [85] and applied by Kiyici and Percin [24]. Almost 2.2 times more air recirculates in CTRZ of the CO swirler, which signifies the influence of the channel rotation and thus resultant swirl number. It can be hypothesized that higher resultant tangential momentum in the CO swirler yields a higher negative axial pressure gradient, which results in an increase in the speed of the recirculating air flow (see Fig. 3.14) and higher recirculating mass flow rate. In addition, these profiles also show the maximum width of the CTRZ where the axial velocity turns from negative to positive. The width of the CTRZ is measured as R/D_{h}= 1.5 and 1.333 for the CO and the CR swirlers, respectively, which also justifies the increased size of the CTRZ in the CO configuration.

$$\dot{m}_{reversed} = 2 \cdot \pi \int_0^R \rho \cdot U \cdot r \cdot dr \tag{3.1}$$

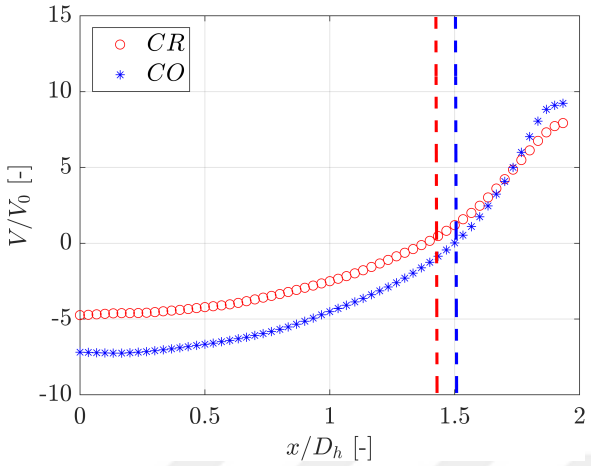


Figure 3.9: Time-averaged axial velocity (the velocity component in the y direction) profiles obtained from the streamwise PIV measurements at the center of the CTRZ for the CR (red circles) and CO (blue asterisks) swirlers. The vertical dashed lines represent the radial location where the axial velocity turns from negative to positive values.

The numerical results are validated by means of direct comparison with the PIV measurements at y/D_{h}= 1 and y/D_{h}= 3 as shown in Fig. 3.17. It should be noted that experimental data is not available in close proximity to the walls due to excessive reflections and thus increased uncertainties in the PIV measurements. Nevertheless, there is a fairly good agreement between the experimental and numerical results, which justifies the use of numerical results for the analysis of flow topology and swirl number calculations.

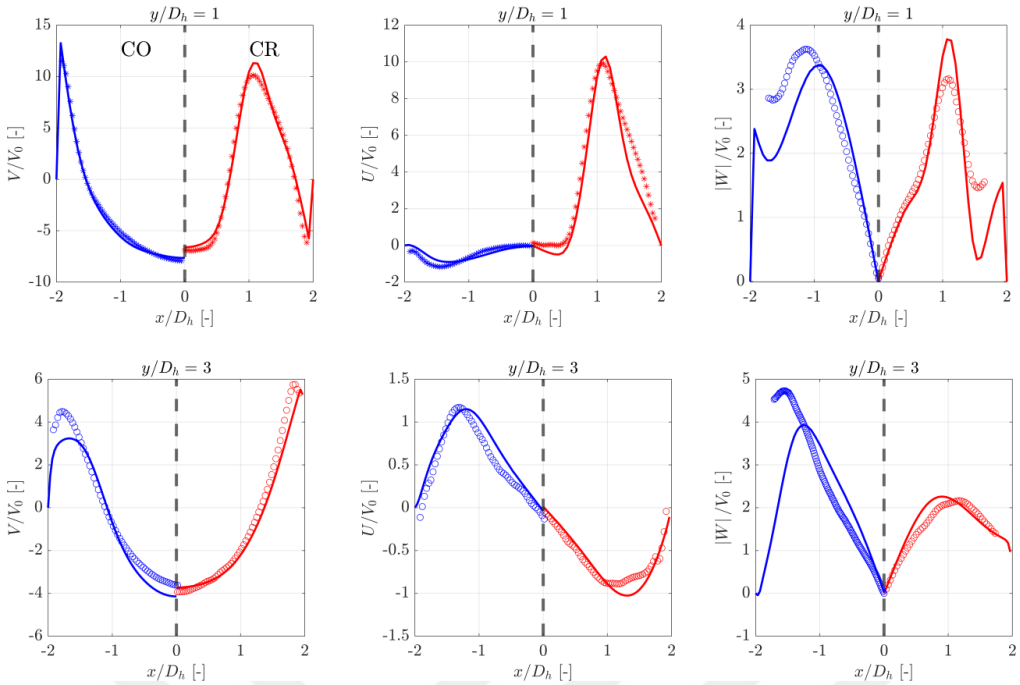


Figure 3.10: Comparison of the time-averaged axial velocity (the velocity component in the y-direction, V/V_0), radial velocity (the velocity component in the x-direction, U/V_0) and the tangential velocity (the velocity component in the z-direction, $|W|/V_0$) profiles obtained from the PIV measurements (symbols) and numerical simulations (full lines) for the CO (blue) and the CR (red) configurations in the streamwise plane aligned with the center of the swirler

3.1.2 Coherent flow structures

In this section, the coherent structures of the swirling flow fields are extracted by means of the snapshot POD and S-POD techniques. Both PIV methods are applied to the velocity data acquired in the highly time-resolved PIV measurements, which focused on the half of the confinement section in the lateral direction (see Fig. 2.12). In literature, there are studies that compare the POD and S-POD mode shapes of a single radial swirler [43], [44]. In this study, a similar performance assessment is conducted for a radial-radial swirler configuration. Axial (y-component of velocity measured in the streamwise central plane) and radial velocity (x-component of velocity measured in the streamwise central plane) components are stacked to form a column vector in the snapshot POD, while only the radial velocity component is used in the S-POD

analysis, which has been proven to be the best indicator for the determination of coherent structures in swirling flows [44].

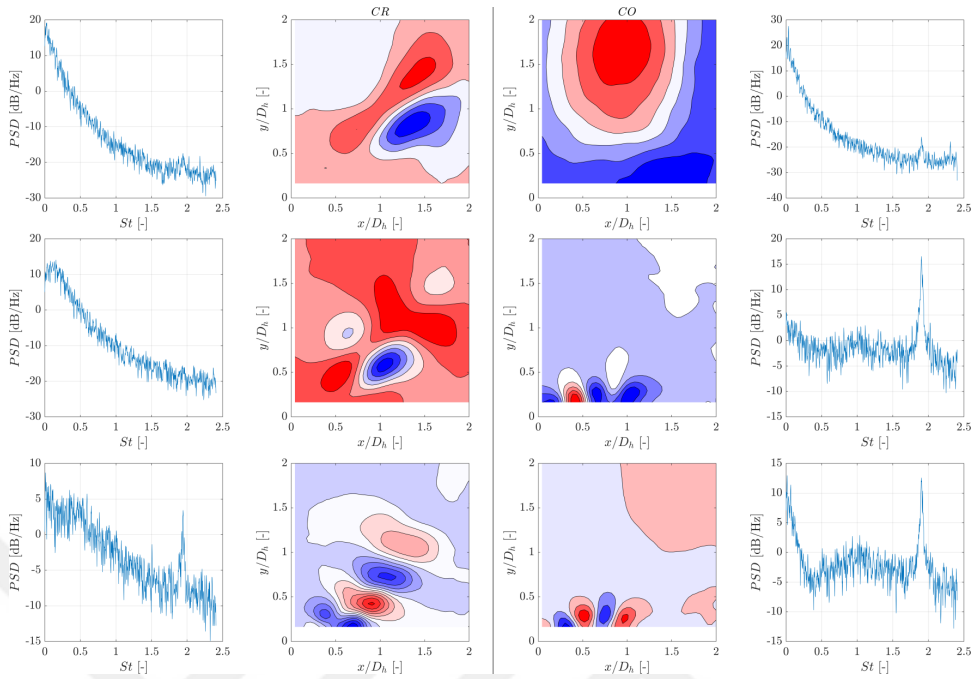


Figure 3.11: The first three most energetic modes and the power spectral densities of their time coefficients obtained from the snapshot POD analysis for the CR (left) and CO (right) swirlers

The first three most energetic mode shapes obtained from the snapshot POD analysis and the power spectral densities for the corresponding time coefficients are shown in Fig. 3.11. In the contour plots, the center of the jet exit corresponds to $x/D_h = 0$, whereas the confinement wall is at $x/D_h = 2$. On the CR side, the first two mode shapes obtained from the snapshot POD analysis represent low-frequency interaction dynamics between the CTRZ, the expanding swirling jet, and the CRZ. The third mode corresponds to the convective Kelvin-Helmholtz instability of the swirling jet shear layers. The power spectral density of the third mode time coefficient has a vague peakedness in the region from 0.4 to 0.5 and a coherent peak at $St = 1.9$ ($St = fD_h/V_{jet}$), which corresponds to a frequency of 1.2 kHz. The classical POD is rather a rigid method that does not necessarily isolate a coherent phenomenon in a single mode [44]. In this case, the convective Kelvin-Helmholtz instability and another high-frequency phenomenon appear in a single mode. As will be shown later, this high-frequency occurrence corresponds to the precessing vortex core, which forces

the flow with its frequency through the convective instability of the shear layer[30]. On the CO side, the first mode corresponds to a low-frequency pulsating motion of the CTRZ. The second and the third modes also have a high-frequency content at $St = 1.9$ and the spatial patterns indicate the presence of a PVC in this case[44]. The third mode combines a low-frequency phenomenon with the PVC, which is a result of the fact that the classical POD approach is based on maximization of the TKE rather than isolating individual occurrences in a single mode **weiss**. It is also observed that the frequency of the PVC emerges in a number of modes obtained from the classical snapshot POD analysis in addition to the first three modes presented here, which justifies the global influence of the PVC. The energy levels of the first three snapshot POD modes are 8.94%, 6.92%, 5.79% for CR swirler and 16.97%, 5.51%, 5.06% for CO swirler, respectively.

The results of the S-POD analysis allow for the assessment of the coherent flow structures as shown in Fig. 3.12 in descending order in terms of their energy content. The first two modes of the CR configuration are identical to those obtained from the conventional snapshot POD analysis corresponding to the low-frequency interaction between the jet and the CRZ at St= 0.155 and shear layer dynamics at St= 0.216, respectively. The third mode represents the PVC at St=1.9, which appears as the second mode in the CO configuration at the same St number. The sense of rotation does not affect the frequency of the PVC, although its energy level is much higher in the CO swirler. This can be attributed to relatively low shear dampening in the CO configuration between the co-rotating primary and secondary jet flows. The first mode for the CO swirler is also identical to that of the snapshot POD analysis, whereas the third mode likely to represent a shear-layer instability at St= 0.638.

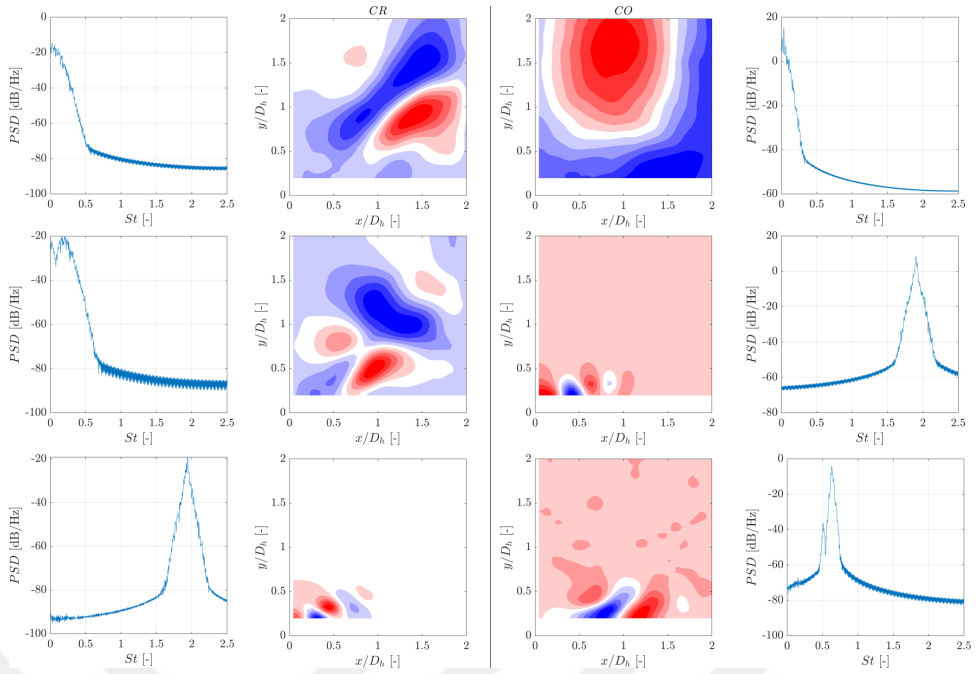


Figure 3.12: Results of the spectral-POD analysis (mode shapes and power spectral densities) for the CR (left) and CO (right) swirlers

3.2 Effect of the confinement ratio

In the present study, the effect of confinement on the differently orientated radial-radial type swirlers is assessed in two main parts. In the first part, the time-averaged stream-wise velocity fields of the numerical and experimental studies are discussed and compared. This section starts with a discussion of the experimental results. Next, numerical results are compared with experimental data for both CO and CR swirlers. In addition, vorticity contours are also presented to reveal shear layer interactions right after the swirler exit where the support connections prevent the illumination. In the second part, S-POD analysis results are provided to discuss coherent structures based on the fast 2D2C PIV measurements. Experimental and numerical data of axial (y-component of velocity, V) and radial (x-component of velocity, U) velocity components are normalized by the mean swirler inlet velocity ($V_0 = 0.89\ m/s$)

3.2.1 Time-averaged flow fields

The time-averaged flow fields for CO and CR swirlers under the different confinement ratio levels are shown in Fig. 3.13. Starting from the CR swirler, the confinement walls change the flow structures remarkably in several aspects. First, the topology of the CTRZ is affected by the confinement walls. For the unconfined swirling jet, a relatively small CTRZ exists directly at the exit of the jet and it extends until approximately $y/D_{\mathrm{h}} < 2.0$. In addition to the unconfined configuration, the corner recirculation zone (CRZ), which is formed between the outer shear layer and the confinement walls, is observed for all confined cases. For the high confinement case, in the region of $y/D_{\mathrm{h}} < 1.5$, the swirling jet flow displays similar features to the unconfined jet with relatively low expansion and a small CTRZ located at the exit of the jet. However, it starts expanding at about $y/D_{\mathrm{h}}>2$ and attaches the side walls. Additionally, the swirling jet's radial expansion increases with decreasing confinement ratio. The radial expansion angle is (the angle between the centerline axis of the swirler to the flow attachment location on the side wall) calculated as 60.6, 59.7 and 38.2 degrees for the low, the medium and the high confinement cases, respectively. The radial expansion behavior can also be attributed to the presence of the walls and the associated CRZ. The size of the CRZ increases as to confinement ratio increases due to relatively lower radial expansion. In addition, the CTRZ connects with a second larger recirculation zone for the high confinement ratio case, as evident from Fig. 3.13. This observation agrees with the findings of Fu et al. [25], who reported that there exist two recirculation zones at higher confinement levels for a radial-radial swirler. Contrary, a single CTRZ is present at the exit of the swirler for smaller confinement levels. The other important effect of the confinement is the length of the CTRZ. The CTRZ closes in the case of the low confinement at approximately $y/D_{\mathrm{h}} =4.75$, whereas it exceeds the measurement planes of higher levels of the confinement cases. It should be noted that the types of vortex-breakdown also differ as to the confinement ratio changes. Bubble type vortex-breakdown is [11] observed in unconfined and high confinement cases of CR swirler while regular conical type vortex-breakdown observed [44] for other confined cases of CR swirler.

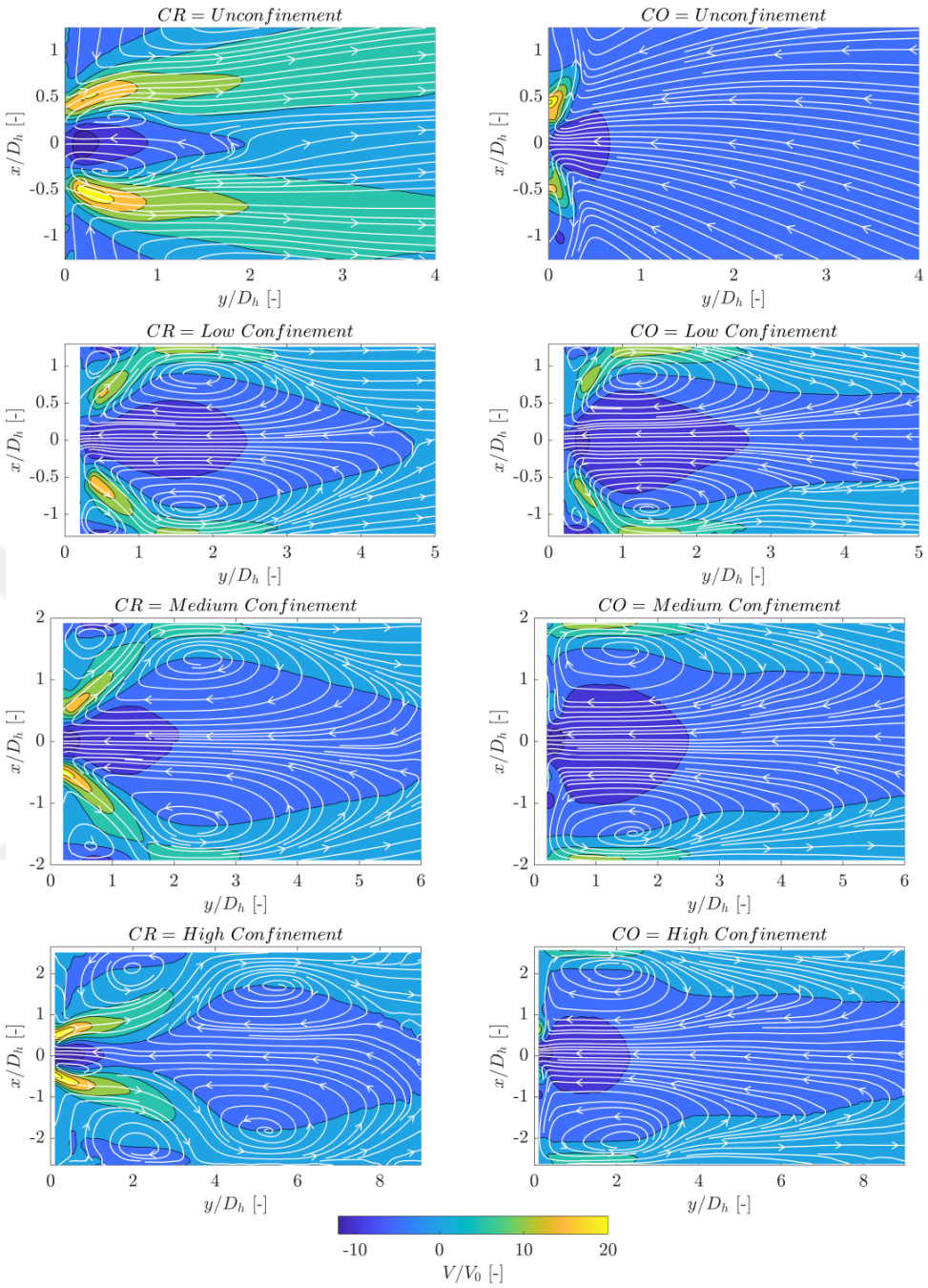


Figure 3.13: Contours of the time-averaged axial velocity component (the velocity component in the y direction, V/V_0) complemented with the flow streamlines for the CR (left) and CO (right) swirler configurations obtained from the PIV measurements under different confinement ratio conditions

Remarkably high radial expansion of the swirling jet flow is observed in CO swirler and the degree of the radial expansion decreases with decreasing confinement. The vicinity of the confinement walls does not affect the radial expansion until a certain level. As a result, the CRZ is only observed for the lower confinement case. The radial expansion angle calculated only for this case (for other CO cases flow directly attaches to the dome; thus, the angle is assumed to be 90 degrees) is 68.8 degrees. In all confined cases, the CTRZ exists and the length of this flow reversal zone exceeds the measurement plane for all cases. At higher confinement levels, the wide-open conical form of vortex-breakdown [11] flow structure is observed, while the regular conical vortex-breakdown structure is observed in the low confinement case [44].

The channel orientation and confinement ratio effect is also investigated on the mass flow rate inside the CTRZ. The reversed mass flow rate is calculated by integrating the Eqn. (3.2) using the axial velocity values shown in Fig. 3.14. The borders of the integral are defined by the negative axial velocity values from the centerline axis to the center of the CTRZ as described by Kilik [85] and applied by Kiyici and Percin [24]. The upper border of the integral also represents the width of the CTRZ. The reversed mass flow rate values are normalized by the result of the medium confinement ratio case of the CR swirler. As shown in Table 3.2, the maximum normalized reversed mass flow rate is observed in the high confinement ratio case of the CO swirler. For each confinement level, a higher level of reversed mass flow rate is observed in the CO swirler due to the stronger adverse pressure gradient at the center of the recirculation zones.

$$\dot{m}_{reversed} = 2 \cdot \pi \int_0^R \rho \cdot U \cdot r \cdot dr \tag{3.2}$$

The width of the recirculation zone for each case is shown in 3.2. The wider CTRZ occurs (where the V/V_0 equals to zero) in CO swirler for each confinement configurations as observed in Fig. 3.14. At low confinement ratio values, the width of the CTRZ is almost similar in both CO and CR swirlers but the size differs as the confinement ratio increases.

The turbulent kinetic energy (TKE) contours for different confinement ratios are shown in Fig. 3.15. It is clear that high TKE values are observed around the swirler

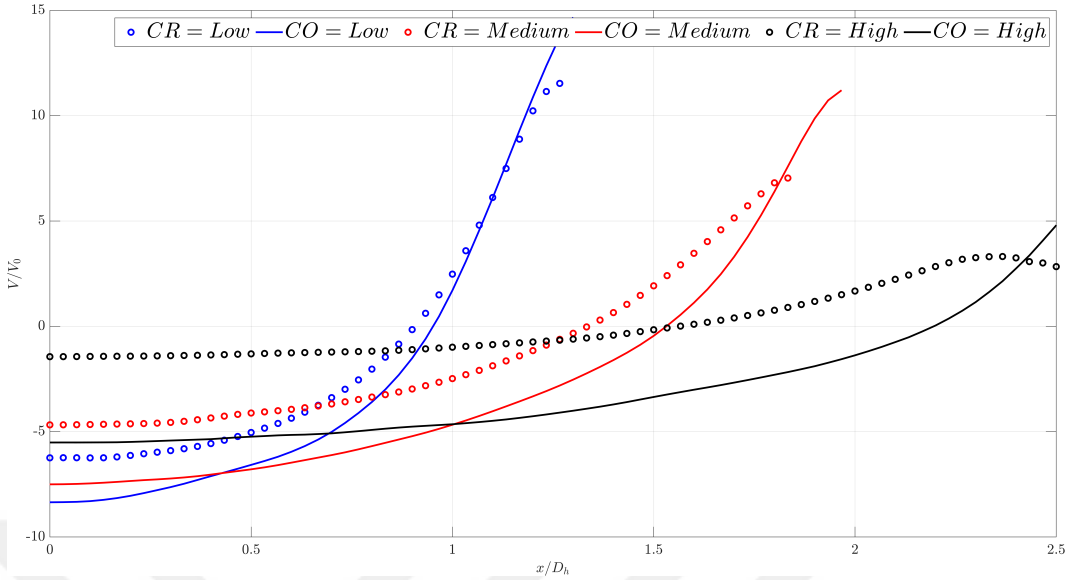


Figure 3.14: Time-averaged profiles of the velocity component in the y direction (V/V_0 corresponding to axial velocity component) along the center of the recirculation zones for the confined cases

Table 3.2: Normalized reversed mass flow rates (normalization is performed using the medium confinement cases of the CR swirler) and width of the CTRZ

Case	Normalized $\dot{m}_{reversed}$	D/D_{h}
CR= Low Confinement Ratio	0.431	1.800
CR= Medium Confinement Ratio	1	2.667
CR= High Confinement Ratio	0.481	3.000
CO= Low Confinement Ratio	0.637	1.866
CO= Medium Confinement Ratio	2.268	3.000
CO= High Confinement Ratio	3.536	4.334

exit, and TKE distribution is correlated with the inner (between swirling jet and CTRZ) and the outer (between the swirling jets and the environment) shear layers for all cases. Also, the maximum TKE values in the CO swirler are higher than in the CR swirler at the same confinement ratio levels. For unconfined conditions, the swirling jet becomes a wall jet in the CO swirler and TKE decays rapidly, but higher TKE regions are observed in the CR swirler farther from the jet exit. The maximum level of the TKE occurs in the inner shear layer in the CO swirler while it occurs in the outer shear layer in the CR swirler. For the low confinement ratio, similar TKE distribution is observed for the CO and CR swirlers due to the same types of vortex breakdown. Interestingly, higher TKE values are still observed in the CO swirler after the flow attaches to the side walls. For medium and high confinement ratio cases, the swirling jet becomes a wall jet in CO swirler and TKE rapidly decays, as observed in the unconfined condition. As the confinement ratio increases, the TKE value becomes more noticeable at further points from the jet exit in the CR swirler. For confined cases, as the confinement ratio increases, the level of the maximum TKE decreases.

The numerical flow fields are shown in Fig. 3.16 for confined cases of CO and CR swirlers. Similar flow patterns are obtained by numerical solutions when compared to the experimental data (see Fig. 3.13). The CFD method predicts the location of the eye of the CTRZ positions fairly well. However, the experimental and numerical data results differ at more downstream locations. For example, the CTRZ is prone to close for the high confinement cases of the CR swirler in the experiment, but the same trend is not observed in numerical analyses. Additionally, the length of the CTRZ is underpredicted in the numerical simulations, as seen in the low confinement cases of both swirlers.

The normalized axial and radial velocity profiles obtained experimentally and numerically at y/D_{h}= 0.5, 1 and 2 are shown in Fig. 3.17. Overall, the trend of the experimental data is well-predicted by the CFD simulations for all cases. For the medium and the high confinement ratio cases of the CR and the CO swirlers, the axial and radial velocity profiles are in good agreement with experimental data at y/D_{h}= 0.5. Nevertheless, the radial expansion (peak axial velocity magnitude location) is underpredicted by the CFD for the CO swirler of the low confinement case; thus, a narrower

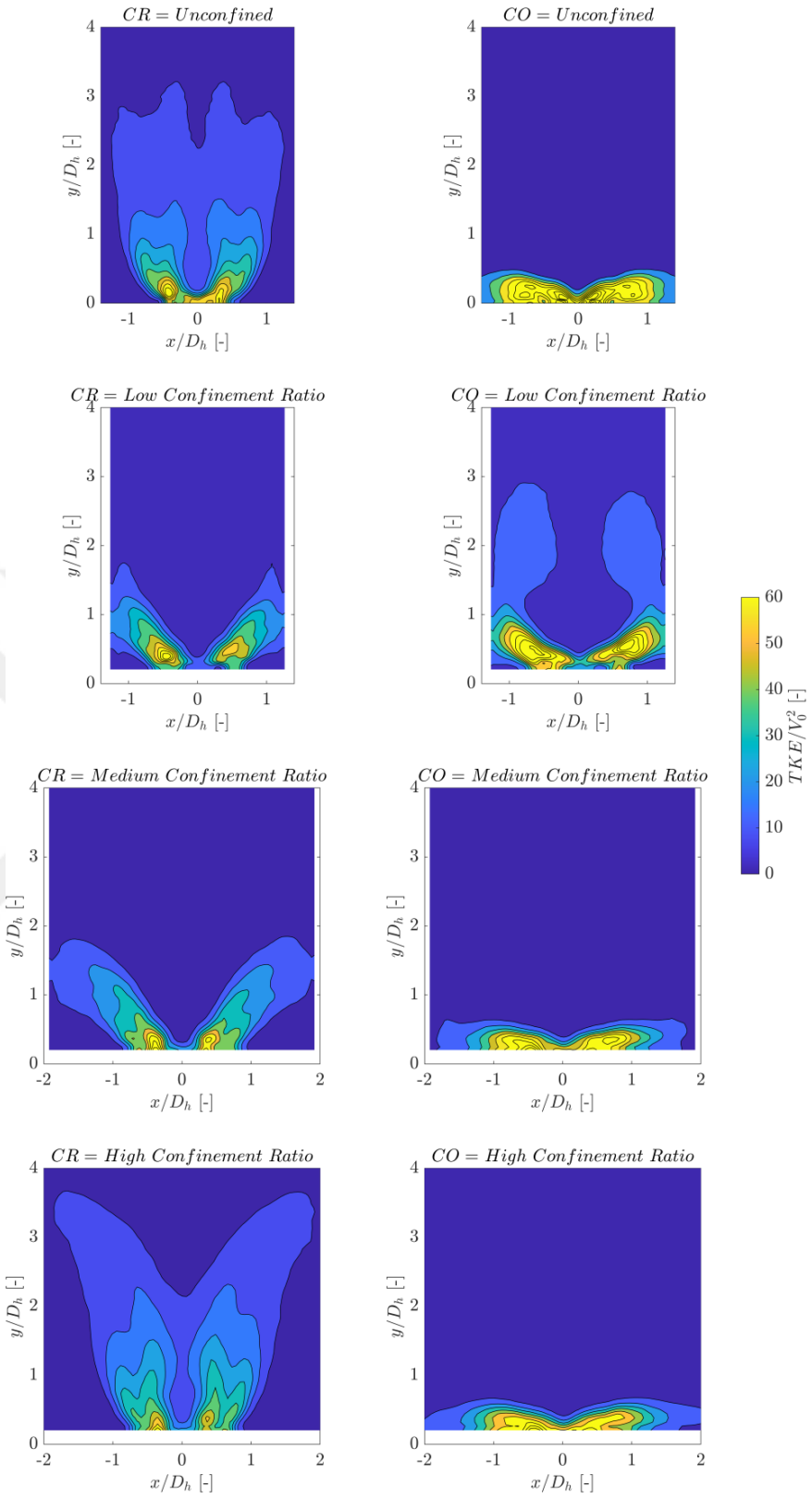


Figure 3.15: Contours of the normalized turbulent kinetic energy (TKE/V_0^2) distributions for the CR (left) and the CO (right) swirler configurations under different confinement ratio conditions

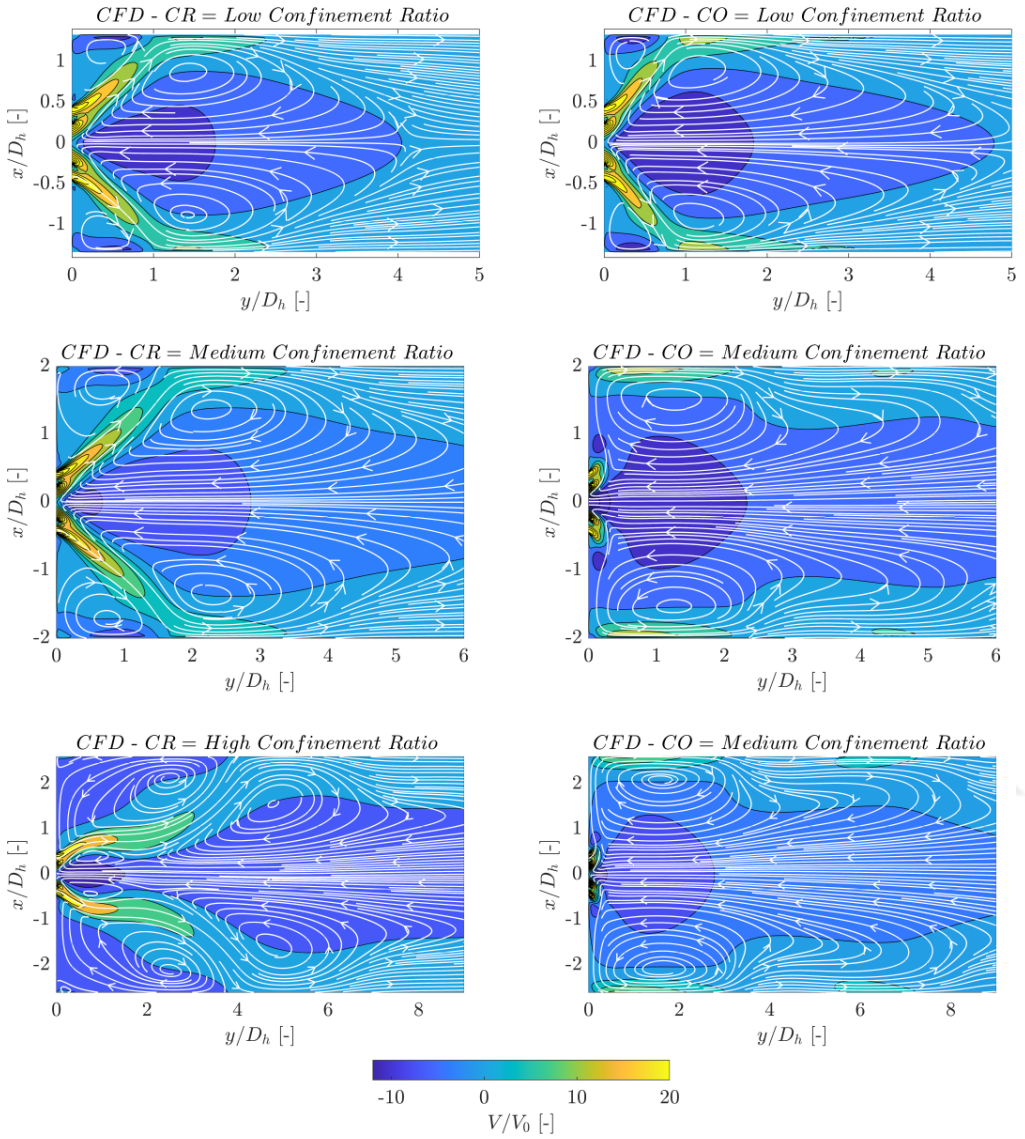


Figure 3.16: Contours of the time-averaged axial velocity component (the velocity component in the y direction, V/V_0) complemented with the flow streamlines for the CR (left) and CO (right) swirler configurations obtained from the numerical simulations under different confinement ratio conditions

CTRZ occurs at this location. Even though the radial expansion is well predicted for the CR-low confinement ratio case, CFD predicts a stronger negative axial pressure gradient and results in lower centerline velocity magnitude than experimental data. Also, the peak axial velocity is remarkably higher than the experimental data. The magnitude of the peak axial velocity increases as the radial expansion decreases, and hence the maximum peak axial velocity is observed for the high confinement case of the CR swirler. The radial locations of the peak axial velocity are predicted as x/D_{h}= 0.85, 0.7 and 0.633 for the CR swirler of low, medium and high confinement ratio cases, respectively. For the CO swirler, only the low confinement ratio case shows a flow structure different from the wall-attached flow structure. The peak axial velocity is observed at x/D_{h}= 1, and the magnitude is lower than all the CR swirler cases. At y/D_{h}= 1, the centerline velocity is slightly underpredicted for the CR swirler of the low and high confinement ratio cases, while a better agreement is obtained for the medium confinement ratio condition. At this location, the flow attaches to the side wall for the low confinement ratio situation, and the rest are still expanding radially. The radial velocity profiles are in a reasonable agreement with experimental data for the CR swirler. For wall-attached flow cases of the CO swirler, the peak axial velocity occurs between the side wall and CTRZ. The centerline axial velocity decreases as the confinement ratio increases for CO swirler. In contrast, the opposite occurs for CR swirler, which indicates the adverse pressure gradient is affected by the channel orientation and the confinement walls.

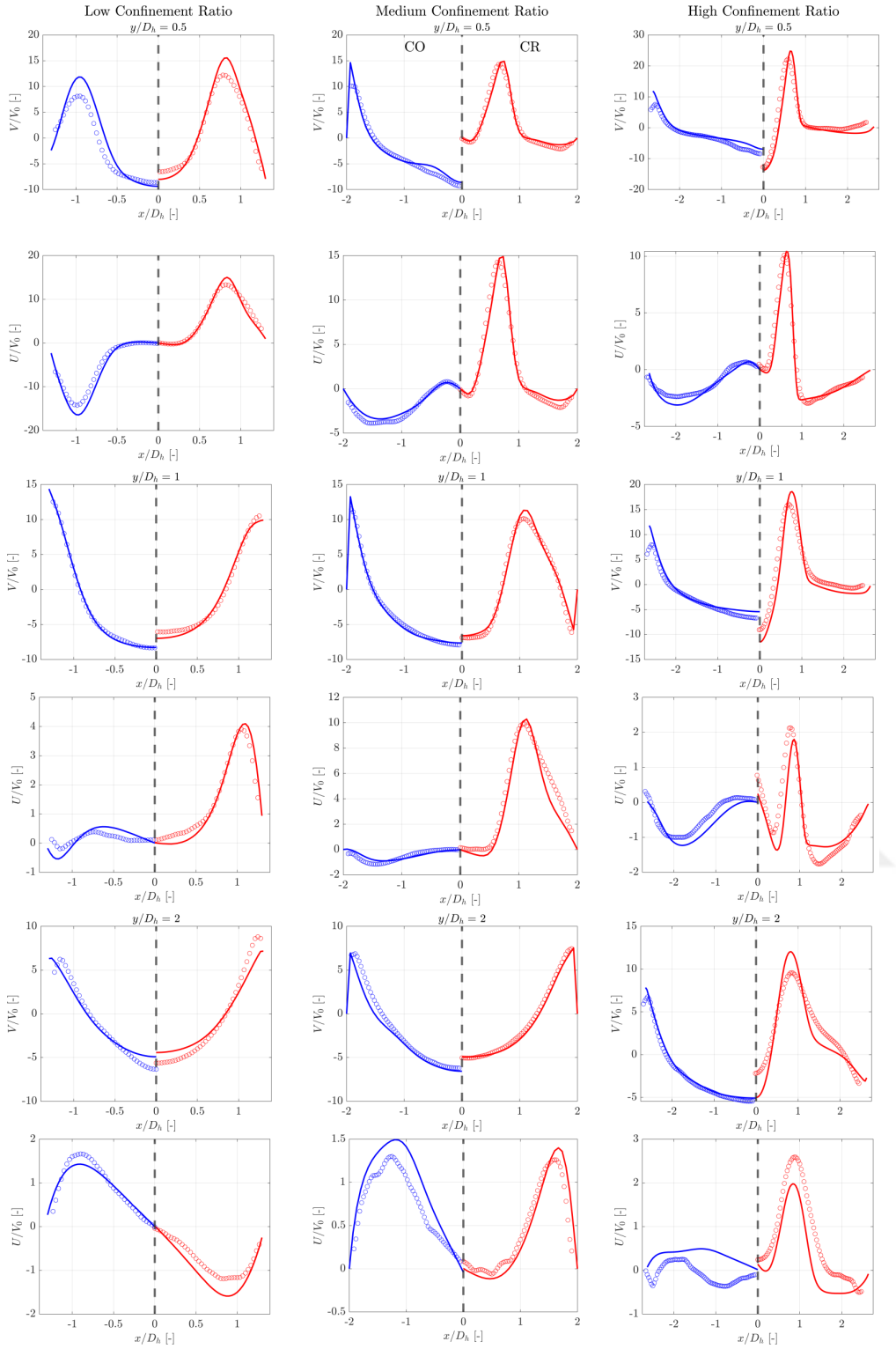


Figure 3.17: Comparison of the time-averaged axial velocity (the velocity component in the y-direction, V/V_0), radial velocity (the velocity component in the x-direction, U/V_0) profiles obtained from the PIV measurements (symbols) and numerical simulations (full lines) for the CO (blue) and the CR (red) configurations in the $y/D_h = 0.5$, 1 and 2

The radial velocity almost decays at y/D_{h}= 1 for the CO swirler, which is incomparably lower than the radial velocity magnitude of the CR swirler cases. At the further locations, the discrepancy between the numerical and experimental results of the centerline axial velocity is getting more remarkable for CR cases of the low and high confinement cases. This is also a sign that the length of the CTRZ is miscalculated in the CFD analysis. Scale-resolving methods would be useful for more accurate length prediction, but sometimes even these methods can fail [80]. Contrary to this, centerline axial velocity is still in good agreement for medium confinement cases of both swirlers. All configurations provide a similar axial velocity profile trend except for the high confinement ratio case of the CR swirler, which still does not attach to the side walls. After the flow attaches to confinement walls, it heads for the centerline axis; thus, the sign of the radial velocity changes for low and medium confinement cases of CO swirler. Moreover, the magnitude of the radial velocity increases for these configurations, while the radial velocity magnitude is negligible for the high confinement ratio case. Again, the radial velocity profiles are in good agreement with experimental data at y/D_{h}= 2.

For a better understanding of the shear layer mechanisms, the normalized vorticity (normalized with swirler exit velocity and swirler hydraulic diameter) contours are shown in Fig. 3.18. These contours reveal several interaction mechanisms such as primary-secondary jets, secondary jets-CRZ, primary jets-CTRZ, and secondary jets-wall interactions regarding the type of swirler and level of confinement. It is seen that the confinement walls have a crucial impact on the shear layer. For the CR swirlers, a stronger shear layer comes out as the outer shear layer, resulting from the interaction between CRZ and the secondary swirling jet. Yet, the outer shear layer's magnitude slightly decreases as the confinement level increases. For the CO swirler, the outer shear layer forms between secondary jets and dome walls due to the absence of a CRZ, and stronger outer shear is observed as in the CR swirler. However, the magnitude of the outer shear layer increases as the level of the confinement increases, contrary to the CR swirler. It should be noted that the primary and secondary swirling jets do not mix immediately after swirler exit, which results in the formation of a small recirculation zone between swirling jets $\pm$ x/D_{h}=0.2-0.3) for all configurations.

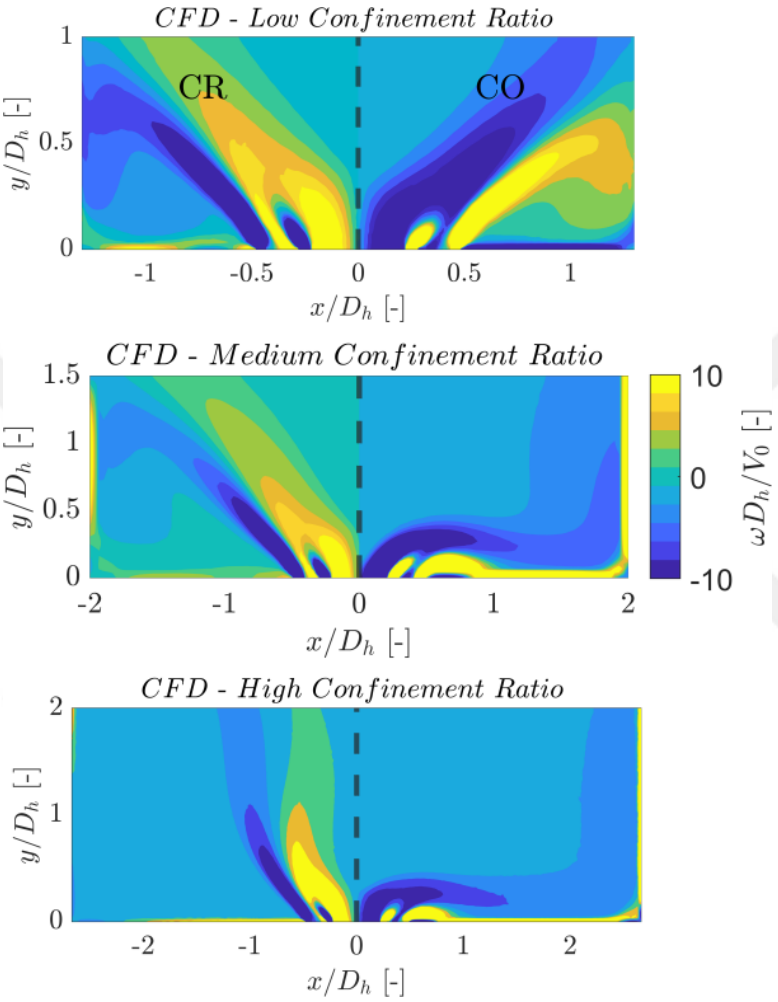


Figure 3.18: Contours of the time-averaged normalized vorticity distribution ($\omega D_h/V_0$) for the CR (left) and CO (right) swirler configurations obtained from the numerical simulations under different confinement ratio conditions

The SN values are calculated using the simulation results in the positive axial velocity regions, and the results are shown in Table 3.3. It is seen that the change of the SN number at different planes is highly associated to the channel orientation and confinement ratio. Close to the jet exit, higher swirl momentum is observed in the regular type conical vortex breakdown cases, while lower SN is seen in wide-open type conical and bubble type vortex breakdown. For the lowest confinement ratio cases, similar flow patterns occur between the CO and CR swirlers. Lower shear strength in the CO swirling jets leads to higher SN. However, the flow fields remarkably change in medium and high confinement ratio cases, and higher SN occurs in CR swirlers. In these cases, flow rapidly expands, and axial velocity passes a narrower area between the confinement walls and CTRZ that is accelerating the flow. Also, the swirling momentum decays due to the high shear stress in this zone. Thus, lower SN values are observed in relatively higher confinement ratio cases of the CO swirler. The SN decreases in CO swirlers and then increases at more downstream locations. The axial momentum decreases when the width of the CTRZ starts to decrease, which leads to higher SN momentum. At y/D_{h}= 3 effect of the wall jet is still observable in medium confinement case of the CR swirler thus SN decreases quite a bit comparing to y/D_{h}= 2. Nevertheless, CTRZ moves radially to the centerline of the burner in the low confinement case of the CR swirler; as a result, the SN increases remarkably due to decreasing the axial momentum. Even the stronger swirl momentum is observed in CR swirler close to jet exit planes; higher SN occurs in CO swirler at y/D_{h}= 3 due to the radially inward motion of the CTRZ of the CO swirler.

Table 3.3: Absolute SN at $y/D_h = 0.5$, 1, 2 and 3 for the CR and CO swirlers under different confinement conditions

	Low Confinement Ratio		Medium Confinement Ratio		High Confinement Ratio	
y/D$_h$	CR	CO	CR	CO	CR	CO
0.5	0.45	0.802	0.445	0.226	0.385	0.205
1	0.487	0.573	0.35	0.204	0.272	0.164
2	0.31	0.582	0.282	0.285	0.291	0.193
3	0.497	0.858	0.272	0.369	0.119	0.266

In addition to numerical study of the confined cases, performance of RANS and LES is compared in unconfined condition of the CR swirler. RANS and LES contours are shown in Fig 3.19 and Fig. 3.20, respectively. In these figures, white borders represents the recirculation zone. The length of the recirculation zone is measured as 58 mm in slow PIV measurements (see Fig. 3.13). The length of the recirculation zone is computed as 60 mm in LES while it is around 140 mm in RANS simulations. RANS computes the 2.333 times longer recirculation zone than reality but LES predicts the length well. Additional recirculation zone occurs in RANS around the shear layers between the swirling jet and ambient flow which are not observed in the experiment. The other remarkable difference is the flow expands more radially in LES compared to RANS. After the axial location of 220 mm, the ambient air still entrains to swirling jet in a radial location of 120 mm in RANS while the swirling jet pushes outward the ambient air due to higher radial expansion.

The normalized axial and radial velocity profiles are compared with experimental data in Fig. 3.21. At y/D_{h}= 0.5, LES is in good agreement with experimental data but RANS fails to provide reasonable agreement. RANS overpredicts distinguishably the centerline velocity while LES slightly underpredicts it. The centerline velocity is important close to jet exit because it has direct relation between the recirculation zone length. Also, LES in good agreement with the experimental data for radial velocity component but the peak radial velocity is overpredicted in RANS simulation. LES is still in good agremeent with experimental data at y/D_{h}= 1 and the centerline velocity is slightly underpredicted again. The huge discrepancy at the centerline axial velocity between RANS and experiments still exists and RANS predicts the centerline axial velocity two times of the experimental value. The maximum and minimum values of the radial velocity is overpredicted in LES but the radial velocity profile is follows the trend of the experimental data. At this location, RANS follows the trend of the measured radial velocity profile but the peak velocity is predicted extremely higher than experiment. At the final location of y/D_{h}= 1, the recirculation zone is about the close in LES but it is already close in experiment. However, the recirculation zone is still open in RANS simulation. Starting from the jet exit, the centerline velocity remarkable different in RANS than experiment which causes the miscalculated recirculation length. LES is in reasonable agreement with radial velocity profile at

this location but RANS fails to predict well the radial velocity. In conclusion, LES provides well-agreed results with the experimental data. Even RANS shows a good agreement in confined condition, it is not capable of solving the highly swirling flow in unconfined condition. In Fig.3.22, r.m.s velocity components from the PIV and LES are compared. Overall, LES also predicts well the fluctuating velocity components except for the fluctuating radial velocity at y/D_{h}= 1, which is not also predicted well in time-averaged comparison.

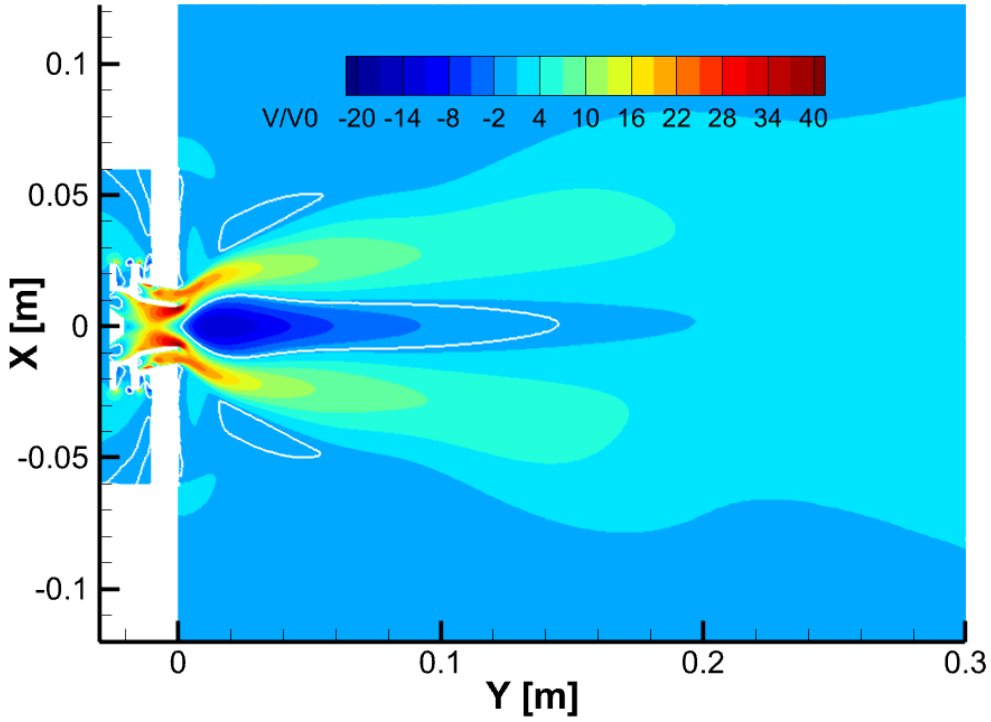


Figure 3.19: Time-averaged velocity contour of RANS for unconfined condition (white lines represent the recirculation zone borders)

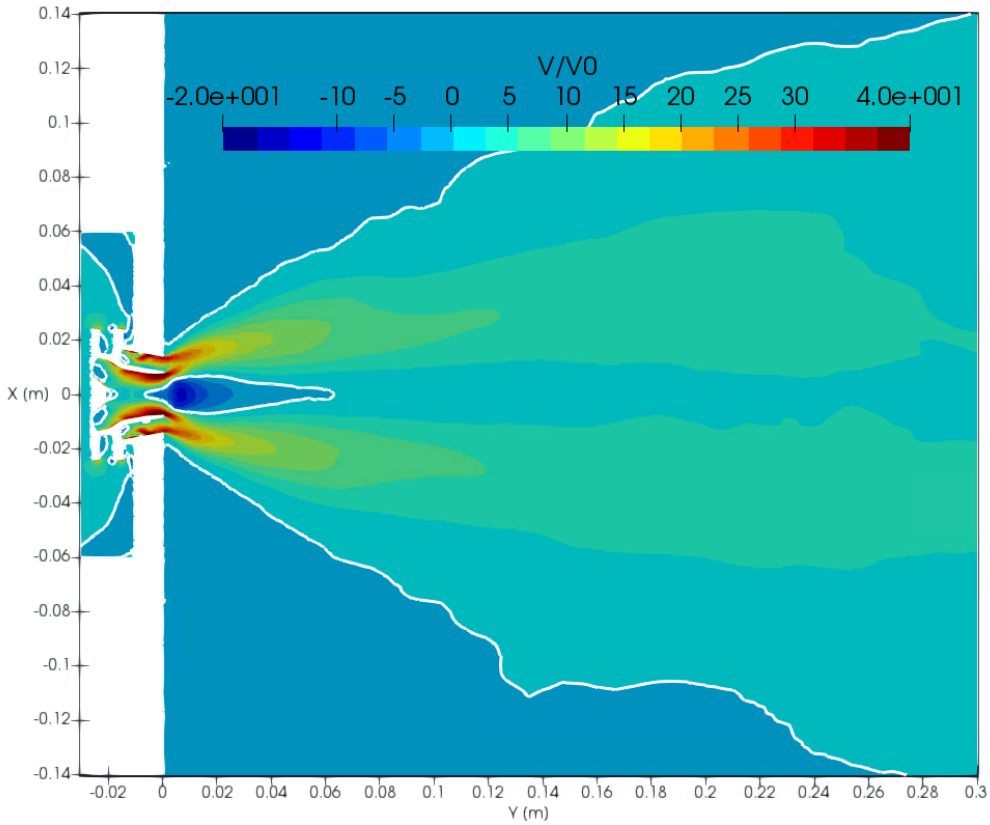


Figure 3.20: Time-averaged velocity contour of LES for unconfined condition (white lines represent the recirculation zone borders)

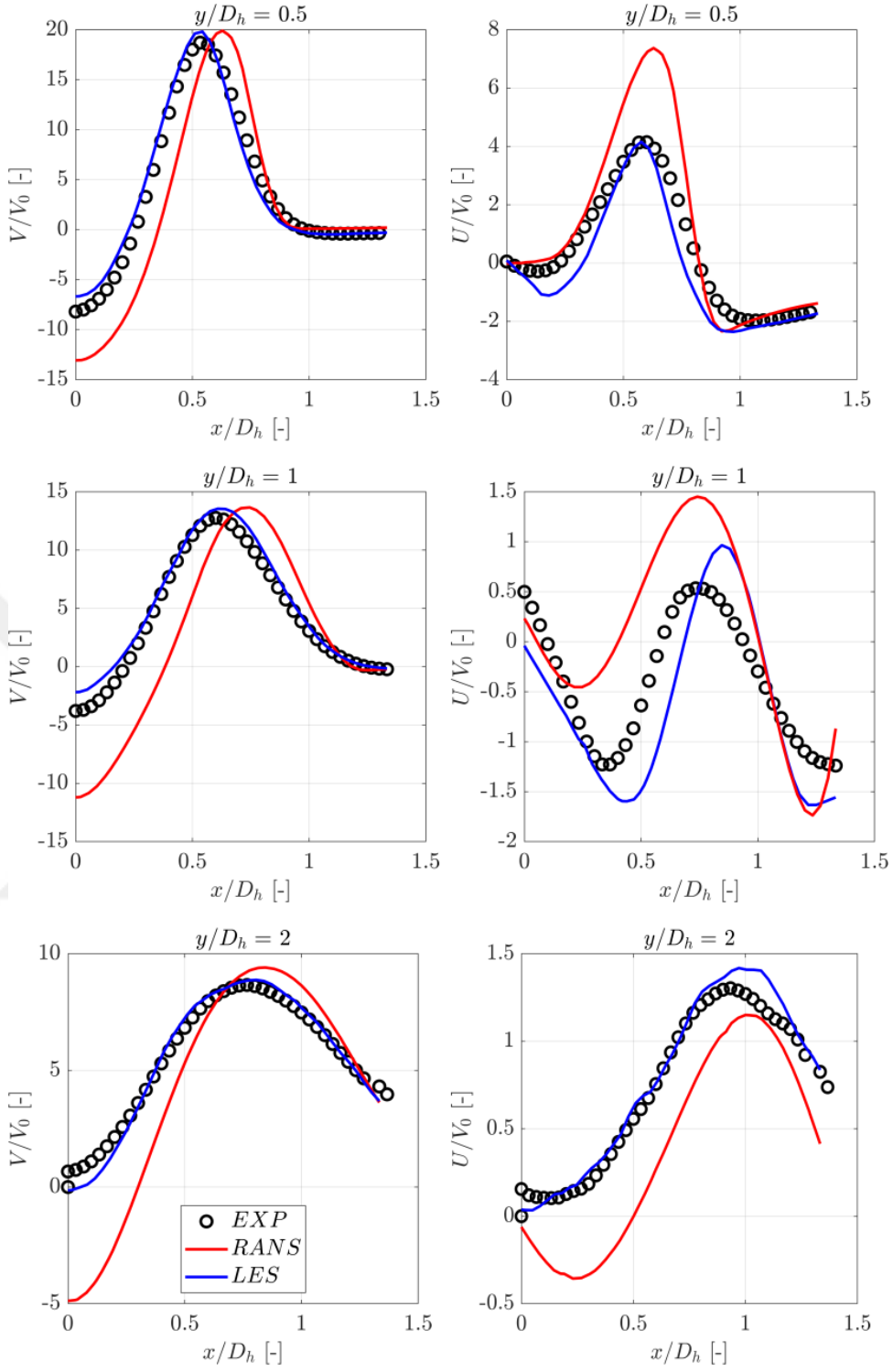


Figure 3.21: Comparison of the time-averaged axial velocity (the velocity component in the y-direction, V/V_0), radial velocity (the velocity component in the x-direction, U/V_0) profiles obtained from the PIV measurements (symbols) and numerical simulations (full lines) for the RANS (red) and the LES (blue) configurations in the y/D_h= 0.5, 1 and 2

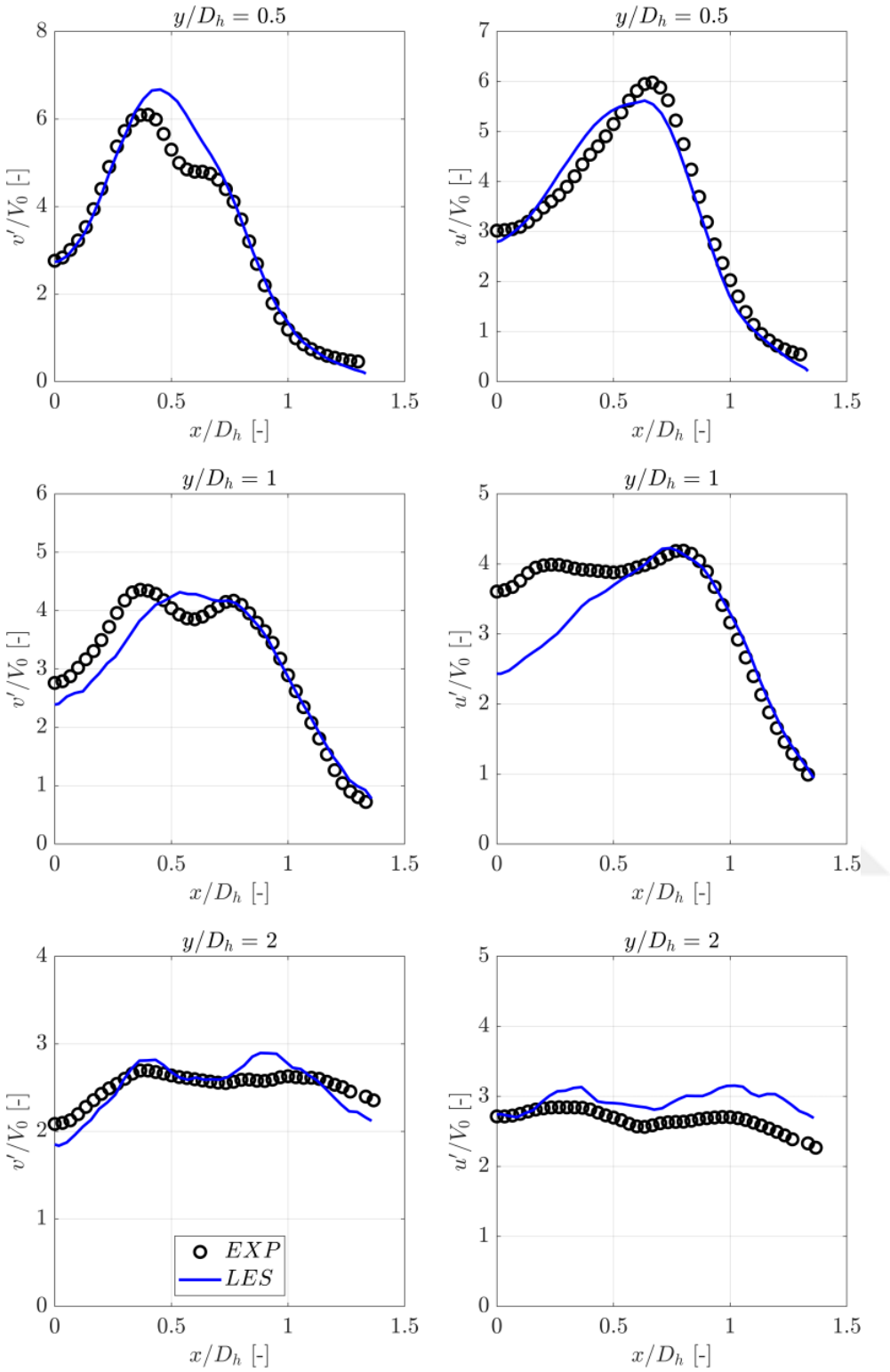


Figure 3.22: Comparison of the r.m.s axial velocity (the velocity component in the y-direction, v'/V_0), radial velocity (the velocity component in the x-direction, u'/V_0) profiles obtained from the PIV measurements (symbols) and numerical simulations (full lines) for the LES (blue) in the y/D_h= 0.5, 1 and 2

In addition to the realizable k-ϵ turbulence model, the effect of the turbulence modeling is observed on the CTRZ length with several turbulence models, as shown in Table 3.4. Interestingly, the standard k-ϵ turbulence model predicts the shortest CTRZ length, which is close to the experimental data. RNG k-ϵ predicts the CTRZ length similar to the realizable k-ϵ and fails to predict the swirling flow field. The k-ω SST turbulence model also fails to predict the swirling flow field correctly. In addition to other turbulence models, the residuals are highly oscillatory for the k-ω SST; thus, the data is sampled for 1000 iterations after the difference between the plotted variables is less than five percent.

Table 3.4: CTRZ length results for different turbulence models

Turbulence Model	CTRZ Length [mm]
Realizable k-ϵ	140
Standard k-ϵ	67
RNG k-ϵ	140
k-ω SST	121

3.2.2 Coherent flow structures

In this section, the coherent structures of the swirling flow field are extracted by performing S-POD on the radial velocity component of the fast PIV data. First, the fast PIV data is collected at 4 kHz for all cases, but no distinct feature is extracted higher than 1.2 kHz for confined situations. That's why fast PIV data is collected at 3 kHz for confined configurations (see Table 3.4) to observe larger zone. Due to the varying measurement plane size due to different confinement levels, the data is collected between x/D_{h} =$\pm$1.2 for the low confinement cases, while the measurements are performed from the center of the swirler to the side walls for medium and high confinement cases. The snapshot-POD is also applied to full-plane on low-frequency PIV data to extract the expected low-frequency modes to match with half-plane S-POD mode shapes. Finally, defining the symmetric and anti-symmetric structures Sieber et al. method is followed [44].

The first three mode shapes of the CR swirlers are shown in Fig. 3.23. The first mode of each configuration has an anti-symmetric helical structure that defines the PVC. The frequency and amplitude of the PVC mode shape are shown in Table 3.5 for each CR case. It reveals that the frequency values of the PVC structure remain similar under the different confinement levels, which means a change in the confinement level is not effective on the frequency value of the PVC. However, the amplitude of this mode shape changes significantly at different confinement levels. The second S-POD modes of the unconfined and low confinement cases represent a radially expanding and contracting motion of the CTRZ. For other confined configurations, the second mode shape of the medium confinement case represents the interaction between the outer shear layer and the corner recirculation zone, which is also observed in the third mode of the low confinement case. The second S-POD mode shape of the high confinement case exposes a low-frequency global instability mode shape (St$\approx$ 0.1) which is commonly observed in the swirl stabilized combustors [30]. Sieber et al. [43] showed this mode shape in both POD and S-POD analysis, thus to be ensured that the second S-POD mode shape of the high confinement case (as mentioned above to obtain less noisy data, the data is collected at half of the burner for the highest confinement ratio case) compared with the snapshot-POD mode to match the findings

of Sieber et al. [43], [44] and the comparison is shown in Fig. 3.24. The Strouhal number of the second S-POD mode shape is calculated using the swirler diameter and the mean velocity value at the swirler exit and found as 0.11, which is very close to the findings of Oberleithner et al. [30] as 0.1. This reveals that this mode shape is observed for the first time in a radial-radial type swirler. Interestingly, this mode shape is not observed in the lower confinement ratio cases, which means narrowing the confinement walls can suppress this instability. The third mode of the high and medium confinement cases describes a low-frequency vortex shedding motion around the shear layer. Finally, the third mode shape of the unconfined case defines a symmetric double-helical mode shape which is the highest frequency phenomenon between each S-POD mode, and its frequency is around 1.6 kHz. This mode shape is not observed for confined cases, and it can be inferred that the confinement suppresses such a high-frequency double-helical mode shape.

Table 3.5: Frequency and amplitude of the PVC for the CR and CO swirlers under different confinement conditions

Case	Frequency [Hz]	Amplitude $x10^6$
CR=Unconfined	1202.5	6.961
CR= Low Confinement Ratio	1203	0.239
CR= Medium Confinement Ratio	1210.8	0.475
CR= High Confinement Ratio	1209	0.237
CO= Low Confinement Ratio	1194.9	6.401
CO= Medium Confinement Ratio	1187.5	392.236
CO= High Confinement Ratio	1209.3	0.662

The S-POD mode shapes of the CO swirler are shown in Fig. 3.25. The first mode shapes define the PVC structure as in the CR swirler cases. The frequency and amplitude content of each case also are shown in Table 3.5. PVC is also insensitive to the confinement walls for CO swirlers, as observed in the CR swirler. Also, the highest PVC amplitude is observed for the medium confinement case of the CO swirler, which is also valid for the CR swirler. The second mode shapes of each case define the recirculation zone wall interactions similar to CR swirler. The medium and

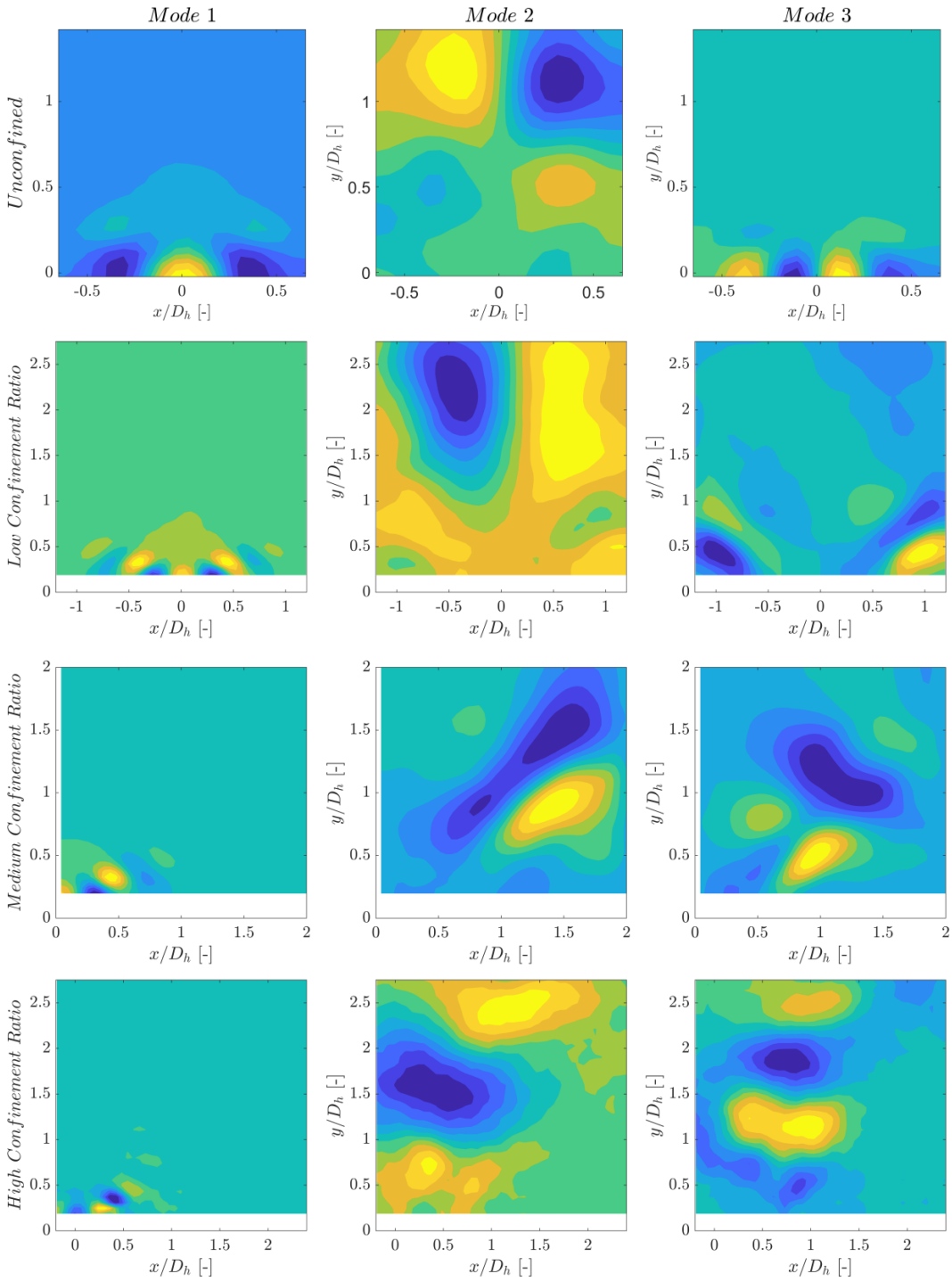


Figure 3.23: The first three most energetic modes obtained from the S-POD analysis for the CR swirler under different confinement conditions

high confinement cases' third mode shape defines vortex shedding motion around the shear layer. The third mode shape represents the low-frequency double-helical mode structure in the low confinement ratio case of CO swirler.

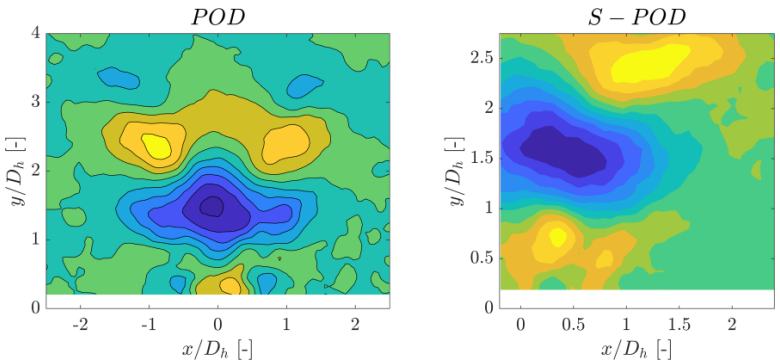


Figure 3.24: The snapshot-POD and S-POD mode shape of the global hydrodynamic instability

The confinement walls change the energy level of the PVC in the flow field. In Table 3.6, the ratio of the PVC energy to the total energy of the flow is shown for the CO and CR swirlers under different confinement ratio conditions. The energy level of the PVC in the flow field is remarkably high in the CO swirler than in the CR swirler. In both swirlers, the most energetic PVC structure is observed in the medium confinement ratio cases. Changing the confinement level in the CR swirler makes the energy ratio of PVC similar as observed in the low and high confinement ratio cases. However, increasing the confinement ratio beyond the medium confinement ratio reduces the energy contribution of the PVC in the flow. The energy of the PVC increases as the swirling momentum [38]. The possible reason for the more energetic PVC structure in the flow is higher swirling momentum in the CO swirler due to the same orientated primary and secondary swirler channels.

Table 3.6: Energy contribution of the PVC in the total energy of the flow

Case	Energy Level [%]
CR= Low Confinement Ratio	0.827
CR= Medium Confinement Ratio	1.567
CR= High Confinement Ratio	0.854
CO= Low Confinement Ratio	5.271
CO= Medium Confinement Ratio	5.711
CO= High Confinement Ratio	3.976

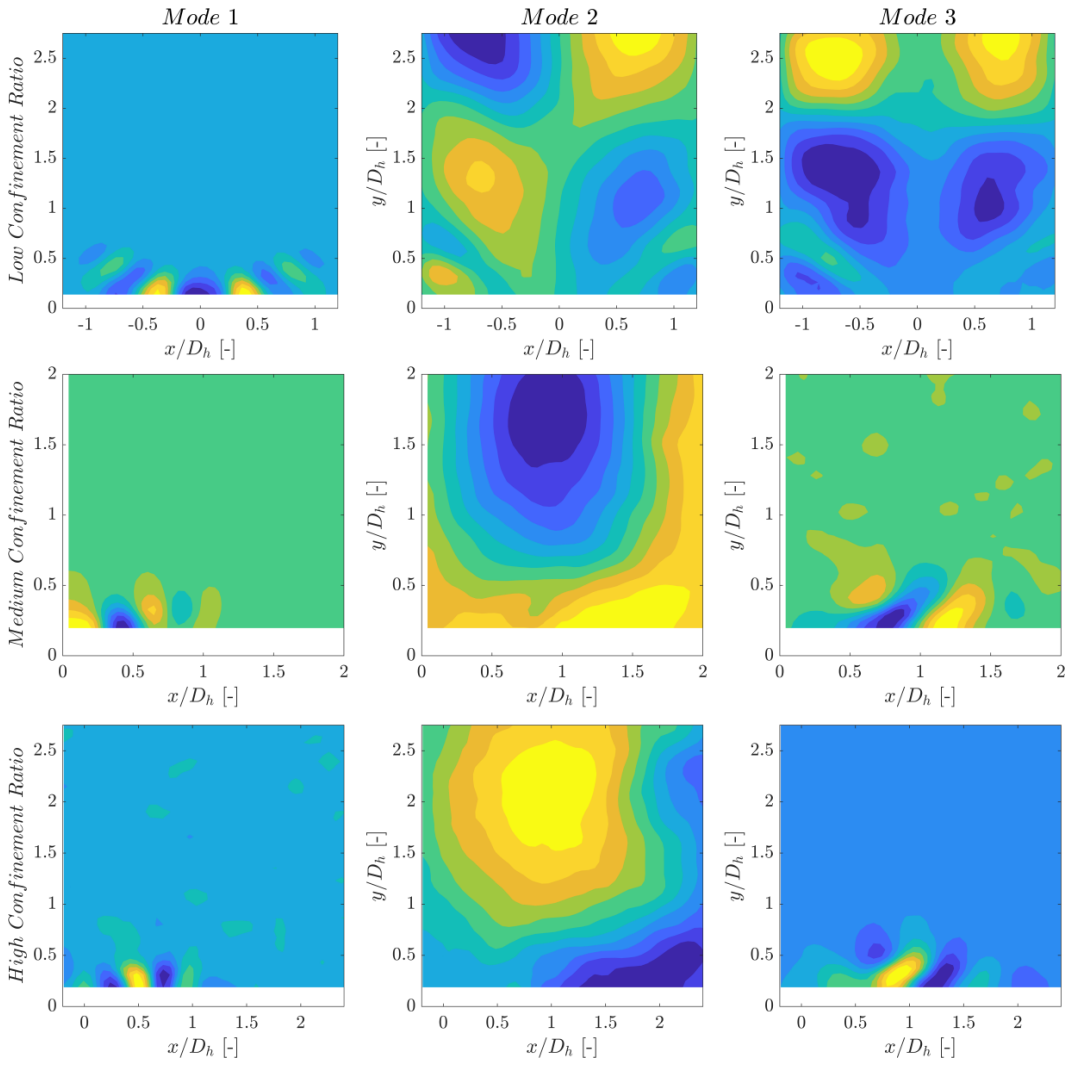


Figure 3.25: The first three most energetic modes obtained from the S-POD analysis for the CO swirler under different confinement condition

3.3 Effect of channel number

The effect of the channel number on the time-averaged flow field is investigated by Gencer et al. [86] at a constant level of the confinement ratio and SN. The 2D2C PIV results show that the effect of the channel number is negligible if the SN is kept same and the velocity profiles at y/D_{h}= 1, 2 and 3 is shown in Fig. 3.26. In these plots, S refers to square shape and numerical values represent the swirler channel configuration. As shown in the Fig. 3.26, no remarkable differences are observed in the axial velocity profiles.

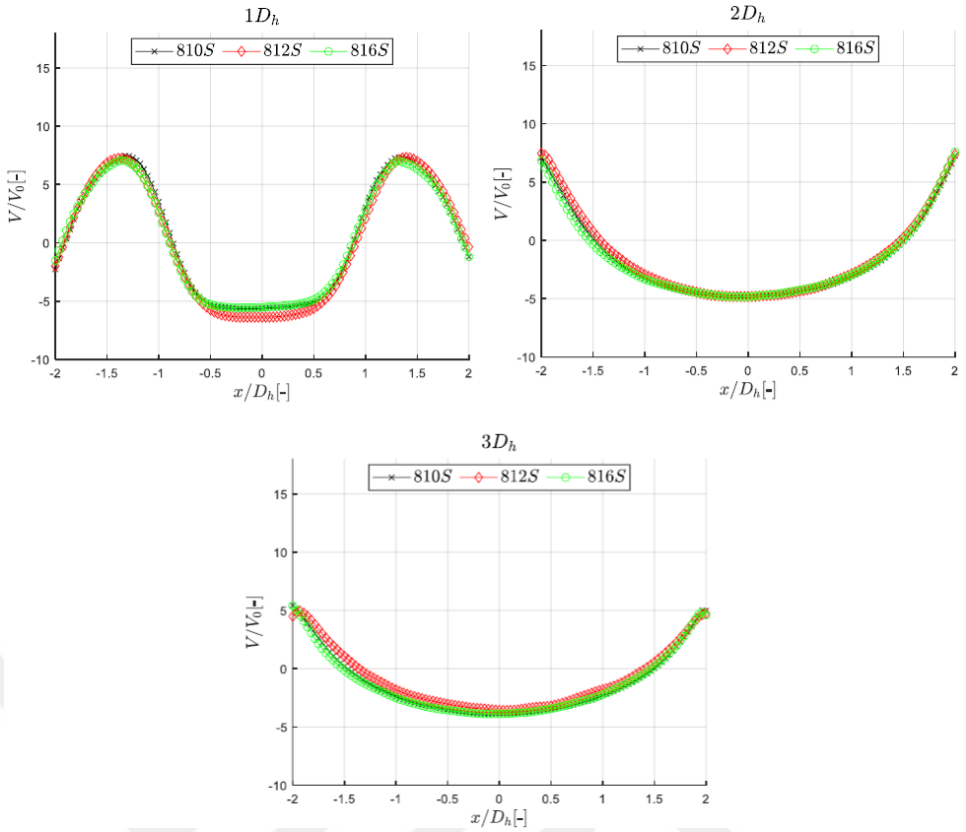


Figure 3.26: Effect of the channel number on the time-averaged axial velocity profiles [86]

In addition to time-averaged comparison, the effect of the vane numbers is also investigated on the PVC dynamics using time-resolved PIV measurements. For this purpose, two different channel numbers 8-10 and 8-16 in both CR and CO configurations at the same SN is evaluated. As observed in the previous comparison (see Table 3.5) , the frequency of the PVC is not affected by the confinement walls thus the investigation is performed in the low confinement ratio to observe whole measurement plane. The PVC mode shapes are observed in Fig. 3.27. The PVC is a helical anti-symmetric mode structure and exists in all swirler configurations. Also, the frequency and amplitude contents are listed in Table 3.7. The frequency of the PVC structure is not sensitive to number and the value of the frequency varies only few tens of Hertz while the amplitude of the PVC changes significantly.

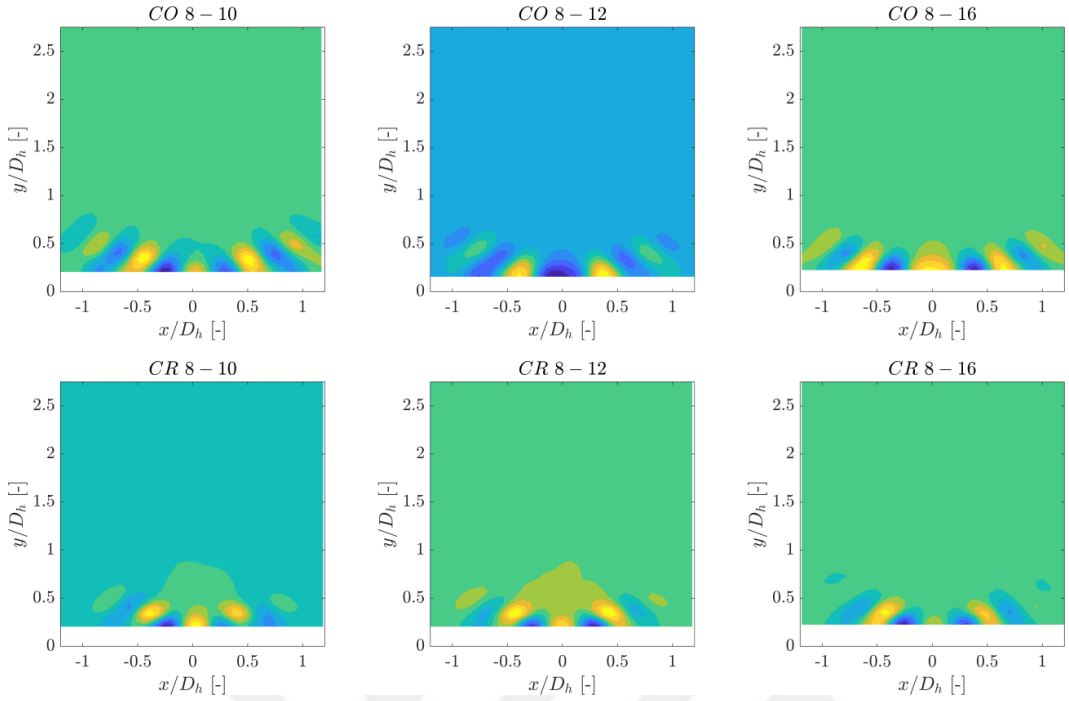


Figure 3.27: PVC modes shapes for different channel numbers and orientations

Table 3.7: Frequency and amplitude of the PVC for different channel numbers and orientations

Case	Frequency [Hz]	Amplitude $x10^6$
CR 8-10	1230.9	0.48
CR 8-12	1203	0.239
CR 8-16	1240.5	0.357
CO 8-10	1194	1.358
CO 8-12	1194.9	6.401
CO 8-16	1218	1.168

CHAPTER 4

CONCLUSION

In this study, planar velocity fields for the CO and the CR radial-radial swirler configurations are obtained using 2D2C PIV measurements to investigate the effects of the sense of rotation. Both swirlers have the same total swirl number of 1.2 at the edge of the venturi yet with different channel orientations. Numerical simulations are also performed to obtain time-averaged three-dimensional flow fields to complement the PIV measurements.

The flow expansion angle is the most prominent difference between the time-averaged flow fields of the CO and the CR swirler configurations. In the CO case, the flow expands rapidly, becoming a dome-attached flow immediately after the jet exit. On the other hand, the swirling flow has a smaller expansion angle in the CR configuration, leading to the formation of corner recirculation zones. The reduced expansion angle in the CR swirler can be attributed to decreased swirl momentum due to the interaction between the counter-rotating jets. As a result, the CTRZ region has a typical conical form in the CR configuration. In contrast, a wide-open CTRZ is observed in the CO configuration with a longer axial extent and higher recirculating mass flow rate. High TKE regions are correlated with the positions of the inner and the outer shear layers in both cases. The PIV measurements in the cross-stream planes and three-dimensional RANS simulations reveal the dominance of the secondary swirler, which has an absolute SN value of 1.4, in determining the resultant direction of rotation in the flow field. The square shape of the confinement cross-section leads to a similar spiral flow pattern at the axial position of $y/D_h = 3.0$ for both swirlers with detaching and inwardly moving swirling flow close to the corners.

Modal analysis of the flow fields in both cases is performed using the snapshot POD

and the spectral POD techniques. Snapshot-POD analysis combines more than one coherent flow structure in a single mode. According to the snapshot POD results, the first two most energetic modes for the CR swirler are associated with low-frequency interaction between the swirling jet, the CTRZ, and the CRZ. The third mode is a combination of the Kelvin-Helmholtz shear-layer instability with a high frequency (St=1.9, corresponding to 1.2 kHz) occurrence. The same high-frequency content is also observed in the power-spectral densities of the time coefficients of the second and the third most energetic modes for the CO swirler. The first mode, on the other hand, is the low-frequency pulsating motion of the CTRZ. The spectral POD technique is then used to isolate coherent flow occurrences into different modes, revealing the PVC presence at St=1.9 (corresponding to the frequency of 1.2 kHz). For the studied SN values and radial-radial swirler configurations, the frequency of the PVC is insensitive to the channel orientation.

The CO and CR radial-radial type swirlers are also compared at different confinement levels in terms of mean and dynamic behavior. Time-averaged PIV results show that the confinement ratio changes the vortex breakdown type and affects the flow field oppositely for the CO and the CR swirlers. The expansion angle increases as the confinement ratio level increases in the CO swirler while it decreases with the confinement ratio in the CR swirler. In addition to experimental data, LES and RANS analyses are conducted to evaluate the performance of numerical models and observe the regions where it is not visualized in experiments. The numerical studies provide results that are, in general, in good agreement with experimental data. The numerical vorticity contours reveal that the primary and secondary jets mix after a while when they enter the test section. S-POD is applied to the fast PIV measurements to extract the coherent structures and their frequency content. The PVC is observed in all cases at a frequency of 1.2 kHz, which is insensitive to confinement walls and channel orientation. Considering the results, the highest frequency coherent structure is observed in the unconfined case of the CR swirler at a frequency of 1.6 kHz. However, this structure is not observed in confined cases. Moreover, a low-frequency global instability mode of the swirl burner is observed in the highest confinement ratio case of the CR swirler, which disappears in other cases. Therefore, it can be hypothesized that the existence of confinement walls suppresses this flow instability mode.

CHAPTER 5

FUTURE WORKS

Observing the performance of the swirlers in reacting flow conditions are highly crucial. For this purpose, the CANTEC-SD (CAN Type Experimental Combustor-Swirler Dynamics) is designed and produced to test the performance of the CO and CR swirlers in reacting conditions. The confinement ratio of the CANTEC-SD is kept the same with the medium confinement ratio case of the RUZGEM setup. The schematic of the CANTEC-SD is shown in Fig. 5.1. CANTEC-SD will provide how lean blow-out and rich extinction limits are affected by changing the swirler channel orientation. In addition, the effect of the channel orientation on the dominant frequency of the swirling flow field in the reacting condition is observed. These results will provide a comparison basis regarding the reliability of the radial-radial type swirler configurations at the SN of 1.2.

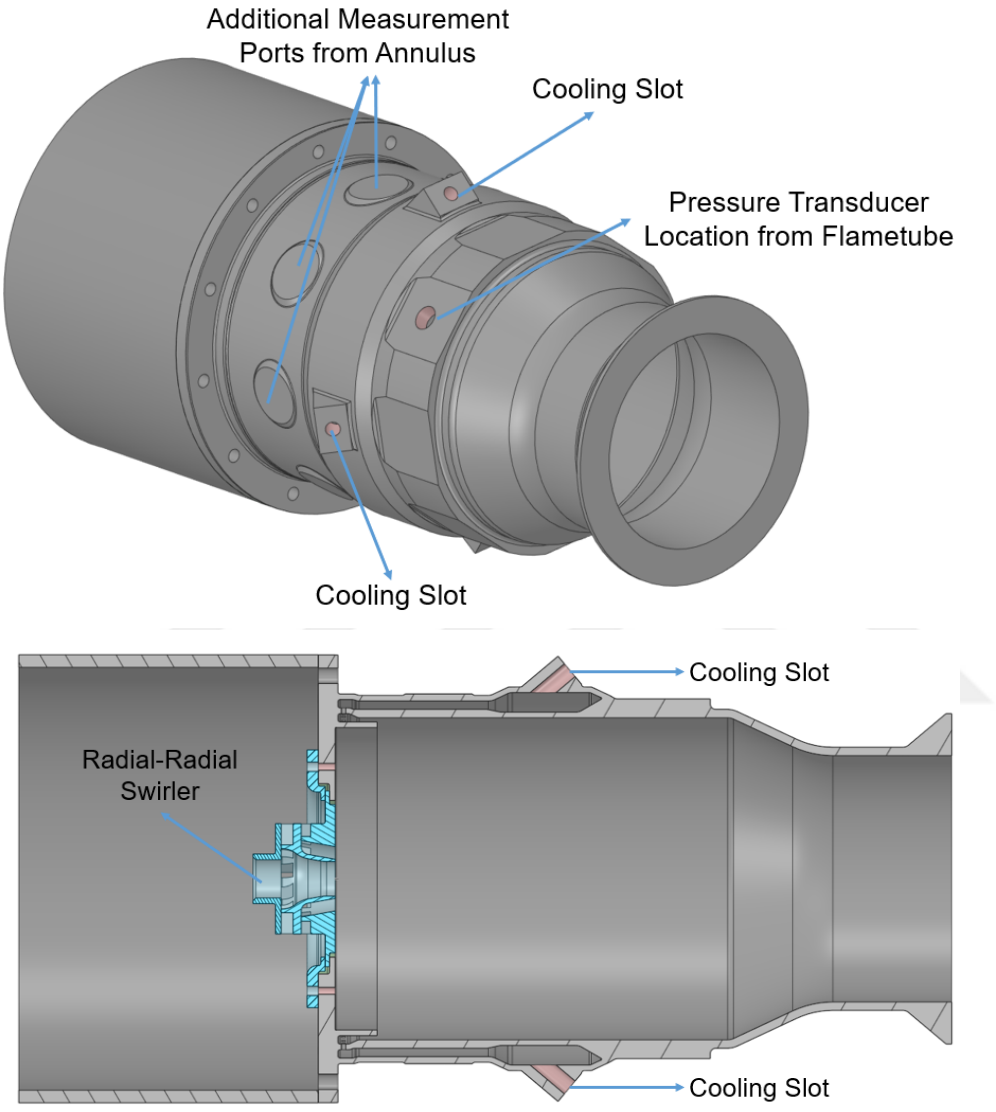


Figure 5.1: Isometric (top) and cross-section (bottom) view of the CANTEC-SD

REFERENCES

[1]H. I. H. Saravanamuttoo, H. Cohen, G. F. C. Rogers, P. Straznicky, and N. A, *Gas Turbine Theory, 7th Edition*. Pearson, 2017.

[2]S. Farokhi, *Aircraft Propulsion, 2nd Edition*. Wiley–Blackwell, 2014.

[3]H. A. Lefevbre and D. R. Ballal, "Gas turbine combustion: Alternative fuels and emissions, third edition", in CRC Press, 2010.

[4]T. C. Lieuwen, *Unsteady Combustor Physics*. Cambridge University Press, 2012.

[5]N. Syred, N. A. Chigier, and J. M. Beer, "Flame stabilization in recirculation zones of jets with swirl", *Symposium (International) on Combustion*, vol. 13, no. 1, pp. 617–624, 1971. DOI: 10.1016/S0082-0784(71)80063-2.

[6]J. M. Beér and N. Chigier, *Combustion Aerodynamics*. New York: Wiley, 1972.

[7]M. Percin, M. Vanierschot, and B. W. Van Oudheusden, "Analysis of the pressure fields in a swirling annular jet flow", *Experiments in Fluids*, vol. 58, no. 166, 2017. DOI: 10.1007/s00348-017-2446-3.

[8]P. Gobbato, M. Masi, A. Capelletti, and M. Antonello, "Effect of the reynolds number and the basic design parameters on the isothermal flow field of low-swirl combustors", *Experimental Thermal and Fluid Science*, vol. 84, pp. 242–250, 2017. DOI: 10.1016/j.expthermflusci.2017.02.001.

[9]S. Menon and R. Ranjan, "Spray combustion in swirling flow", in Cambridge University Press, 2016. DOI: 10.1017/CBO9781316480243.014.

[10]T. Sarpkaya, "Vortex breakdown in swirling conical flows", *AIAA JOURNAL*, vol. 9, no. 9, 1971. DOI: 10.2514/3.49981.

[11]P. Moise and J. Mathew, "Hysteresis and turbulent vortex breakdown in transitional swirling jets", *Journal of Fluid Mechanics*, vol. 915, 2021. DOI: 10.1017/jfm.2021.118.

[12]K. Oberleithner, M. Stöhr, S. H. Im, C. M. Arndt, and A. M. Steinberg, "Formation and flame-induced suppression of the precessing vortex core in a swirl

combustor: Experiments and linear stability analysis", *Combustion and Flame*, vol. 162, 8 2015. DOI: 10.1016/j.combustflame.2015.02.015.

[13]T. Terasaki and S. Hayashi, "The effects of fuel–air mixing on nox formation in non-premixed swirl burners", *26th Symposium (International) on Combustion*, vol. 26, pp. 2733–2739, 2 1996. DOI: 10.1016/S0082-0784(96)80110-X.

[14]R. Hadef and B. Lenze, "Effects of co- and counter-swirl on the droplet characteristics in a spray flame", *Chemical Engineering and Processing*, vol. 47, pp. 2209–2217, 12 2008. DOI: 10.1016/j.cep.2007.11.017.

[15]I. S. Carvalho and M. V. Heitor, "Liquid film break-up in a model of a prefilming airblast nozzle", *Experiments in Fluids*, vol. 24, pp. 408–415, 1998.

[16]A. H. Lefebvre and V. G. McDonell, *Atomization and Sprays, 2nd Edition*. CRC Press, 2017.

[17]Y. Kao, S. B. Tambe, and S.-M. Jeng, "Effect of dome geometry on swirling flow field characteristics of a counter-rotating radial-radial swirler", *Proceedings of ASME Turbo Expo 2013: Turbine Technical Conference and Exposition GT2013*, 2013. DOI: 10.1115/GT2013-95344.

[18]Y. Sung and G. Choi, "Non-intrusive optical diagnostics of co- and counter-swirling flames in a dual swirl pulverized coal combustion burner", *Fuel*, vol. 174, pp. 76–88, 2016. DOI: 10.1016/j.fuel.2016.01.011.

[19]A. Degeneve, R. Vicquelin, C. Mirat, J. Caudal, and T. Schuller, "Impact of co- and counter-swirl on flow recirculation and liftoff of non-premixed oxy-flames above coaxial injectors", *Proceedings of the Combustion Institute*, vol. 38, pp. 5501–5508, 4 2021. DOI: 10.1016/j.proci.2020.06.279.

[20]K. Merkle, H. Buchner, N. Zarzalis, and O. N. Sara, "Influence of co and counter swirl on lean stability limits of an airblast nozzle", *ASME Turbo Expo 2003, collocated with the 2003 International Joint Power Generation Conference*, pp. 1–9, 2003. DOI: 10.1115/GT2003-38004.

[21]A. K. Gupta, M. J. Lewis, and M. Daurer, "Swirl effects on combustion characteristics of premixed flames", *Journal of Engineering for Gas Turbines and Power*, vol. 123, 2001. DOI: 10.1115/1.1339987.

[22]G. Li and E. J. Gutmark, “Effects of swirler configurations on flow structures and combustion characteristics”, *Proceedings of the ASME Turbo Expo*, 2004. DOI: 10.1115/GT2004-53674.

[23]H. B. Bolat and S. Uslu, “Investigation of the effect of co/counter configurations of a double swirler airblast atomizer ın an annular turbojet combustor with computational fluid dynamics”, *AIAA SCITECH 2015 Forum*, 2015. DOI: 10.2514/6.2015-3787.

[24]F. Kiyici and M. Percin, “Experimental investigation of the confinement effects in radial-radial swirlers”, *ASME Turbo Expo 2021: Turbomachinery Technical Conference and Exposition*, 2021. DOI: 10.1115/GT2021-58653.

[25]Y. Fu, J. Cai, S.-M. Jeng, and H. Mongia, “Confinement effects on the swirling flow of a counter-rotating swirl cup”, *ASME Turbo Expo 2005: Turbomachinery Technical Conference and Exposition*, 2005. DOI: 10.1115/GT2005-68622.

[26]J. Cai, Y. Fu, N. Flohre, S.-M. Jeng, and H. Mongia, “Experimental study on coherent structures of a counter-rotating multi-swirler cup”, *43rd AIAA/ASME/SAE/ASEE Joint Propulsion Conference and Exhibit*, 2007. DOI: 10.2514/6.2007-5674.

[27]Q. Zeng and Y. Yuan, “Flow dynamics of dual-stage counter-swirl combustor in different confinement spaces”, *International Communications in Heat and Mass Transfer*, vol. 116, 2020. DOI: 10.1016/j.icheatmasstransfer.2020.104633.

[28]L. Ji, J. Wang, W. Zhang, R. Mao, G. Hu, and Z. Huang, “Effect of confinement ratio on flame structure and blow-off characteristics of swirl flames”, *Experimental Thermal and Fluid Science*, vol. 135, 2022. DOI: 10.1016/j.expthermflusci.2022.110630.

[29]N. Syred, “A review of oscillation mechanisms and the role of the precessing vortex core (pvc) in swirl combustion systems”, *Progress in Energy and Combustion Science*, vol. 32, pp. 93–161, 2 2006. DOI: 10.1016/j.pecs.2005.10.002.

[30]K. Oberleithner, M. Sieber, C. N. Nayeri, *et al.*, “Three-dimensional coherent structures in a swirling jet undergoing vortex breakdown: Stability analysis and empirical mode construction”, *Journal of Fluid Mechanics*, vol. 679, 2011. DOI: 10.1017/jfm.2011.141.

[31]M. Frederick, K. Manoharan, J. Dudash, B. Brubaker, S. Hemchandra, and J. O'Connor, "Impact of precessing vortex core dynamics on shear layer response in a swirling jet", *Journal of Engineering for Gas Turbines and Power*, vol. 140, 6 2018. DOI: 10.1115/1.4038324.

[32]S. Candel, D. Durox, T. Schuller, J.-F. Bourgouin, and J. P. Moeck, "Dynamics of swirling flames", *Annual Review of Fluid Mechanics*, vol. 46, pp. 147–173, 2014. DOI: 10.1146/annurev-fluid-010313-141300.

[33]M. Freitag, M. Klein, M. Gregor, *et al.*, "Mixing analysis of a swirling recirculating flow using dns and experimental data", *International Journal of Heat and Fluid Flow*, vol. 27, pp. 636–643, 4 2006. DOI: 10.1016/j.ijheatfluidflow.2006.02.020.

[34]P. M. Anacleto, E. C. Fernandes, M. V. Heitor, and S. I. Shtork, "Swirl flow structure and flame characteristics in a model lean premixed combustor", *Combustion Science and Technology*, vol. 175, pp. 1369–1388, 8 2003. DOI: 10.1080/00102200302354.

[35]A. M. Steinberg, I. Boxx, M. Stöhr, C. D. Carter, and W. Meier, "Flow–flame interactions causing acoustically coupled heat release fluctuations in a thermo-acoustically unstable gas turbine model combustor", *Combustion and Flame*, vol. 157, pp. 2250–2266, 12 2010. DOI: 10.1016/j.combustflame.2010.07.011.

[36]M. García-Villalba and J. Fröhlich, "Les of a free annular swirling jet – dependence of coherent structures on a pilot jet and the level of swirl", *International Journal of Heat and Fluid Flow*, vol. 27, pp. 911–923, 5 2006. DOI: 10.1016/j.ijheatfluidflow.2006.03.015.

[37]D. Dunham, A. Spencer, J. M. James, and M. Dianat, "Comparison of urans and les cfd methodologies for air swirl fuel injectors", *ASME Turbo Expo 2008: Power for Land, Sea, and Air*, pp. 187–196, 2008. DOI: 10.1115/GT2008-50278.

[38]A. Karmarkar, M. Frederick, S. Clees, D. Mason, and J. O'Connor, "Role of turbulence in precessing vortex core dynamics", *ASME Turbo Expo 2019: Turbomachinery Technical Conference and Exposition*, 2019. DOI: 10.1115/GT2019-91095.

[39]D. Mason, S. Clees, M. Frederick, and J. O'Connor, "The effects of exit boundary condition on precessing vortex core dynamics", *ASME Turbo Expo 2019: Turbomachinery Technical Conference and Exposition*, 2019. DOI: 10.1115/GT2019-91079.

[40]P. Holmes, L. J. Lumley, G. Berkooz, and W. C. Rowley, "Coherent structures", in *Turbulence, Coherent Structures, Dynamical Systems and Symmetry*, Cambridge University Press, 1996. DOI: 10.1017/CBO9780511622700.

[41]K. Taira, S. L. Brunton, S. T. M. Dawson, *et al.*, "Modal analysis of fluid flows: An overview", *AIAA Journal*, vol. 55, 12 2017. DOI: 10.2514/1.J056060.

[42]S. Terhaar, K. Oberleithner, and C. O. Paschereit, "Impact of steam-dilution on the flame shape and coherent structures in swirl-stabilized combustors", *Combustion Science and Technology*, vol. 186, 7 2014. DOI: 10.1080/00102202.2014.890597.

[43]M. Sieber, C. O. Paschereit, and K. Oberleithner, "Spectral proper orthogonal decomposition", *Journal of Fluid Mechanics*, vol. 792, 2016. DOI: 10.1017/jfm.2016.103.

[44]——, "Advanced identification of coherent structures in swirl-stabilized combustors", *Journal of Engineering for Gas Turbines and Power*, vol. 139, 2 2017. DOI: 10.1115/1.4034261.

[45]M. Vanierschot, J. S. Müller, M. Sieber, M. Percin, B. W. an Oudheusden, and K. Oberleithner, "Single-and double-helix vortex breakdown as two dominant global modes in turbulent swirling jet flow", *Journal of Fluid Mechanics*, vol. 883, 2020. DOI: 10.1017/jfm.2019.872.

[46]Y. Shen, M. Ghulam, K. Zhang, E. Gutmark, and C. Duwig, "Vortex breakdown of the swirling flow in a lean direct injection burner", *Physics of Fluids*, vol. 32, 2020. DOI: 10.1063/5.0028838.

[47]J. L. Halpin, "Swirl generation and recirculation using radial swirl vanes", *ASME 1993 International Gas Turbine and Aeroengine Congress and Exposition*, 1993. DOI: 10.1115/93-GT-169.

[48]*Piv working principle*, https://www.dantecdynamics.com/solutions-applications/solutions/fluid-mechanics/particle-image-velocimetry-piv/measurement-principles-of-piv/, Accessed: 2022-05-22.

[49]J. Westerweel and F. Scarano, "Universal outlier detection for piv data", *Experiments in Fluids*, vol. 39, pp. 1096–1100, 2005. DOI: 10.1007/s00348-005-0016-6.

[50]C. Atkinson, S. Coudert, J. M. Foucaut, M. Stanislas, and J. Soria, "The accuracy of tomographic particle image velocimetry for measurements of a turbulent boundary layer", *Experiments in Fluids*, vol. 50, pp. 1031–1056, 2011. DOI: 10.1007/s00348-010-1004-z.

[51]A. Sciacchitano and B. Wieneke, "Tpiv uncertainty propagation", *Measurement Science and Technology*, vol. 27, 8 2016. DOI: 10.1088/0957-0233/27/8/084006.

[52]S. V. Patankar and D. B. Spalding, "A calculation procedure for heat, mass and momentum transfer in three-dimensional parabolic flows", *International Journal of Heat and Mass Transfer*, vol. 15, 10 1972. DOI: 10.1016/0017-9310(72)90054-3.

[53]I. R. Issa, "Solution of the implicitly discretised fluid flow equations by operator-splitting", *Journal of Computational Physics*, vol. 62, 1 1986. DOI: 10.1016/0021-9991(86)90099-9.

[54]*Ansys fluent theory guide*, https://www.afs.enea.it/project/neptunius/docs/fluent/html/th/main_pre.htm, Accessed: 2022-05-22.

[55]H. Tennekes and J. L. Lumley, *A First Course in Turbulence*. MIT Press, 1972.

[56]L. F. Richardson, *Weather Prediction by Numerical Process*. Cambridge University Press, 1922.

[57]P. Davidson, *Turbulence: An Introduction for Scientists and Engineers*. Oxford University Press, Second Edition, 2015.

[58]T. Poinsot and D. Veynante, *Theoretical and Numerical Combustion*. R.T. Edwards, Inc.; 2nd edition, 2005.

[59]O. Reynolds, "On the dynamical theory of incompressible viscous fluids and the determination of the criterion", *philosophy transactions of the royal society*, vol. 186, 1895. DOI: 10.1098/rsta.1895.0004.

[60]D. Ting, *Basics of Engineering Turbulence*. Academic Press; 1st edition, 2016.

[61]J. Boussinesq, “Théorie de l’écoulement tourbillonnant et tumultueux des liquides dans les lits rectilignes a grande section”, *Paris, Gauthier-Villars et fils*, 1897.

[62]S. Wallin and A. V. Johansson, “An explicit algebraic reynolds stress model for incompressible and compressible turbulent flows”, *Journal of Fluid Mechanics*, vol. 403, 2000. DOI: 10.1017/S0022112099007004.

[63]T. B. Gatski and C. G. Speziale, “On explicit algebraic stress models for complex turbulent flows”, *Journal of Fluid Mechanics*, vol. 254, 1993. DOI: 10.1017/S0022112093002034.

[64]F. Vashahi, S. Rezaei, R. A. Dafsari, and J. Lee, “Sensitivity analysis of the vane length and passage width for a radial type swirler employed in a triple swirler configuration”, *Theoretical and Applied Mechanics Letters*, vol. 9, 6 2019. DOI: 10.1016/j.taml.2019.05.004.

[65]A. Bay, F. Kiyici, and M. Percin, “Effect of flare geometry on the flow field of radial-radial swirlers”, *Proceedings of ASME Turbo Expo 2022 Turbomachinery Technical Conference and Exposition*, 2022. DOI: –.

[66]W. P. Jones and B. E. Launder, “The prediction of laminarization with a two-equation model of turbulence”, *International Journal of Heat and Mass Transfer*, vol. 15, 2 1972. DOI: 10.1016/0017-9310(72)90076-2.

[67]T.-H. Shih, W. W. Liou, A. Shabbir, Z. Yang, and J. Zhu, “A new k-ϵ eddy viscosity model for high reynolds number turbulent flows”, *Computers Fluids*, vol. 24, 3 1995. DOI: 10.1016/0045-7930(94)00032-T.

[68]M. Wolfstein, “The velocity and temperature distribution of one-dimensional flow with turbulence augmentation and pressure gradient”, *International Journal of Heat and Mass Transfer*, vol. 12, 3 1969. DOI: 10.1016/0017-9310(69)90012-X.

[69]H. C. Chen and V. C. Patel, “Near-wall turbulence models for complex flows including separation”, *AIAA Journal*, vol. 26, 6 1988. DOI: 10.2514/3.9948.

[70]T. Jongen, “Simulation and modeling of turbulent incompressible flows”, *PhD thesis, EPF Lausanne, Lausanne, Switzerland*, 1992.

[71]S. B. Pope, *Turbulent Flows*. 2000. DOI: 10.1017/CBO9780511840531.

[72]J. Smagorinsky, "General circulation experiments with the primitive equations", *Monthly Weather Review,*, pp. 99–164, 1963. DOI: 10.1175/1520-0493(1963)091<0099:GCEWTP>2.3.CO;2.

[73]F. Nicoud and F. Ducros, "Subgrid-scale stress modelling based on the square of the velocity gradient tensor flow", *Turbulence and Combustion*, vol. 62, 3 1999. DOI: 10.1023/A:1009995426001.

[74]*Openfoam theory guide*, https://www.openfoam.com/documentation/overview, Accessed: 2022-05-22.

[75]S. B. Pope, "Ten questions concerning the large-eddy simulation of turbulent flows", *New Journal of Physics*, vol. 6, 2004. DOI: 0.1088/1367-2630/6/1/035.

[76]I. B. Celik, N. Cehreli, and I. Yavuz, "Index of resolution quality for large eddy simulations", *Journal of Fluids Engineering*, vol. 127, 5 2005. DOI: 10.1115/1.1990201.

[77]M. S. Sweeney, S. Hochgreb, M. J. Dunn, and R. S. Barlow, "The structure of turbulent stratified and premixed methane/air flames i: Non-swirling flows", *Combustion and Flame*, vol. 159, pp. 2896–2911, 9 2012. DOI: 10.1016/j.combustflame.2012.06.001.

[78]——, "The structure of turbulent stratified and premixed methane/air flames ii: Swirling flows", *Combustion and Flame*, vol. 159, pp. 2912–2929, 9 2012. DOI: 10.1016/j.combustflame.2012.05.014.

[79]R. Zhou, S. Balusamy, M. S. Sweeney, R. S. Barlow, and S. Hochgreb, "Flow field measurements of a series of turbulent premixed and stratified methane/air flames", *Combustion and Flame*, vol. 160, pp. 2017–2028, 10 2013. DOI: 10.1016/j.combustflame.2013.04.007.

[80]F. Kiyici and H. Turkeri, "Scale resolving simulations of cambridge/sandia turbulent swirling premixed flames", *AIAA SCITECH 2022 Forum*, 2022. DOI: 10.2514/6.2022-1101.

[81]H. Turkeri, S. B. Pope, and M. Muradoglu, "A les/pdf simulator on block-structured meshes", *Combustion Theory and Modelling*, vol. 23, no. 1, pp. 1–41, 2019. DOI: 10.1080/13647830.2018.1475683.

[82]P. G. Tucker, *Unsteady computational fluid dynamics in aeronautics*. Springer, 2014.

[83]L. Sirovich, “Turbulence and the dynamics of coherent structures.i. coherent structures”, *Quarterly of Applied Mathematics*, vol. 45, no. 3, pp. 561–571, 1987.

[84]L. Rayleigh, “On the dynamics of revolving fluids”, *Proceedings of the Royal Society of London, Series A*, vol. 93, 1917.

[85]E. Kilik, “The influence of swirler design parameters on the aerodynamics of the downstream recirculation region”, *School of Mechanical Engineering, Cranfield Institute of Technology, United Kingdom.*, 1976.

[86]B. Gencer, F. Kiyici, and M. Percin, “Effects of vane numbers/types on the swirling flow field characteristics of a counter-rotating radial-radial swirler”, *12th Ankara International Aerospace Conference*, 2021.